

**Combinatorial and Conventional Development of new
Catalysts for the CO₂ Reforming of Methane**

Dissertation

zur Erlangung des Grades

des Doktors der Ingenieurwissenschaften

der Naturwissenschaftlich-Technischen Fakultät III

Chemie, Pharmazie, Bio- und Werkstoffwissenschaften

der Universität des Saarlandes

von

Do Kyoung Kim

Saarbrücken

2006

Tag des Kolloquiums: 07.11.2006

Dekan: Prof. Dr. Kaspar Hegetschweiler

Berichterstatter: Prof. Dr. Wilhelm F. Maier
Prof. Dr. Elmar Heinzle

Prüfungsvorsitzender: Prof. Dr. Uli Kazmaier

Akademischer Beirat: Dr. Andreas Rammo

This work had been achieved during the time from February 2003 to August 2006 at the Universität des Saarlandes in Saarbrücken, under the careful guidance of Prof. Dr. W. F. Maier.

I would like to express my sincere gratitude and appreciation to my advisor, Prof. Dr. W. F. Maier, for providing me with the unique opportunity to work in the research area of combinatorial chemistry & high-throughput experiment, for his expert guidance and mentorship, and for his encouragement and support at all levels.

I thank Prof. Dr. E. Heinzle for his constructive comments and friendly acceptance to be a reviewer.

The financial support from the Deutsche Forschungs Gemeinschaft (grant GRK 232) is greatly acknowledged. I would like to thank every Graduiertenkolleg member, especially Prof. Dr. R. Clasen for organizing the program.

Dr. K. Stöwe offered much-appreciated advice and support throughout the XRD experiment, and Dr. F. Müller for XPS experiment. I thank Mr. R. Richter and Mr. J. Kriesamer for constructing the new reactor, Mrs. H. Höltzen for assisting with product analysis, and Mrs. R. Nagel for helping with the BET measurements.

I thank Prof. Dr. S. I. Woo and Mr. K. S. Oh at KAIST in Korea for the collaboration on the study of the selective oxidation of propane.

I am grateful to all former and present colleagues for their generous help, valuable discussions, and great fun during my whole PhD period.

Finally, I would like to thank my family for their life-long love and support, and especially Sunyoung for all her love and patience.

Publications

Thesis

D.K. Kim, Combinatorial and Conventional Development of new Catalysts for the CO₂ Reforming of Methane, Ph.D. thesis, Universität des Saarlandes, 2006.

D.K. Kim, Catalytic Activity and Durability of Fe/ZSM5, Pt/ZSM5 and Pt-Fe/ZSM5 Catalysts prepared by Sublimation Method for Selective Catalytic Reduction of NO, M.S. thesis, KAIST, 2000.

Journal papers

D.K. Kim and W.F. Maier, Combinatorial discovery of new autoreduction catalysts for the CO₂ reforming of methane, *J. Catal.*, 238, 142-152 (2006).

S.I. Woo, D.K. Kim, Y.K. Park, M.R. Kim and P. Decyk, Wide temperature Window in the Catalytic activity of noble Pt/ZSM5 prepared by Sublimation Method for Selective Catalytic Reduction of NO, *Catal. Lett.*, 85, 69-72 (2003).

P. Decyk, D.K. Kim and S.I. Woo, Poisoning effect of SO₂ on NO reduction by i-butane over Fe/ZSM-5 prepared by sublimation method, *J. Catal.*, 203, 369-374 (2001).

Patents

S.I. Woo, D.K. Kim and D.H. Kim, Catalyst for automotive lean-burn engine and process for preparing the same, US Patent 6627167 (30. Sep. 2003).

S.I. Woo, D.K. Kim and D.H. Kim, Catalyst for automotive lean-burn engine and process for preparing the same, Korea Patent 0389120 (13. Jun. 2003).

S.I. Woo, D.K. Kim and D.H. Kim, Catalyst for automotive lean-burn engine and process for preparing the same, Australian Patent 734958 (20. Oct. 2000).

S.I. Woo, D.K. Kim and D.H. Kim, Catalyst for automotive lean-burn engine and process for preparing the same, JP applied number 2000-320811 (2000).

Abstract

High-throughput synthesis and primary screening techniques were utilized in the search for and optimization of new noble metal free autoactivation catalysts for the CO₂ reforming of methane to syngas and new catalysts for the selective oxidation of propane to acrylic acid, and the results were confirmed in conventional studies. In the study of the CO₂ reforming of methane, Ni₁₀Ce₉₀O_x demonstrated a rapid start-up operation and high coking resistance as well as comparable activity relative to the commercial Ni/Al₂O₃ catalyst. Although a slow but continuous catalyst deactivation was recognized for Ni₁₀Ce₉₀O_x, it could be strongly reduced by doping with 15 mol% Zr or Al. The exceptional properties of Ni₁₀Ce₉₀O_x and the effect of Zr doping on the catalytic activity and stability were investigated by X-ray diffraction (XRD) and pulse experimentation.

Hochdurchsatzsynthesen und Screeningmethoden wurden bei der Suche und Optimierung neuer edelmetallfreie selbstreduzierender CO₂ Reformierungskatalysatoren von Methan zu Synthesegas sowie von neuen Katalysatoren für die selektive Oxidation von Propan zu Acrylsäure verwendet und die erhaltenen Ergebnisse wurden mit Hilfe konventioneller Versuche bestätigt. Im Fall der CO₂ Reformierung von Methan zeichnete sich Ni₁₀Ce₉₀O_x gegenüber einem kommerziellen Ni/Al₂O₃ Katalysator zum einen durch eine direkte Operationsbereitschaft ohne etwaige Vorbehandlung und zum anderen durch eine geringe Tendenz zur Verkokung aus, wobei die Aktivitäten beider Materialien vergleichbar war. Dennoch konnte eine langsame kontinuierliche Desaktivierung von Ni₁₀Ce₉₀O_x festgestellt werden, die durch den Zusatz von 15 Mol-% Zr bzw. Al drastisch reduziert werden konnte. Die außergewöhnlichen Eigenschaften von Ni₁₀Ce₉₀O_x und der Einfluss der Dotierung mit Zr auf die jeweilige katalytische Aktivität und Selektivität wurden mit Hilfe von Röntgenbeugungs- sowie Puls-Experimenten untersucht.

Contents

1. Introduction.....	1
1.1. CO ₂ reforming of methane.....	1
1.2. Sol-gel synthesis	9
1.3. Combinatorial chemistry	14
1.4. Selective oxidation of propane to acrylic acid.....	21
1.5. Research objectives	24
2. Results and Discussion	26
2.1. Combinatorial discovery of new catalysts for the CO ₂ reforming of methane	26
2.1.1. Setup of the high-throughput experiment.....	26
2.1.2. High-throughput experiments (generations 1 and 2).....	34
2.1.3. Conventional testing (after generations 1 and 2).....	39
2.1.4. High-throughput experiments (generations 3 and 4).....	45
2.1.5. Conventional testing (after generations 3 and 4).....	47
2.2. Mechanistic study of Ni-Ce mixed oxide	53
2.2.1. Catalyst performance and carbon deposition	53
2.2.2. Characterization of Ni/Al ₂ O ₃ catalyst	57
2.2.3. Characterization of Ni-Ce mixed oxide	59
2.2.4. Pulse experiments.....	64
2.2.5. Suggested mechanism	75
2.3. Composition and dopant effect on Ni-Ce mixed oxide	77
2.3.1. Ni _x Cu _y Ce _z mixed oxides.....	77
2.3.2. Zr _x Ni ₁₀ Ce _{90-x} mixed oxide	87

2.4. Combinatorial discovery of new catalysts for the selective oxidation of propane	94
2.4.1. High-throughput screening (generation 1)	94
2.4.2. High-throughput screening (generation 2)	96
2.4.3. High-throughput screening (optimization of Mo-V-Te-Nb).....	98
3. Experimental.....	99
3.1. High-throughput syntheses of catalyst libraries.....	99
3.2. High-throughput testing of catalyst libraries	103
3.3. Conventional catalyst syntheses	106
3.4. Conventional testing of catalysts	107
3.5. Pulse experiment.....	109
3.6. Catalyst characterization.....	111
4. Summary and Conclusion.....	113
5. References.....	118

List of figures and tables

Figure 1. Equilibrium conversion of the CO ₂ reforming of methane.....	2
Figure 2. Carbon deposition threshold calculated as a function of CO ₂ /CH ₄ ratios.....	5
Figure 3. Three main reactions during sol-gel process.....	10
Figure 4. General hydrolysis reaction under basic and acid conditions.....	11
Figure 5. Effect of pH on hydrolysis and condensation.....	12
Figure 6. Effect of pH on sol-gel network formation.....	13
Figure 7. Flow chart of the high-throughput experimentation in the present study.....	27
Figure 8. Screen print of the library design software Plattenbau.....	28
Figure 9. Image of a stainless-steel library plate.....	29
Figure 10. Cross-section of the assembled reactor.....	30
Figure 11. Screen print of the high-throughput experimental control software TestRig.....	31
Figure 12. Measured temperature distribution across the catalyst library at 600°C.....	33
Figure 13. Reaction products on an identical material in previous reactor and new reactor.....	33
Figure 14. Relative activity (%) of the E _x Zr ₂₀ Al _{80-x} (x = 1, 5, 10) library.....	37
Figure 15. Time dependence of the catalytic activity and stability of Ni ₁₀ Ce ₉₀ and Ni/Al ₂ O ₃	41
Figure 16. Catalytic activity depending on the amount of Ni ₁₀ Ce ₉₀	42
Figure 17. d-TGA profile of used Ni ₁₀ Ce ₉₀ and Ni/Al ₂ O ₃	43
Figure 18. d-TGA profile of fresh Ni ₁₀ Ce ₉₀ without reduction step.....	44
Figure 19. Catalytic activity (%) on the M ₁₅ Ni ₁₀ Ce ₇₅ library.....	46
Figure 20. Catalytic activity (%) of (Al _N , Al _A , Si, Ta, Zr _N , Zr _A) _y Ni ₁₀ Ce _{90-y}	48
Figure 21. Catalytic activity of Al _{A15} Ni ₁₀ Ce ₇₅ and Zr _{N15} Ni ₁₀ Ce ₇₅	49
Figure 22. d-TGA profile of used (Al _{N5} , Al _{N15} , Al _{A15} , Zr _{N15} , Zr _{A5} , Zr _{A15})Ni ₁₀ Ce _{90-y}	49
Figure 23. Catalytic activity of Al _{N15} Ni ₁₀ Ce ₇₅ , Al _{N15} Ni ₁₀ Ce ₇₅ , Zr _{A5} Ni ₁₀ Ce ₈₅ , Zr _{A15} Ni ₁₀ Ce ₇₅	50
Figure 24. Catalytic activity of the best catalysts in high-throughput and conventional tests.....	52

Figure 25. Catalytic activity and stability of 100 mg Ni ₁₀ Ce ₉₀ on different regenerations	56
Figure 26. XRD patterns of as prepared, reduced, tested Ni/Al ₂ O ₃	58
Figure 27. XRD patterns of as prepared, reduced, tested Ni ₁₀ Ce ₉₀	60
Figure 28. Ce 3d XPS spectra of as prepared, reduced, tested Ni ₂₀ Ce ₈₀	63
Figure 29. Example of procedures obtaining pulse data	65
Figure 30. The amount of products from pulses of 15H ₂ -19CH ₄ -15CO ₂ over 20 mg NiO	68
Figure 31. The amount of products from pulses of 15H ₂ -15CH ₄ -15CO ₂ over 4.60 mg NiO	69
Figure 32. The amount of products from pulses of 20CH ₄ -20CO ₂ -20CH ₄ over Ni ₁₀ Ce ₉₀	71
Figure 33. Proposed structure of the oxidized surface species on Pd/CeO ₂ catalyst system	72
Figure 34. The amount of products from pulses of 15H ₂ -15CH ₄ -15CO ₂ over Ni ₁₀ Ce ₉₀	74
Figure 35. Relative catalytic activity of the ternary composition Ni _x Cu _y Ce _z library	79
Figure 36. Approximated relative activity of the ternary composition Ni _x Cu _y Ce _z library	80
Figure 37. Catalytic activity of the Ni _x Ce _{100-x} mixed oxides	81
Figure 38. Catalytic activity of the Ni _x Ce _{100-x} (x = 10, 20, 60, 80) mixed oxides	81
Figure 39. Catalytic activity of Ni ₁₀ Ce ₉₀ and Ni ₂₀ Ce ₈₀	82
Figure 40. d-TGA profile of used Ni ₁₀ Ce ₉₀ and Ni ₂₀ Ce ₈₀	83
Figure 41. XRD patterns of the as prepared Ni ₁₀ Ce ₉₀ and Ni ₂₀ Ce ₈₀	84
Figure 42. Relation between the composition and lattice parameter in Ni _x Ce _{100-x}	86
Figure 43. The amount of products from pulses of 25CH ₄ over 100 mg Ni ₂₀ Ce ₈₀	86
Figure 44. The amount of products from pulses of 35CH ₄ over 100 mg Zr ₁₅ Ni ₁₀ Ce ₇₅	88
Figure 45. d-TGA profile of used Zr _x Ni ₁₀ Ce _{90-x} (x = 5, 15, 45, and 75)	89
Figure 46. Catalytic activity of Zr _{Nx} Ni ₁₀ Ce _{90-x} (x = 5, 15, 45, 75)	90
Figure 47. XRD patterns of the as prepared Zr _x Ni ₁₀ Ce _{90-x}	91
Figure 48. Relation between the composition and lattice parameter in Zr _x Ni ₁₀ Ce _{90-x}	92
Figure 49. Relative performance of V-Cr-Sb, Mo-Cr-Te, Mo-V-Cr oxides	97
Figure 50. Drawing of the reactor parts and their assembly	103

Figure 51. Schematic setup of the high-throughput equipment.	104
Figure 52. Picture of the micro mixer from IMM	105
Figure 53. Schematic setup of the conventional testing.....	107
Figure 54. Operation principle of six-port valve in two positions.	110
Table 1. Sample composition, preparation method, time-on-stream, sample number, and active sample of libraries prepared	36
Table 2. Composition of mixed oxides on the selected prefabricated libraries studied during the primary screening.....	38
Table 3. Physical property, TGA and results of conventional tests of selected catalysts	40
Table 4. Catalytic activity and coking rate on Ni ₁₀ Ce ₉₀ and Ni/Al ₂ O ₃ depending on the different treatment.....	54
Table 5. Conditions of pulse experiments	66
Table 6. The amount of oxygen consumed during the pulse experiments	67
Table 7. Physical property, TGA and results of conventional tests of selected catalysts	84
Table 8. List of chemicals and their solvents for matrix and dopant.....	100
Table 9. Elements used for matrix and dopant	101

1. Introduction

1.1. CO₂ reforming of methane

Concern about the high dependence of our economies on crude oil has generated increasing interest in the use of alternative fuel sources. Biogas, which is produced by anaerobic digestion of biomass such as peat, wood, urban or agriculture waste and landfill, is one of the most attractive renewable energy sources available [1]. The most common sources of biogas are landfill gas and digester gas, which are byproducts of anaerobic decomposition of organic matter and are primarily composed of methane and carbon dioxide. Landfill gas is produced during the decomposition of organic matter in sanitary landfills. Digester gas is manufactured at sewage treatment plants during the treatment of municipal and industrial sewage. Research carried out on the anaerobic digestion of a variety of agricultural wastes indicates that there is a great variability in the composition of the biogas generated. The composition of biogas usually lies within the ranges of 50-70 % CH₄, 25-50 % CO₂, 1-5 % H₂, 0.3-3% N₂ with various minor impurities [2]. Notably, hydrogen sulphide (H₂S), one of minor impurities gives the biogas a bad odor.

Biogas is cheap, readily available, and can be considered a potential energy reserve, for example in combined heat and power generation [3-6] while nowadays it is mainly used for heating and cooking [7]. One of the principal limitations of biogas in certain applications is its variability of composition, not only in different locations but also over time, which presents difficulties in its use in conventional power systems. As the proportion of CO₂ in the biogas increases the fuel becomes progressively more difficult to ignite. In practice, conventional heat engines are not operated at methane levels below 50 %, and hence large quantities of biogas are

presently vented to the atmosphere [8,9]. The methane and carbon dioxide exhausted into the atmosphere are a significant contribution to greenhouse gas emissions and at the same time wasting a potentially clean, renewable energy resource [10].

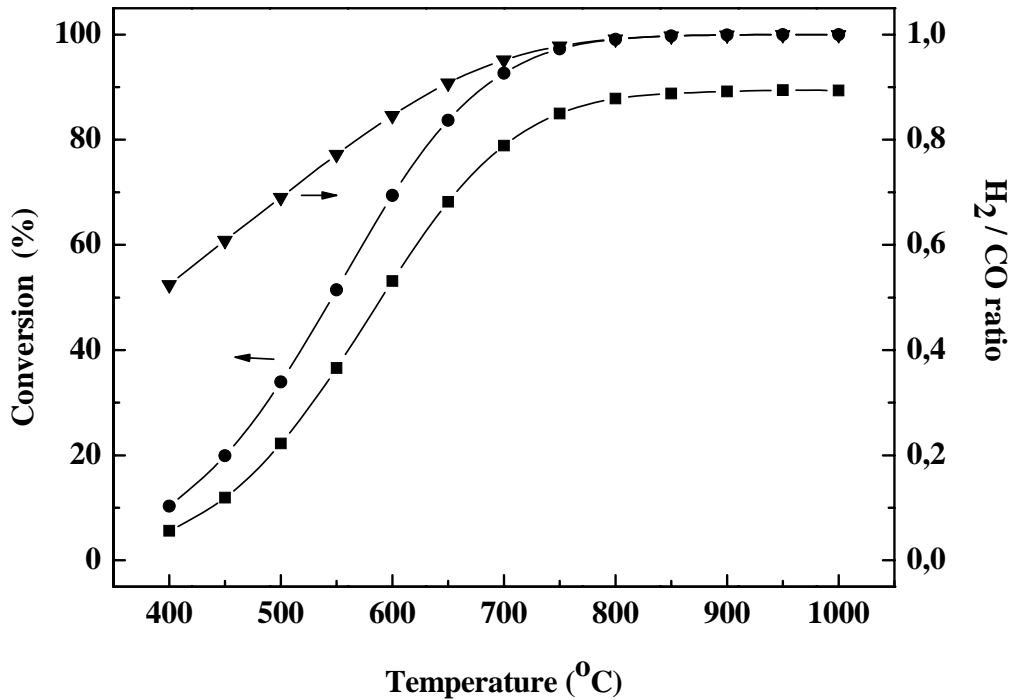


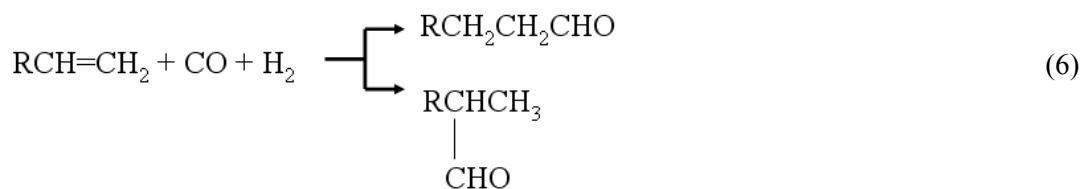
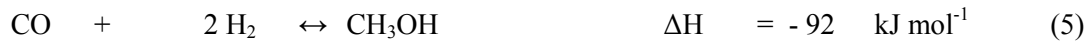
Figure 1. Equilibrium conversion of CH₄ (■) and CO₂ (●) and product ratio of H₂/CO (▼) for the CO₂ reforming of methane as a function of temperature. Operation conditions: P = 1 atm; CH₄/ CO₂/ Ar = 16.9 / 15.1 / 68.

The catalytic reforming of methane with CO₂ (Equation 1), the so called CO₂ reforming of methane or dry reforming, is a particularly elegant way to combine major components of biogas (CH₄ and CO₂) to produce syngas with H₂/CO production ratio of unity [11,12]. This reaction is highly endothermic, and hence it is favoured by low pressure but requires a higher temperature. The undesired reverse water-gas shift (RWGS) reaction occurs as the major side reaction, especially at low temperature (Equation 2).



The equilibrium conversions of both reactant gases and product ratio of H₂/CO for a feed stream at 1 atm total pressure (CH₄ / CO₂ / Ar = 16.9 / 15.1 / 68), calculated using the equiTherm software, are shown in Figure 1. Only over 800 °C did the equilibrium conversions of CH₄ and CO₂ finally reach almost total consumption with a H₂/CO ratio of 1. The CO₂ conversion is always greater than that of CH₄, due to the RWGS reaction.

Syngas is a valuable feedstock for the production of higher hydrocarbons (Fischer-Tropsch synthesis, Equations 3 and 4), methanol (Equation 5), and for hydroformylation processes (Equation 6).



In addition, in conjunction with the water-gas shift (WGS) reaction, it may be applied to produce hydrogen, the main feed gas for fuel cell applications and ammonia synthesis [13]. One potential advantage of CO₂ reforming of methane that would have an impact on the industrial sector is the lower H₂/CO product ratio, compared with steam reforming (Equation 7) and partial oxidation (Equation 8) to produce syngas with H₂/CO production ratio of 3 and 2, respectively.



The lower H₂/CO product ratio is desirable for direct use as feedstock for oxo-synthesis (Equation 6), and it also introduces the possibility of combining the steam reforming, partial oxidation, and CO₂ reforming of methane reactions to control the desirable H₂/CO product ratio [14 -18]. Because of the high endothermicity of the reaction, CO₂ reforming of methane is also used as a chemical energy storage and energy transmission system (CETS) [15,19]. Solar energy is used to drive the endothermic forward reaction, and the energy thus stored can be transported via pipelines as syngas and liberated at will by the reverse reaction at any location or time.

The disadvantage of the CO₂ reforming of methane is the carbon deposition under certain conditions. Carbon deposition mainly results from methane cracking and the Boudouard reaction where C_s refers to surface carbon (Equations 9 and 10). The former is an endothermic reaction, thermodynamically favored at higher temperatures and under lower pressures, while the latter is an exothermic reaction and thermodynamically favored at lower temperatures and higher pressures [20].



Clearly, carbon deposition is thermodynamically possible for CO₂/CH₄ ratios of unity at temperature up to 1000 °C at 1 atm and 1100 °C at 10 atm. In addition, at a given pressure, the temperature limit increases as the CO₂/CH₄ ratios decreases as shown in Figure 2 [19,21,22]. Operation at high temperature and with CO₂/CH₄ ratios far above unity is required to avoid carbon formation. However, from an industrial point of view, it may be desirable to operate at lower temperature with CO₂/CH₄ ratios near unity. This necessitates the use of a catalyst which

incorporates a kinetic inhibition of carbon formation under conditions where deposition is thermodynamically favourable.

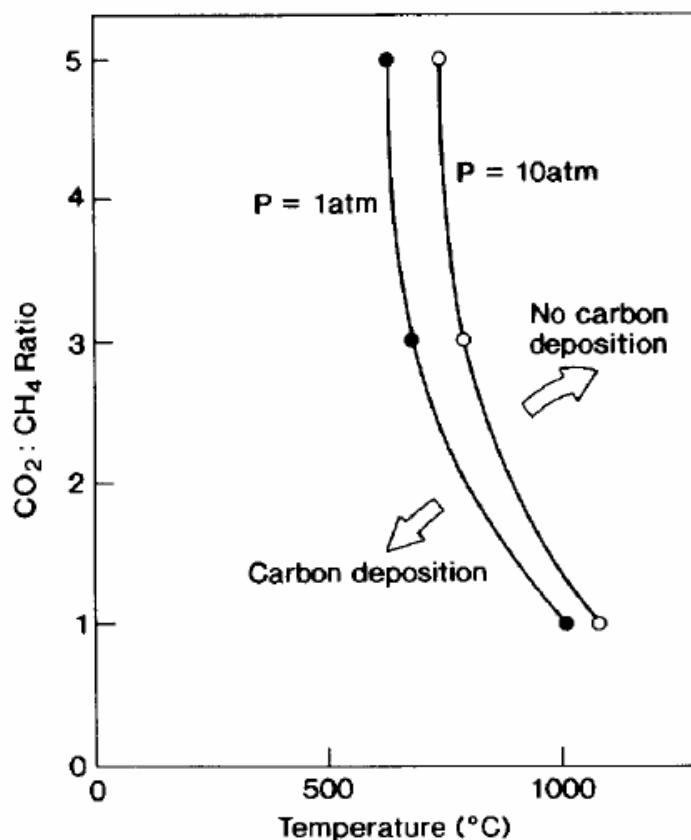


Figure 2. Carbon deposition threshold calculated as a function of CO₂/CH₄ ratios [19].

When distributed in reduced form on suitable supports, Group VIII metals (including Ni, Ru, Rh, Pd, Ir, and Pt) become effective catalysts for the CO₂ reforming of methane [15,19,23-25]. The conversions approaching those defined by thermodynamic equilibrium can be obtained over most of the nickel and noble metal based catalysts, as long as contact times are kept long enough [26]. The catalysts based on noble metals are reported to be less sensitive to coking compared to the nickel-based catalysts [27]. Particularly, Rh was observed to be the best element in the CO₂ reforming of methane after considering the overall performance criteria containing high activity and carbon-free operation [19]. However, for economic reasons (low cost and high availability), most state-of-the-art technologies are based on nickel catalysts. In

fact, Ni on alumina support with alkaline dopants such as K_2O , MgO , or CaO is commercially used in the steam reforming reaction, but in the CO_2 reforming of methane the nickel catalysts are susceptible to a severe, inactive carbon deposition leading to reactor plugging. Although the carbon deposition does not immediately deactivate the Ni particles on the catalyst, prolonged carbon formation can result in complete encapsulation of Ni particles by polymorphic graphite [8]. Several novel Ni-based catalysts or methods improving the coke resistance for long-term stability have been developed and are reported below.

- (i) Carbon deposition can be suppressed when TiO_2 [28], La_2O_3 [29,30], ZrO_2 [31], MgO [32], CeO_2 [20,33], $Y-CeO_2$ [34] $Ce-ZrO_2/\theta-Al_2O_3$ [35], CaO/Al_2O_3 [26], $Ce-ZrO_2$ [36-39], or perovskite [40] is used as support for Ni catalysts.
- (ii) The resistance towards coking can be improved when a metal oxide with strong Lewis basicity (Li, Na, K, Mg, Ca) [41-45] or Mn [46-48], Mo [49], La [50,51], Ce [52], Sn [53], V [54], or Cr [55] is added on Ni/Al_2O_3 as a dopant.
- (iii) The catalyst structure appears to affect the carbon deposition. The formation of $NiAl_2O_4$ during the pretreatment procedure causes a marked decrease in coke deposition [41]. The solid solution of $NiO-MgO$ [32,56,57] has been reported to enhance catalyst lifetime by decreasing carbon formation. This is related to the small nickel crystallites which are stable towards sintering and carbon formation. However, in these cases a reduced catalytic activity is a resulting problem.
- (iv) Catalysts prepared by sol-gel processes, such as $La_{0.8}Pr_{0.2}NiAl_{11}O_{19}$ [58], La_2NiO_4 [59], $NiO-La_2O_3-Al_2O_3$ [51], Ni/SiO_2 [60], La_2NiO_4/Al_2O_3 [50], Ni/Al_2O_3 [61-64], Co/Al_2O_3 [65], or Ni/SiO_2 [66] show that the amount of carbon deposition and the degree of catalytic deactivation are smaller compared to catalysts prepared by impregnation processes.
- (v) Carbon deposition can be more suppressed in the fluidized-bed reactor than in the fixed-bed reactor [3,67-69].

- (vi) The SPARG process, namely sulphur passivated reforming, has been studied to resolve the problem of carbon formation [70]. Carbon formation and growth on Ni-based reforming catalysts require an ensemble of 6 or 7 atoms of Ni, whereas the CH₄ reforming reaction requires ensembles with only 3 or 4 atoms of Ni [19]. Sulphur may block the nickel catalyst surface, which means that nickel cannot catalyze the formation of carbon because of the ensemble effect. However, the passivation process suffers from lower catalytic activity and high operating temperatures.
- (vii) The addition of a small amount of steam was tried to reduce carbon formation. When CO₂ reforming was carried out simultaneously with steam reforming on Ni/CaO-Al₂O₃ catalyst significant increase in methane conversion and decrease in carbon deposition occurs, but H₂/CO production ratio was higher than 1 with the addition of water [26].

Besides catalytic activity and stability, instant catalytic activity without the necessity of previous reduction with hydrogen, and the capacity for intermittent operation are essential properties for the use of the catalyst in reformers for portable and small-scale stationary fuel cells. The Company Umicore developed precious metal-based catalysts, protonicsTM, for autothermal reforming and heated steam reforming in fuel cell systems [71]. These catalysts are non-pyrophoric, do not require preactivation or conditioning after assembly and offer safe operation under all conditions [71]. However, only few reports are available for such catalysts [72,73]. In both industrial and academic studies, precious metal-based catalysts are dominating the published investigations.

Two mechanisms have been proposed for the CO₂ reforming of methane over group VIII metal catalysts. One is the Eley–Rideal type mechanism in which methane is adsorbed and decomposed on the metallic sites to form H₂ and surface carbon [27,74,75]. This carbon species reacts directly with CO₂ from the gas phase to form CO. In the alternative mechanism methane is decomposed on the metal to yield a surface CH_x species and hydrogen [76,77]. CO₂ is also

adsorbed dissociatively on the metal or on the interface of the metal and support oxide under formation of CO and adsorbed oxygen or surface OH groups. These oxygen species react with CH_x to form CO and H_2 . A large number of researches suggest that both mechanisms can be operative, which greatly depends on the nature of the metals as well as the supports [78 -82].

1.2. Sol-gel synthesis

Interest in the sol-gel processing of inorganic ceramic and glass materials began as early as the mid-1800s on silica gels studies [83]. These early investigators observed that the hydrolysis of tetraethyl orthosilicate (TEOS), $\text{Si}(\text{OC}_2\text{H}_5)_4$, under acidic conditions yielded SiO_2 in the form of a glass-like material. The motivation for sol-gel processing is primarily the potentially higher purity and homogeneity and the lower processing temperatures associated with sol-gels compared to traditional glass melting or ceramic powder methods. Many specific applications include optics, protective and porous films, optical coatings, window insulators, dielectric and electronic coatings, high temperature superconductors, reinforcement fibers, filters, sensors, membranes and catalysts [84,85]. In the preparation of catalysts with sol-gel processes, one can start with the molecular precursors of the mixed oxides. Thus, a greater degree of control over the catalysts preparation can be achieved in comparison to traditional methods [86]. The advantages of sol-gel processing for preparation of catalysts include: (i) superior homogeneity and purity, (ii) better microstructural control of metallic particles, (iii) higher BET surface area, (iv) improved thermal stability of the supported metals, (v) control of well-defined pore size distributions, (vi) the ease with which additional elements can be added, (vii) versatility of synthesis method for most elements of the periodic system, and (viii) simple preparation conditions with no necessity of extra steps such as filtration, reflux, and distillation [87-90].

The sol-gel process, as the name implies, involves the evolution of inorganic networks through the formation of a colloidal suspension (sol) and gelation of the sol to form a network in a continuous liquid phase (gel). Colloids are solid particles with diameters of 1-100 nm. A gel is an interconnected, rigid network with pores of submicrometer dimensions and polymeric chains whose average length is greater than a micrometer. The precursors for synthesizing these

colloids consist of metals surrounded by various reactive ligands. Metal alkoxides are most popular precursors. At the functional group level, three reactions are generally used to describe the sol-gel process: hydrolysis, water condensation, and alcohol condensation. This general reaction scheme can be seen in Figure 3.

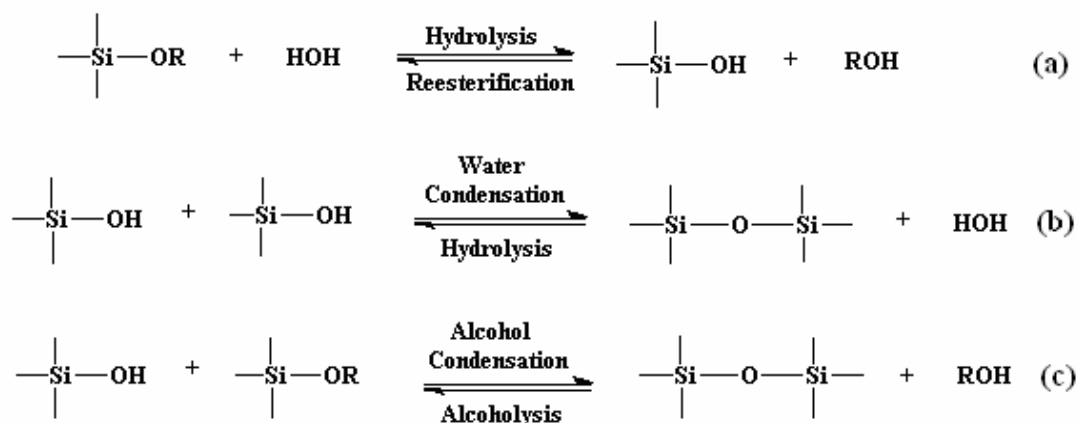


Figure 3. Three main reactions during sol-gel process: (a) hydrolysis, (b) water condensation, and (c) alcohol condensation.

The hydrolysis reaction, through the addition of water, replaces alkoxide groups (OR) with hydroxyl groups (OH). Subsequent condensation reactions involving the silanol groups (Si-OH) produce siloxane bonds (Si-O-Si) and water or alcohol as by-products. The characteristics and properties of a particular sol-gel inorganic network are related to a number of factors that affect the rate of hydrolysis and condensation reactions, such as pH, temperature and time of reaction, reagent concentrations, catalyst nature and concentration, H₂O/Si molar ratio (R), aging temperature and time, and drying [91]. Of the factors listed above, pH, nature and concentration of catalyst, H₂O/Si molar ratio (R), and temperature have been identified as most important. Thus, by controlling these factors, it is possible to vary the structure and properties of the sol-gel derived inorganic network over wide ranges [91]. When the pore liquid is removed as a gas phase from the interconnected solid gel network under hypercritical conditions (critical-point

drying), the network does not collapse and a low density aerogel is produced. On the other hand, when the pore liquid is removed at near ambient pressure by heat treatment and shrinkage occurs, the resulting monolith is termed a xerogel.

The sol-gel process may be performed under acidic conditions (pH 1.5-6), basic conditions (pH 8-11), or neutral conditions (pH 7). Different catalysts can be used to accelerate the hydrolysis reactions. Under acid conditions, strong acids such as HCl, H₂SO₄, HNO₃ may be used as catalysts. Weak acids or weak bases such as acetic, oxalic, formic or ammonia may also be used. The general hydrolysis reactions under basic and acid conditions are schematically shown in Figure 4.

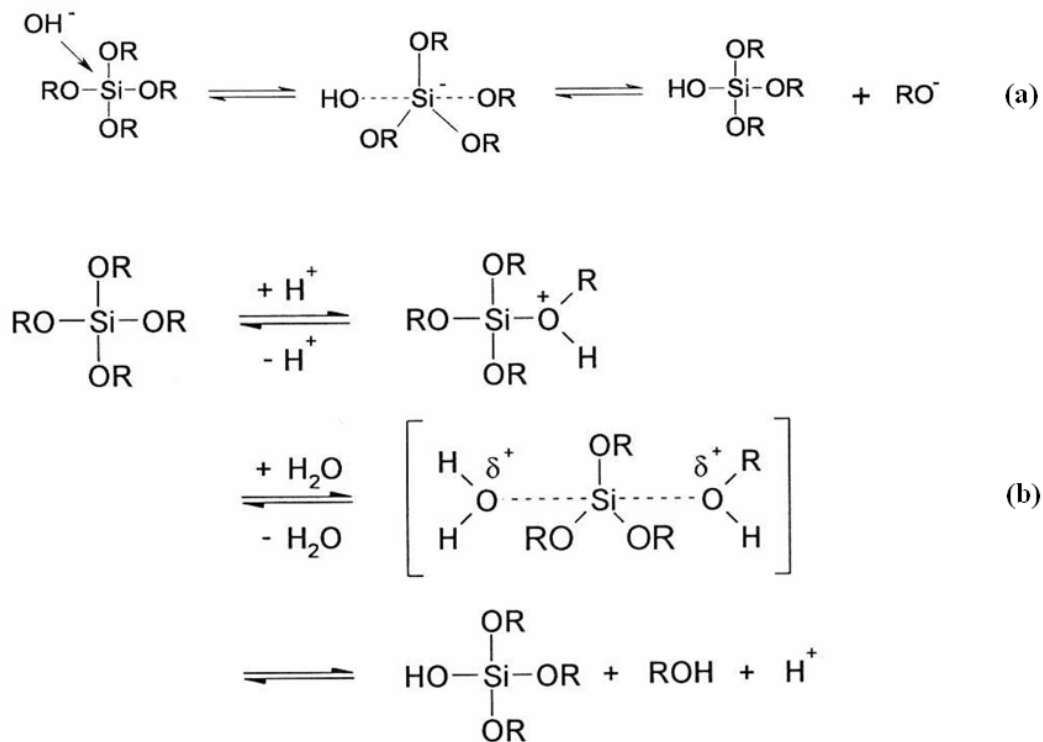


Figure 4. General hydrolysis reaction under (a) basic and (b) acid conditions during sol-gel process.

In the case of hydrolysis under basic conditions (see Figure 4a), the hydroxyl anion attacks the silicon atom and hydroxyl groups (OH) displaces alkoxide groups (OR) with inversion of the silicon tetrahedron. When base-catalyzed sol-gel methods are applied to prepare mixed oxide,

phase separations can be formed because hydrolysis and condensation are controlled by the electronegativity of the central atoms. In the case of hydrolysis under acidic conditions (see Figure 4b), it is likely that an alkoxide group is protonated in a rapid first step. Electron density is withdrawn from the silicon atom, making it more electrophilic and thus more susceptible to attack from water. This results in the formation of a penta-coordinate transition state which decays by displacement of an alcohol and inversion of the silicon tetrahedron [92]. When acid-catalyzed sol-gel methods are applied to prepare mixed oxides, uniform mixed oxides can be formed without discrimination by electronegativity since hydrolysis and condensation are controlled by the lone pair on the oxygen atoms.

Relative reaction rate of hydrolysis and condensation as a function of pH is revealed in Figure 5. Under acidic conditions, hydrolysis rate is faster than condensation rate resulting in weakly branched gel. Conversely, hydrolysis rate is slower than condensation rate under basic conditions resulting in highly branched gel.

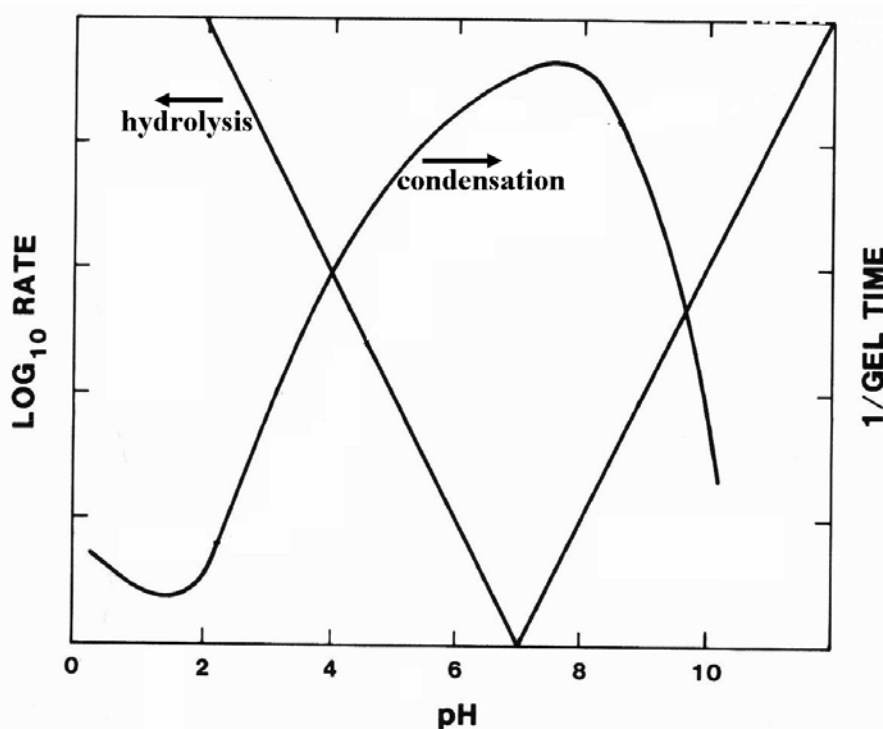


Figure 5. Effect of pH on hydrolysis and condensation [92].

Therefore, although many factors affect the resulting sol-gel network, it can generally be said that sol-gel networks under acid-catalyzed conditions yield primarily linear or randomly branched polymers which entangle and form additional branches resulting in gelation. On the other hand, sol-gel networks under base-catalyzed conditions yield more highly branched clusters which do not interpenetrate prior to gelation and thus behave as discrete clusters (see Figure 6).

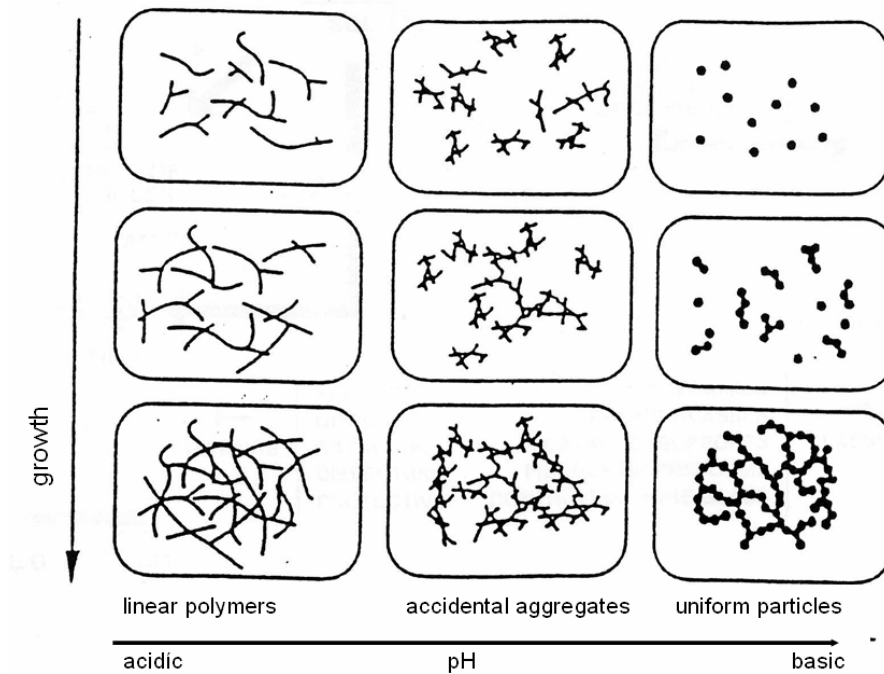


Figure 6. Effect of pH on sol-gel network formation [93].

1.3. Combinatorial chemistry

Combinatorial methods, which established its importance for drug development, have been applied increasingly in the field of materials research and catalysts development. Combinatorial chemistry is the systematic preparation, processing, testing, and characterization of large diversities of chemically and physically different materials libraries in a high-throughput fashion, and modeling of the vast amount of data generated [94]. The discovery and development of new materials and catalysts used to be a time consuming and rather unpredictable trial-and-error process. However, combinatorial and high-throughput approaches are changing this perception. This technology is aimed to speed up the pace of research leading to increase the chances of discovery of totally new and unexpected materials and catalysts and their optimization. Also, combinatorial methods can significantly contribute to our understanding of catalytic function by expediting the recognition of trends and patterns of many variables to affect desirable properties, from which new catalytic materials can be designed more efficiently. From an industrial view, combinatorial chemistry and high-throughput experimentation (HTE) opened the new paradigm of industrial materials and catalysis research. Due to the enormous industrial impact of the development of better materials and catalysts a number of new companies is already active in this field, namely Symyx Technologies, HTE Aktiengesellschaft, Avantium, AMTEC, IMM, SINTEF, and combinatorial chemistry is now core technology in many major chemical and material companies such as BASF, Bosch, Degussa, UOP, P&G, GE, Bayer, DuPont, DOW, and many others.

Already in 1970, this concept was used initially by Hanak to search for a new semiconductor [95]. Schultz and co-workers demonstrated the application in the search of solid material libraries for superconductivity and magnetoresistance [96]. Those investigations initiated the application of HTE in material sciences and later also in heterogeneous catalysis

[97]. The development and application of high-throughput methods for the rapid discovery and optimization of solid-state catalysts and materials has experienced significant growth, as described in the exponential growth of its scientific publications number [98]. It is also proving the speed and economic advantage of combinatorial approaches by the discovery of superior catalysts and materials in a matter of hours and days, as opposed to the months and years required using traditional methods [99,100].

The general approach used in combinatorial chemistry is based on the current understanding gained from pharmaceutical and biochemical research. However, the use of combinatorial and high-throughput experimentation to inorganic materials, particularly to heterogeneous catalysts is substantially different from that in pharmaceutical study or organic chemistry. The additional challenges arise from the complex and dynamic properties of catalysts. First, real solid-state catalysts generally contain multiple discontinuities in structure and composition allowing very limited systematic variation for their desirable properties [94]. In addition, these structures are strongly dependent on many variables such as preparation methods, pre- or after treatment, and reaction conditions. For example, preparation of 100 catalysts of the identical chemical composition by different synthesis procedures and different pre- or after treatments will result in 100 materials of different catalytic activity, ranging most likely from inactive to highly active. Thus, it is essential, that all materials in a combinatorial study are prepared by the same recipe in order to provide the same microstructure. Only then may the results be comparable. Second, many catalysts only attain their desirable properties after a certain time on stream for catalysts formation and deactivation processes such as surface reconstruction, sintering, poisoning, coke formation, and volatilization. Finally, the reaction conditions for practical testing typically require elevated temperatures and pressures, and various gases or liquid streams that might be flammable or toxic.

The preparation of inorganic material libraries has been accomplished by using techniques of thin film deposition and solution-based methods. The thin film deposition with

physical masking provides access to materials libraries with spatial resolution. Schultz and co-workers initially demonstrated such an approach with a library of 128 components prepared by masking and radio frequency (RF) sputtering for the discovery of new superconducting materials [96]. Just two years later, Symyx technologies perfected this technique in the searching for new luminescent materials on three libraries containing 25,000 discrete materials prepared by the combination of masking with physical vapour deposition (PVD) [101]. The same method was also used for the discovery and optimization of new catalysts for the CO oxidation reaction [102] and the oxidative dehydrogenation of ethane to ethylene [103]. Since with sputtering a large number of sites can be prepared simultaneously with very high speed, this technique can be a useful tool for the creation of very large libraries. However, a successful scale-up of discovered compounds, especially catalysts, is a challenging problem since physical and chemical properties that influence the catalytic activity may be very different between the thin film and powder-form catalyst. Other thin-film deposition methods, such as thermal [104] and plasma chemical-vapour deposition [105,106], molecular beam epitaxy [107], and pulsed-laser deposition [108,109] have been developed. The solution-based methods involve sol-gel, impregnation, hydrothermal synthesis, coprecipitation, and polymerization. Conventional synthesis robots and a library containing predefined positions in the form of little wells are used for this approach. The use of an ink-jet print technique was successfully adapted to prepare a 645 combination Pt-Ru-Os-Ir library for the reforming of methanol [110]. The application of sol-gel synthesis in catalysis library preparation has been introduced by Maier and co-workers, particularly for the synthesis of amorphous mixed oxides [111]. Symyx Technologies created arrays of thin films that are spatially separated catalysts libraries from stabilized sol-gel precursors [112].

High-throughput testing of heterogeneous catalysts has been one of the most crucial parts in combinatorial chemistry in order to obtain meaningful and reliable data. The high-throughput screening has been achieved by the development and application of miniaturized and

fast reactor systems coupled to suitable analysis tools. As in pharmaceutical discovery, the most promising strategy appears to be a two-stage approach, e.g., primary screening and secondary screening. The primary screening allows a very large number of compounds with high diversity to be tested at a relatively imprecise level, and provides a reasonable relative ranking of the library. In the secondary screening catalysts are evaluated in more detail under conditions close to those of conventional testing at more accurate level. However, the clear discrimination of methods between the primary and secondary screening is quite ambiguous.

For primary screening, various techniques such as optical methods and spatially resolved mass spectrometry (MS) or gas chromatograph (GC) were used. The optical screening method includes the colour indicator method [113], infrared (IR) thermography, Fourier transform infrared (FTIR), laser induced fluorescence imaging (LIFI) [114], resonance-enhanced multiphoton ionization (REMPI) [115], and photothermal deflection (PTD). IR thermography is used to register radiation energies, which can be correlated to heats of reaction. Wilson and co-workers used thermography in the parallel analysis of catalysts [97]. These were arrayed as pellets on an alumina disk and screened for the catalytic activity of hydrogen oxidation. The method has been refined by Maier and co-workers by adding a background correction to improve the temperature resolution [116]. Using this correction technique, temperature differences of 0.1 K can be analyzed reliably, even at elevated temperature. Although IR thermography is an extremely fast and nonintrusive screening technique monitoring large numbers of samples through the visualization of reaction heats, it does not provide information on the chemical identity of the products formed in a reaction. FTIR spectrometry can also be used to screen libraries of solid-state catalytic materials [117,118]. The FTIR approach provides a significant improvement over IR thermography as it provides chemically specific information. However, the detection of gas-phase species at low concentrations creates a challenge that must be addressed for the effective use. The adaptation of mass spectrometry to high-throughput testing of heterogeneous catalysts has been reported in

several approaches independently in 1999. An especially developed MS screening reactor was reported by Symyx Technologies, which monitors product composition sequentially by quadrupole mass spectrometry (QMS). In a reaction chamber the catalyst spots on a flat library are heated from the back by a CO₂ laser beam, while on the opposite side the catalyst sample is supplied with the feed gas mixture from one capillary and simultaneously a small part of the feed-product mixture is transported to and analyzed by the MS [102,103]. Senkan and co-workers reported a heated gas phase flow reactor with multiple channels in a ceramic block, sampled sequentially by a QMS. Here the reactor is moved by a xyz stage to insert the fixed inlet tube of the MS into the exit opening of individual reactor outlets for sampling [119]. At the same time Maier and co-workers reported a system based on the use of plate libraries, where individual catalysts have been placed in wells and monitored in the open-well by a moving capillary, which is connected to the MS and GC [120]. Claus and co-workers reported the use of a monolithic reactor system with up to 250 catalysts in parallel in combination with QMS [121,122].

More complicated reactor designs are required for the secondary screening. Generally, a reliable multichannel reactor should satisfy three conditions: accurate amount of catalyst loading, narrow temperature distribution, and uniform reactant flow rate at each channel. A 15-fold glass tube parallel reactor was introduced by Rodemerck and co-workers close to conventional catalyst testing equipment [123]. Analysis of the products for each catalyst was performed sequentially, using a multi-position valve and QMS. More recently, an analogous 16-bed microreactor setup has been presented by Mirodatos and co-workers and commercialized by the AMTEC company [124]. Here a combination of QMS and fast GC was used as analysis tools. Advanced parallel fixed-bed reactors, typically with 48 channels in parallel, were presented by Symyx Technologies [125]. Here, an equal feed distribution over the different catalyst beds was ensured by using upstream capillaries. Schüth and co-workers developed a number of high-throughput reactors close to conventional testing methods with different degrees

of sample integration. A 16-channel parallel brass reactor [126] and an advanced 49-fold parallel reactor which consists of a stainless steel body [127] connected via capillaries to a multiport valve. In addition, many research groups have fabricated the various types of reactor system for the secondary screening [128 -132].

Although large numbers of samples can be generated and tested by means of HTE, the possible number of compositions is almost infinite. For example, the possible number of organic molecules based on the known structural diversity of just the five elements carbon, oxygen, nitrogen, sulphur and hydrogen has been estimated to 10^{63} [133]. Preparing only 1 mg each a total mass of 10^{60} g would be obtained. The total mass of our sun is approximately 2×10^{33} g, the total mass of the known universe has been estimated to 10^{58} g, indicating that this limited organic library from just five elements is equivalent to 100 times the mass of the universe [134]. If we allow for 75 useful elements the possible chemical diversity clearly exceeds comprehension [135]. Moreover, as the structural and functional complexity of heterogeneous catalysts, the diverse parameters such as the conditions of preparation (method, recipe, temperature, pressure), mixing, milling, pre- or after treatment (drying, calcination, reduction), and operating (temperature, pressure, GHSV, reactant concentration, time-on-stream, deactivation) should also be considered as independent variables. Considering this large parameter space, combinatorial techniques represent the most rational approach for the discovery and optimization of new catalytic materials. However, as mentioned above, even using HTE, only a small fraction of this large parameter space can be searched. Therefore, one of the most important key points of combinatorial chemistry research should be to build representative libraries that ensure the greater probability of obtaining hits for a given reaction. For this purpose, effective combinatorial experiment planning, namely design of experiment (DOE), is required to organize the experimental work into a minimum of work input and maximal information output. In the design of experiment, all factors that affect the result are considered simultaneously in a planned set of experiments, and then the correlation of the

factors among each other and their importance to the result can be estimated. In the beginning of high-throughput experimentation two possible starting situations can be identified [136]. First, screening is based on prior information and catalytic systems are available which show some activity for the desired reaction (optimization program). Second, there is essentially no precedence of a catalyst, or the systems previously investigated do not seem to have the potential for further improvement (discovery program). In the optimization program, relevant and potentially relevant factors are thought to be known so that libraries can be designed in a well defined frame. Library design would concentrate on compositions or a limited parameter space around system, and the selected parameter are varied in a systematic and efficient way. Some tools such as statistical DOE, evolutionary algorithms, or neural networks have been used for this purpose. Genetic algorithms (one of evolutionary algorithms) combined with neural networks have been successfully applied to the optimization of heterogeneous catalysts for the oxidative dehydrogenation of propane [137], the low temperature oxidation of propane [138], the low temperature light paraffin isomerization [139], and selective oxidation of propane [140]. In the discovery program, diversity methods are used to sample an existing collection of molecules or materials of a predefined experimental space. The methods are intended to optimize some property of an ensemble of samples. The groups of Schüth and Mirodatos investigated the catalytic performance of 467 catalysts of different origin and prepared by various methods for the oxidation of propene [136]. The authors searched for general descriptors that correlate with the catalytic activity described by the dataset [141]. In the dataset, parameters such as mean electron affinity, mean electronegativity or mean molar mass of all elements in the catalysts were identified as descriptors, while chemical composition does not correlate with the function of the materials [136]. This was to be expected, since catalytic performance is a function of preparation much as it is a function of composition.

1.4. Selective oxidation of propane to acrylic acid

Selective transformation of low molecular weight alkanes into more valuable products is a challenging task. Oxidative catalytic processes are considered as promising in this sense. Selective oxidation is one of the most important strategies for the transformation of raw materials into more valuable components, since it produces worldwide about 25% of the industrial organic chemicals and intermediates used for the production of fine chemicals, pharmaceuticals, etc. [142]. The direct oxidation of propane to acrylic acid has attracted a lot of attention in the past decade in both academia and industry, since it attempts to reduce a three step reaction into a one step process.

In industry, most acrylic acid and esters have been manufactured by the Reppe process. In the newer plants propene oxidation predominates. It can be conducted catalytically either as a single-step or as a two-step process. In the single-step direct oxidation, propene is reacted with air or oxygen (sometimes diluted with steam) at up to 10 bar and 200-500 °C, depending on the catalyst. The multicomponent catalyst mainly consists of heavy metal molybdates, and generally contains tellurium compounds as promoters. Acrolein and acrylic acid are formed sequentially (Equations 11 and 12).



As both oxidation steps have different kinetics, uniform process conditions and a single catalyst would not lead to optimal acrylic acid selectivity. For this reason, numerous firms developed two-step processes with an optimal coordination of catalyst and process variables, and the first industrial single-step process (Japan Catalytic Chem. Ind.) has been converted to the two-step

process [143].

To date, the industrial production of acrylic acid involves a two-step process, which consists of the propene oxidation to acrolein followed by the oxidation of acrolein to acrylic acid. While the processes are essentially the same, there are marked differences in the catalyst compositions. As in the single step process, they contain mixed oxides, the main component being molybdenum on supports of low surface area. The promoters for the two steps are vastly different. In the first step, propene is generally oxidized to acrolein over multicomponent Mo-Bi-Co-Fe based oxide catalysts in the presence of steam and air at 330-370 °C and 1-2 bar. The exothermic reaction is conducted in a fixed-bed tubular reactor with up to 22,000 tubes per reactor. The reaction products are fed directly into a second reactor where they are further oxidized over Mo-V based oxide catalysts at 260-300 °C to acrylic acid. The propene and acrolein conversion are over 95 %, with a selectivity to acrylic acid of 85-90 %, based on propene. Water is generally added to the reactant for the purpose of shift of explosion limit, improvement in desorption from catalyst, and facilitation of heat removal. The large excess of water leads to an aqueous solution of 20-25 % acrylic acid, from which the acid is generally isolated by extraction and separated from the byproducts such as acetic acid, propionic acid, maleic acid, acetaldehyde, and acetone by distillation. In a newer separation method from BASF, acrylic acid is removed from the reaction gases by absorption in hydrophobic solvents (e.g., diphenyl/diphenyl ether mixtures) and purified by distillation.

The one-step direct conversion of propane to acrylic acid has especially attracted many research interests, since propane is much cheaper than propene. By now, three categories of catalyst systems, vanadium pyrophosphate (VPO) type catalysts [144,145], heteropoly compounds catalysts [146,147] and multi-component or mixed metal oxides catalysts (MMO) [148-150], have been studied for the direct oxidation of propane to acrylic acid. MMO catalysts are commonly considered to be good candidates. Among those MMO catalysts systems, the most promising catalyst appears to be the Mo-V-Te-Nb mixed oxide catalyst, initially proposed

by Mitsubishi Chemicals, which is reported to achieve more than 40% of acrylic acid yield [151]. An appropriate Mo-V-Te-Nb metal ratio is critical for the formation of high catalytic activity. According to the patent of Ushikubo [149], the catalysts with metal ratio of $\text{Mo}_1\text{V}_{0.3}\text{Te}_{0.23}\text{Nb}_{0.12}$ show excellent catalytic performance for selective oxidation of propane to acrylic acid. However, no catalyst systems have been reported for the direct oxidation of propane, which are active and selective enough for industrial application. The oxidation of propane take place via several different pathways, leading to the formation of many partial oxidation products such as propene, acrolein, acetone, acrylic, propionic, and acetic acids as well as carbon oxide and water. This reaction is generally believed to proceed via Mars-Van Krevelen mechanism with incorporation of lattice oxygen to form the aforementioned products followed by catalyst reoxidation by molecular oxygen [152]. The oxidation of propane to acrylic acid requires four lattice oxygen atoms, abstraction of four hydrogen atoms from the substrate, insertion of two oxygen atoms from the lattice, and transfer of eight electrons, i.e., a coordinated action of the active sites as well as balanced redox properties of the catalyst to complete the catalytic cycle.

Acrylic acid and its esters are important monomers for the manufacture of homo- and copolymers. They are used mainly in paints adhesives, in paper and textile finishing, and in leather processing. One important use is as superabsorbents (super absorbent polymers, SAP), that is, as polymers which can soak up extremely high amounts of liquids [143].

1.5. Research objectives

Combinatorial chemistry and high-throughput experimentation (HTE) has additional challenging problems for discovery and optimization of solid-state catalysts while the motivations are similar to those in pharmaceutical and biochemical research. The additional challenges arise from the complex and dynamic properties of catalysts, which strongly dependent on the diverse parameters such as the conditions of preparation, mixing, milling, pre- or after treatment, and operating. Studying CO₂ reforming of methane by high-throughput method also has similar challenging problems: (i) Highly tolerant synthesis method and recipe are required to allow the broad screening and optimization of chemical compositions, since the synthesis of the catalysts of varying composition should be carried out under identical synthetic conditions. (ii) High-heat-resistant screening system is crucial because this reaction requires a high temperature over 600 °C. (iii) During high-throughput testing on each catalyst, time-on-stream should be considered due to the deactivation and activation behaviour of such reforming catalysts. In addition, a certain amount of water in a form of liquid phase should be reliably added to and mixed with reactant gases in the study of selective oxidation of propane to acrylic acid.

In the study of CO₂ reforming of methane, new catalysts based on non-precious metal of high catalytic activity and stability towards coking are required for economic reasons. Moreover, for applications of the reforming catalysts in mobile fuel cells, immediate catalyst start-up is desirable property. Therefore, new noble metal-free catalysts of high catalytic activity, lack of coking, and rapid startup operation with no prereduction step are of great interest in the CO₂ reforming of methane. In the study of direct oxidative conversion of propane to acrylic acid, development of new catalysts with high activity and selectivity to acrylic acid are essential to replace the current two steps process.

Based on these considerations, the research objectives in this study include:

1. Development and application of combinatorial chemistry and high-throughput experimentation tools to investigate catalysts for the CO₂ reforming of methane to syngas and selective oxidation of propane to acrylic acid.
2. Searching for new noble metal-free catalysts of high catalytic activity, lack of coking, and rapid startup operation with no prereduction step in the study of CO₂ reforming of methane by means of combinatorial chemistry and high-throughput experimentation.
3. Confirmation of the properties of the best materials from high-throughput experimentation through scale-up syntheses and conventional gas-phase reaction tests.
4. Characterization of new catalysts in order to understand their properties at a fundamental level by various tools.
5. Searching for new catalytic system of high activity and selectivity in the study of selective oxidation of propane to acrylic acid by means of combinatorial chemistry and high-throughput experimentation.

2. Results and Discussion

2.1. Combinatorial discovery of new catalysts for the CO₂ reforming of methane

2.1.1. Setup of the high-throughput experiment

Efficient implementation of high-throughput experimentation (HTE) requires the complete combinatorial workflow with no bottleneck. The general strategy for high-throughput experimentation in the present study involves not only the discovery and optimization cycles with the creation and evaluation of catalyst libraries but also conventional verification and characterization. The typical HTE procedure in this study is demonstrated in Figure 7. The discovery and optimization cycle containing library design, synthesis and performance testing is carried out until the promising catalysts to satisfy the desired properties are found. The catalysts with promising results are reproduced and validated in conventional manners, and the properties of the new catalysts are characterized. The knowledge extracted from the conventional confirmation and characterization is also used in the design of new libraries leading to another discovery and optimization cycle.

It is well known that the catalytic activity of heterogeneous catalysts is very sensitive to preparation conditions. The function of a catalyst is not defined by composition, but by the exact synthesis protocol, the synthesis procedure, and the precursors used. Changing the sequence of additions and allowing different drying times and calcination temperatures will result in a variety of different materials of identical composition, but different catalytic activity and selectivity. Thus, variations in chemical composition with a wide range of elements must be carried out with a common synthesis procedure that is tolerant to such compositional changes.

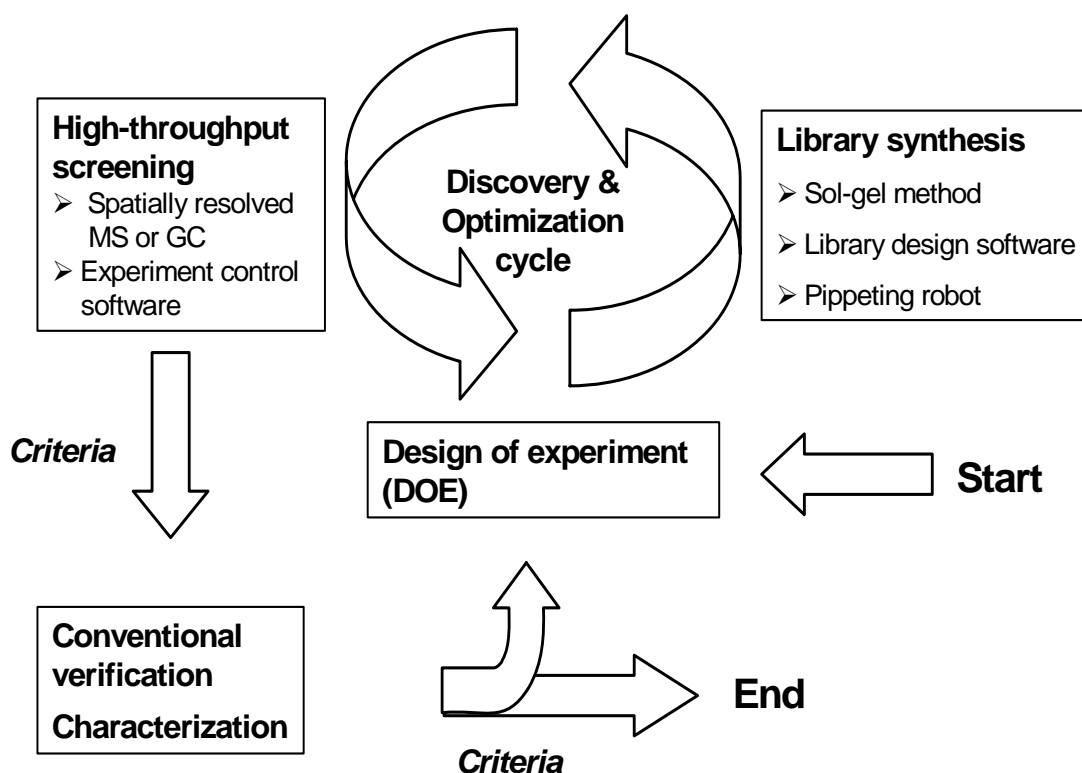


Figure 7. Flow chart of the high-throughput experimentation in the present study.

Many conventional catalyst preparations are not suitable for such a search. Highly tolerant synthesis recipes have been developed in our group, which allow the broad screening of elemental compositions based on sol-gel procedures [85,89,153-155]. These recipes have been used to prepare a large variety of mixed oxides, which can then be tested for catalytic performance. Because all catalyst materials were mixed oxides, and the oxidation state of the oxides was not determined and may change during the experiment (redox processes), the materials are identified only by the metal ions and atomic % given as a subscript; for example, $\text{Nb}_{37}\text{Cs}_{63}$ means a mixed oxide comprising 37% of Nb and 63% of Cs oxides.

The automated synthesis of catalysts was done using a commercial pipetting robot. In the procedure, 1 M matrix and 0.1 M dopant stock solutions were positioned in 10 ml vials and used to formulate the final reaction mixture by transferring the aliquots of each stock solution

into 2-ml vials, positioned in racks of 50 vials. The synthesis of the combinatorial catalyst libraries was accelerated using the Plattenbau library design software (see Figure 8) [156]. This software calculates, based on a parameterized recipe, the volumes of the different solutions of starting materials, as required for the preparation of the individual samples. It also generates an optimized pipetting list, which can be transferred directly to the pipetting robot.

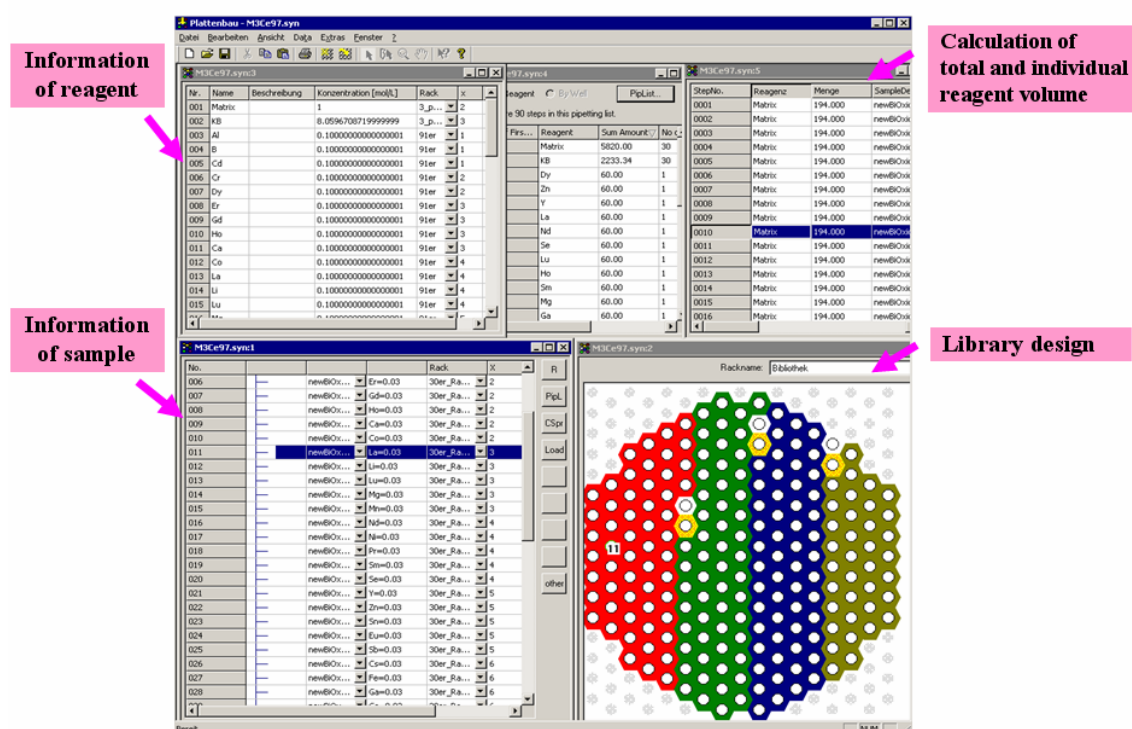


Figure 8. Screen print of the library design software Plattenbau.

Three different kinds of modified sol-gel procedures were applied to prepare libraries depending on the matrix metal precursor used (i.e., method 1 for alkoxide, method 2 for propionate, and method 3 for nitrate, see chapter 3.1). The samples prepared are identified by the central elements with the expected mol% from the composition of the starting sol given in subscripts. Subscripts were also used to distinguish dopant elements based on the different kinds of precursors (i.e., “N” for metal nitrate and “A” for metal alkoxide). The total molar amount of dopant and matrix was set as 200 μmol per sample. After the pipetting process of an entire rack

(50 vials) was completed, this rack was covered and placed on an orbital shaker for 3 h. After removing the lid, the rack was dried for 5 days at 40 °C to allow gel formation and catalyst drying. All samples were calcined in an oven at 65 °C for 5 h and at 250 °C for 5 h. The catalyst powders obtained were crashed with a glass rod in the vials and manually transferred into 207 hexagonally positioned wells (\varnothing 3.5 mm) in a stainless steel library plate (\varnothing 99 mm), as shown in Figure 9. Some wells were left empty for background, and at least one well was filled with a reference catalyst. The activity of each well was obtained from the amount of CO produced on the catalyst and represented relative to the activity of the reference catalyst. Therefore, the relative activity (%) of each sample was defined as [(the amount of CO produced on a sample)/(the amount of CO produced on the reference catalyst) \times 100]. For comparison, 10 mol% Ni catalyst supported on commercial γ -Al₂O₃, referred to as Ni/Al₂O₃, was prepared using the wet impregnation method in a conventional manner and was filled in a well. The library was calcined again in an oven, heated to 700 °C at a heating rate of 2 °C min⁻¹, and kept there for 2 h.



Figure 9. Image of a stainless-steel library plate (\varnothing 99 mm) with 207 hexagonally positioned wells (\varnothing 3.5 mm), filled with catalysts.

Studying CO₂ reforming of methane by high-throughput screening methods is not a trivial task. All attempts to use IR-thermography failed since the reaction is an equilibrium

reaction carried out at high temperatures. Suitable methods include spatially resolved mass spectrometry (MS) or gas chromatograph (GC). The open-well, high-throughput reactor system was previously developed in our group [120,155,157]. In the reactor system, a catalyst library is placed in a special reactor with a heating system and insulation (see Figure 10). On top of the library, a 15-mm-thick ceramic mask with drillings provides additional reaction volume on the top of each well and insulates the library plate to improve the constant of the reaction temperature on the catalyst surface. A capillary bundle containing both the educt gas supply and the product gas sampling system is inserted sequentially into each well of the library plate. The position of the capillary bundle is fixed while the complete reactor is moved by an *xyz*-stage.

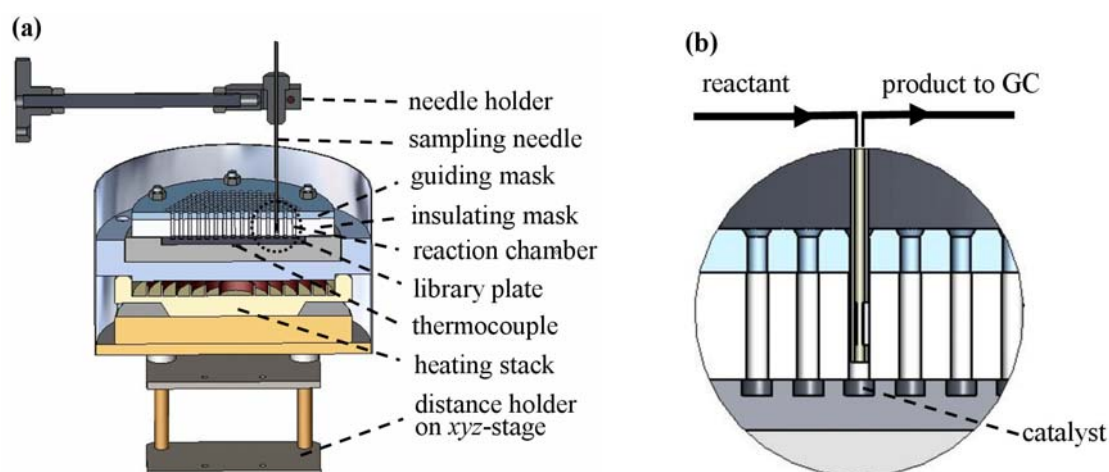


Figure 10. (a) Cross-section of the assembled reactor and (b) magnification of reaction chambers (dotted-circle in (a)).

The high-throughput screening experiment was controlled by the TestRig software written in our group (see Figure 11) [158]. Its function is to simplify the planning and control the flow of the high-throughput screenings by controlling *xyz*-stage movements. This software allows the user by simple pointing or marking to freely define the whole sequence of the high-throughput testing. A panel at the window bottom informs about the status of the HTE. On the left side of the picture the layout of the reaction chambers on the library plate is shown on the

hexagonal array, non-existing positions are shaded. By selecting a well on the library the reactor can be moved to the corresponding position. The window on the right hand side is used to define the sequence of measuring positions. Moreover, this program defines three time settings: an offset time between entering a hole and starting the measurement, a measurement time in each well, and a waiting time between exiting a hole and entering the next one. When GC is to be used as analysis tool as in this study, TestRig controls the automatic start and stop of the GC at each library position.

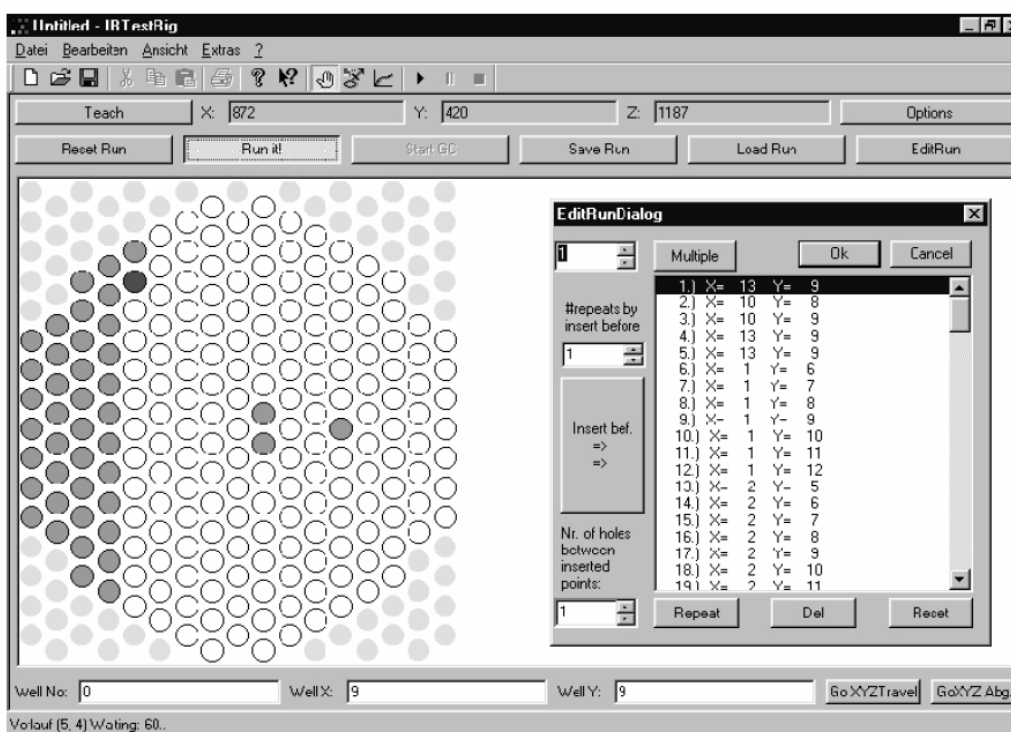


Figure 11. Screen print of the high-throughput experimental control software TestRig.

Our original reactor system could not be used at the temperature range of 600–800 °C needed for this investigation. To improve the thermal stability of the reactor at such high temperatures, the modifications of the previous reactor involving a change in the reactor parts materials and reactor structure was carried out by R. Richter. Whereas the original reactor was constructed from V4A-steel, high-heat-resistant steel was used for all parts of the new reactor.

In addition, a thicker insulating mantle for high temperatures was wrapped around the reactor. The insulating mask was made from MACOR (thickness 12.5 mm) and was in direct contact with the library plate. The arrangement of the tightening screws was changed, as shown in Figure 10a. After these modifications to the reactor, the temperature variation across the library improved, and the library could be heated reliably up to 750 °C. The reactor cross-section is shown in Figure 10.

The library plate temperature was set to 600 °C for each measurement. To assess the quality of the temperature distribution in the library, 29 holes of a library plate had been filled with inert alpha-alumina and the temperature inside the powder had been measured using a thin thermocouple. The temperature distribution over a library plate at 600 °C is shown in Figure 12. The temperature varied from 551 °C to 564 °C. Considering the open construction of the system the temperature distribution is sufficiently uniform for a primary screening device. Reaching 600 °C at the library surface took about 1 h, and stabilizing the library plate temperature took another 2 h. Also, this stabilization time which was set to a standard value of 2 h improves the reproducibility of the data since the time between the start and the measurement of an individual catalyst leads to additional calcinations time that probably stabilizes the absolute catalyst activity.

Because of the open construction of the reactor (see Figure 10), oxygen and moisture from the ambient air cannot be avoided completely. Figure 13 shows the reaction products in the new reactor relative to those in the previous reactor on an identical material during high-throughput screening as determined by the micro-GC. In the previous reactor, a considerable amount of air from the atmosphere was in the product during sampling allowing the CO production and methane consumption through oxidation reactions of methane (see green color in Figure 13). Therefore, avoiding oxygen from the atmosphere was essential to reduce undesired oxidation reactions. After the modification of the previous reactor, the amount of air during the reaction in the wells was close to zero (see blue color in Figure 13).

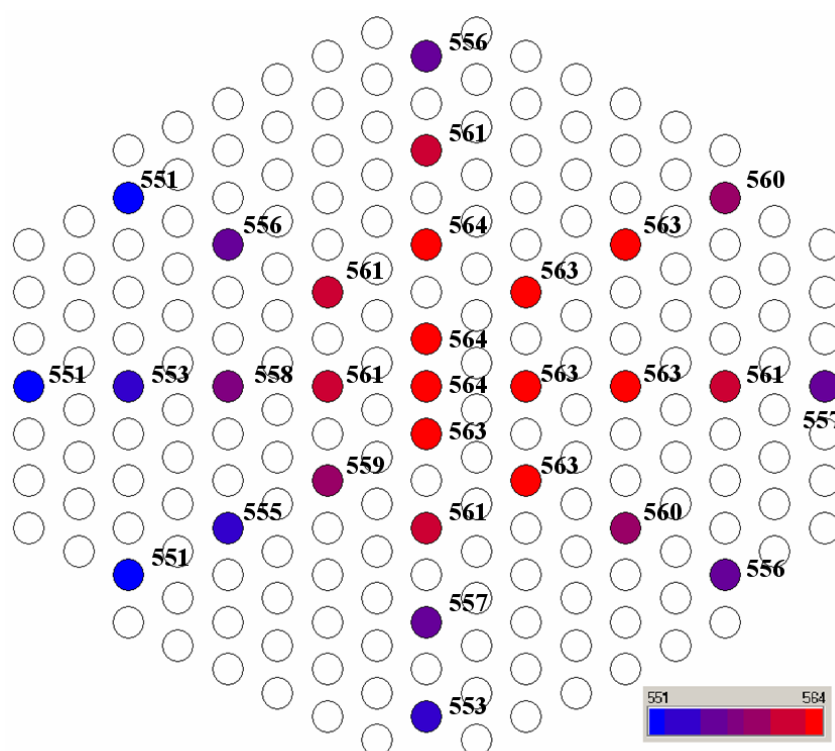


Figure 12. Measured temperature distribution across the catalyst library at 600°C

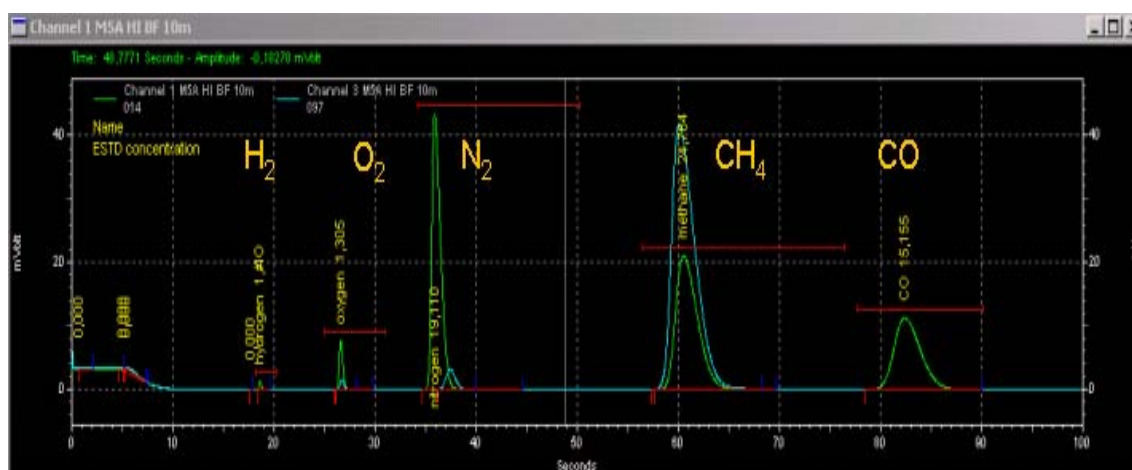


Figure 13. Reaction products on an identical material in previous reactor (green color) and new reactor (blue color) during high-throughput experiment, as determined by GC. Operating conditions: $T = 600\text{ }^{\circ}\text{C}$; $P = 1\text{ bar}$; total flow: 10 ml min^{-1} ($\text{CH}_4/\text{CO}_2 = 1.12$).

The additional improvement after modification probably arises from the direct contact of the insulating mask with the library plate preventing the cross-contamination of air from adjacent holes. The reactant gas, a certified calibration gas mixture composed of 52.8 vol% CH₄ and 47.2 vol% CO₂ (CH₄/CO₂ ratio: 1.12), was used without further purification. The flow rate of this gas mixture was always set to 10 ml min⁻¹. The gas composition of products was analyzed by Gas Chromatograph.

In a standard experiment, it took about 120 s (100 s inside the hole for reaction, 10 s outside the hole for waiting, and another 10 s for xyz-stage moving) to evaluate the catalytic activity for each material by a single GC run. Therefore, the activity test of 207 catalysts took approximately 7 h. The same high-throughput system was used for the stability test of the components. To assess the stability of each catalyst, the sampling needle was kept inside the hole of each well for 800 s with five GC runs or for 3500 s with 22 GC runs. The activity of each well is represented relative to the maximum activity of the reference catalyst. Although the stability test takes a long time, the experiment is completely automated and does not need much supervision. The rapid initial activity test can have false positives (i.e., rapidly deactivating materials) and false negatives (i.e., materials that activate slowly). Both negatives can be eliminated by the stability test. To enable comparisons of sample stability, the deactivation rate (h⁻¹) of each sample in the high-throughput experiment was defined as $[(1 - (\text{the activity at last measurement}) / (\text{the maximum activity})) / (\text{time-on-stream between a maximum and a last point (h)})]$. If the relative activity of a sample increased continuously during the measurement, then the deactivation rate was expressed as zero.

2.1.2. High-throughput experiments (generations 1 and 2)

The chemical composition of each catalyst in a library was verified by XRF. The concept of evolution (i.e., variation and selection) was applied for the library design. Variation

was obtained by doping and composition spread. Catalyst activity and stability, determined by the amount of CO produced and its deactivation rate, respectively, were chosen for selection. Hit samples, the most active catalysts of one generation, were used as base materials for the catalysts studied in the following generation. Table 1 summarizes the sample composition, preparation method, time on stream, sample number, and active sample of libraries sorted by generation.

Our search for new catalysts began with the systematic doping of $Zr_{20}Al_{80}$, which is known to exhibit extraordinarily high thermal stability [89]. An $E_xZr_{20}Al_{80-x}$ ($x = 1, 5, 10$ mol%) library with 177 samples of 59 different dopants (E) was tested. Among these, only precious metal including mixed oxides showed relatively good activity, which decreased in the following order: $Rh > Ru > Pt > Pd > Ir$ ($x = 1$), $Rh > Ru > Pd > Ir > Pt$ ($x = 5$), and $Rh > Pd \approx Pt > Ir > Ru$ ($x = 10$). This can be explained by the facile reducibility of noble metals and the exceptional catalytic properties of these metals in their metallic state [159]. Low loading (1 mol%) was sufficient for effective performance in the case of Rh and Ru. Figure 14 describes the activity (%) for the $E_xZr_{20}Al_{80-x}$ ($x = 1, 5, 10$ mol%) library, presented relative to the activity of $Rh_1Zr_{20}Al_{79}$, the best catalyst in this library. Despite controversy in the literature about the most suitable metal, Rh was always observed to be the most active and stable element in the CO_2 reforming of methane under our reaction conditions [19,82,160]. Precious metal-containing catalysts are effective and usually not dependent on prereduction steps.

Ni on alumina support with alkaline dopants such as K_2O , MgO , or CaO is commercially used in the steam reforming reaction. However, the nickel catalysts in the CO_2 reforming of methane are susceptible to a severe, inactive carbon deposition leading to reactor plugging despite of their high activity. Therefore, the improvement of the catalyst has attracted a lot of attention as mentioned in chapter 1.1. To see the catalytic properties of the nickel catalyst under our high-throughput experiment condition, 10 mol% Ni catalyst supported on commercial $\gamma-Al_2O_3$, referred to as Ni/Al_2O_3 , was prepared using by the wet impregnation method, filled in

Table 1. Sample composition, preparation method, time-on-stream, sample number, and active sample of libraries prepared^a

Generation	Sample composition	Method	Time-on-stream (s)	Sample Number	Active sample
1	$E_xZr_{20}Al_{80-x}$ ^b	1	100	59×3	(Rh, Ru, Pt, Pd, Ir) _x Zr ₂₀ Al _{80-x}
	M_3Ni_{97} ^c	1	100	55×6	None
	M_3P_{97} ^d	2	100	55×3	V_3Ni_{97}
	M_3Q_{97} ^e	3	100	55×5	Ni_3Ce_{97}
	Previous libraries ^f	-	100	≈ 4000	Rh, Ru, Pt, Pd and Ir containing catalysts
	V_3Ni_{97}, Ni_3Ce_{97}	2, 3	800	2	Ni_3Ce_{97}
2	M_3Ce_{97}	3	800	55	Ni_3Ce_{97}
	$Ni_{10}M_{90}$	3	800	55	$Ni_{10}Ce_{90}$
3	$M_{15}Ni_{10}Ce_{75}$	3	800	54	(Al _N , Al _A , Si, Ta, Zr _N , Zr _A) ₁₅ Ni ₁₀ Ce ₇₅ and (Cd, Rb, Sc, Se) ₁₅ Ni ₁₀ Ce ₇₅
		3	3500	10	(Al _N , Al _A , Si, Ta, Zr _N , Zr _A) ₁₅ Ni ₁₀ Ce ₇₅
4	$R_yNi_{10}Ce_{90-y}$ ^g	3	800	6×4	(Al _{N5} , Al _{N15} , Al _{A5} , Al _{A15} , Al _{A45} , Si ₅ , Si ₁₅ , Si ₄₅ , Si ₇₅ , Ta ₁₅ , Zr _{N5} , Zr _{N15} , Zr _{N75} , Zr _{A5} , Zr _{A15})Ni ₁₀ Ce _{90-y} and (Al _{A75} , Zr _{A45} , Zr _{A75})Ni ₁₀ Ce _{90-y}
		3	3500	18	(Al _{N5} , Al _{N15} , Al _{A15} , Zr _{N15} , Zr _{A5} , Zr _{A15})Ni ₁₀ Ce _{90-y}

^a Operating conditions: T = 600 °C; P = 1 bar; total flow: 10 ml min⁻¹ (CH₄/CO₂ = 1.12).

^b E = Ag, Al_N, Al_A, Au, B, Ba, Bi, Ca, Cd, Ce, Co, Cr, Cs, Cu, Dy, Er, Eu, Fe, Ga, Gd, Ge, Hf, Ho, In, Ir, K, La, Li, Lu, Mg, Mn, Mo, Na, Nb, Nd, Ni, Pb, Pd, Pr, Pt, Rb, Re, Rh, Ru, Sb, Sc, Se, Si, Sm, Sn, Sr, Ta, Tb, Te, Ti, Tm, V, W, Y, Yb, Zn, Zr_N, Zr_A. x = 1, 5, 10.

^c M = E - Au, Ir, Pd, Pt, Re, Rh, Ru. N = Cu, Fe, Nb, Sn, Ta, V.

^d P = Co, Mn, Ni.

^e Q = Ce, Cr, Ga, In, Zn.

^f See Table 2.

^g R = Al_N, Al_A, Si, Ta, Zr_N, Zr_A. y = 5, 15, 45, 75.

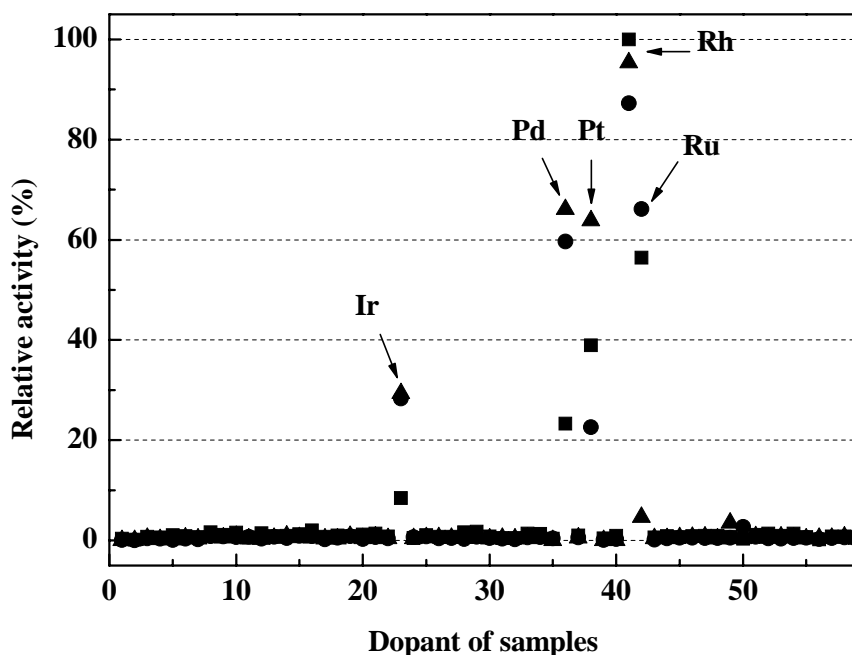


Figure 14. Relative activity (%) of the $E_xZr_{20}Al_{80-x}$ ($x = 1, 5, 10$) library, normalized to the activity of $Rh_1Zr_{20}Al_{79}$ (most active, reference): $x = (\blacksquare) 1, (\bullet) 5, (\blacktriangle) 10$ mol%. Operating conditions: $T = 600$ °C; $P = 1$ bar; total flow: 10 ml min^{-1} ($CH_4/CO_2 = 1.12$).

a well, and tested. The Ni/Al_2O_3 exhibited little CO formation in the initial activity test and even in the stability test over 3500 s. The catalytic activity of this catalyst appears to be highly dependent on the prereduction.

$Rh_1Zr_{20}Al_{79}$, the most active catalyst on the $E_xZr_{20}Al_{80-x}$ library was prepared several times by high-throughput synthesis and was used as a reference catalyst on all libraries during generations 1 and 2. Twenty additional libraries available in our research group with almost 4000 samples that had been prepared for other studies were assessed; here also, only precious metal-containing mixed oxides showed effective catalytic activity. Table 2 summarizes the catalysts on the libraries screened unsuccessfully for CO_2 reforming of methane during the primary screening phase of the project.

Table 2. Composition of mixed oxides on the selected prefabricated libraries studied during the primary screening^a

Binary and ternary mixed oxide	$(L_1)_x(L_2)_y$ (L = V, Fe, Mo, Cr, Ta, Nb, Mn, Sb, Bi) $(L_1)_x(L_2)_y(L_3)_z$ (L = V, Fe, Mo, Cr, Ta, Nb, Mn, Sb, Bi) $Nb_x Ta_y Ti_z$
Doped Sb oxides	$(L_1)_x(L_2)_y Sb_{90}$ (L = Bi, Mo, Nb, Te, Zr, Ta, V, Cr, Mn) $(L_1)_x(L_2)_y Sb_{90}$ (L = Fe, Sn, Cu, Ni, Ce, Ti, Al, Co, La)
Pt containing mixed oxides	$Pt_3(L_1)_x(L_2)_y$ (L = Ti, Ta, V, Al, Zr, Ni, Mn, W, Si, Co, Nb, Fe, Ge, Sn, Mo, Te, Bi) $Pt_3(L_1)_x(L_2)_y(L_3)_z$ (L = Zr, Al, Ni, Mn, Nb) $Pt_3(L_1)_x(L_2)_y(L_3)_z(L_4)_t$ (L = Ti, W, Nb, Ta)
Pd containing mixed oxides	$Pd_{0.5}(L_1)_x(L_2)_y$ (L = W, Cr, Nb, Mn, Fe, Ti, Al, Zr, Co, Zn, Ni, Cu, Sn, Ge, Si, Te) $Pd_{0.5}(L_1)_x(L_2)_y(L_3)_z$ (L = Si, Co, W, Fe, Cu, Cr, Ti)

^a Operating conditions: T = 600 °C; P = 1 bar; total flow: 10 ml min⁻¹ (CH₄/CO₂ = 1.12).

Because we focused on non-precious metal catalysts in this study, we prepared and examined 14 different non-precious metal (Ce, Co, Cr, Cu, Fe, Ga, In, Mn, Nb, Ni, Sn, Ta, V, and Zn)-based mixed oxides with 55 dopants of 3% (Ag, Al_N, Al_A, B, Ba, Bi, Ca, Cd, Ce, Co, Cr, Cs, Cu, Dy, Er, Eu, Fe, Ga, Gd, Ge, Hf, Ho, In, K, La, Li, Lu, Mg, Mn, Mo, Na, Nb, Nd, Ni, Pb, Pr, Rb, Sb, Sc, Se, Si, Sm, Sn, Sr, Ta, Tb, Te, Ti, Tm, V, W, Y, Yb, Zn, Zr_N, and Zr_A; subscript “N” for metal nitrate and “A” for metal alkoxide). The total number of catalysts prepared was 770. Only a few of these, such as Ni₃Ce₉₇ and V₃Ni₉₇, were effective, with activities of 32.5 and 52.5%, respectively, relative to the reference Rh₁Zr₂₀Al₇₉. Stability tests of these two catalysts were performed for 800 s. The relative activity of V₃Ni₉₇ decreased rapidly from 54.8 to 46.3% (maximum 71.0% at the second run) with a deactivation rate of 2.09 h⁻¹. In contrast, Ni₃Ce₉₇ showed good stability with a relative activity of 32.5-32.9% (maximum 33.9 % at the second run). The deactivation rate of Ni₃Ce₉₇ was 0.18 h⁻¹. Therefore, Ni₃Ce₉₇ was selected for the next generation. In the first generation, more than 5000 mixed oxides have been tested, and Ni₃Ce₉₇ exhibited the best activity and stability among all of the non-precious metal catalysts without prereduction.

In the second generation, the mixed oxides M_3Ce_{97} and $Ni_{10}M_{90}$ with total number of 110 were prepared with 55 different elements M and examined for 800 s to verify the activity of other ceria-based or nickel-including mixed oxides. However, only Ni_3Ce_{97} and $Ni_{10}Ce_{90}$ were significantly active, with relative activities of 32.5 and 93.9%, respectively. $Ni_{10}Ce_{90}$ revealed an effective stability, with relative activity of 93.9-95.1% (maximum 96.4% at the second run). The deactivation rate of $Ni_{10}Ce_{90}$ was 0.08 h^{-1} . Both nickel and ceria were selected as essential elements for the CO_2 reforming of methane with no prereduction step. $Ni_{10}Ce_{90}$ was selected as a hit sample for the subsequent generation due to higher activity and stability.

2.1.3. Conventional testing (after generations 1 and 2)

After the high-throughput testing of generations 1 and 2, the properties of the best materials needed to be confirmed in a conventional study. $Ni_{10}Ce_{90}$ and Ni/Al_2O_3 were synthesized by sol-gel preparation method 3 and a simple wet impregnation method, respectively, in a conventional manner. Table 3 shows that $Ni_{10}Ce_{90}$ has a low surface area and Ni/Al_2O_3 has a relatively high surface area, due to the inherent characteristic of each support. As shown in Figure 1, equilibrium conversions of CH_4 and CO_2 calculated were 53.1 and 69.4%, respectively, with a H_2/CO ratio of 0.85 at 600 °C. Only at 800 °C do the equilibrium conversions of CH_4 and CO_2 reach almost total conversion (87.8 and 99.1%, respectively) with a H_2/CO ratio of 1. The CO_2 conversion is always greater than that of CH_4 , due to the reverse water-gas shift (RWGS) reaction.

Conventional test results of both catalysts are shown in Figure 15. $Ni_{10}Ce_{90}$ demonstrated high initial activity (32.3 % of CH_4 conversion and 48.7 % of CO_2 conversion) with no prereduction. This catalyst revealed rapid deactivation during the first 30 min, and much less deactivation thereafter. In contrast, in Ni/Al_2O_3 activity did not start to increase until after almost 80 min, and catalytic activity stabilized only after about 240 min (long induction period).

Table 3. Physical property, TGA and results of conventional tests of selected catalysts

Generation	Catalyst	$S_{\text{BET}}^{\text{a}}$ ($\text{m}^2 \text{g}^{-1}$)	Conventional testing ^b		TGA ^c
			Max. relative activity (%)	Deactivation rate (h^{-1})	coke ($\text{g}_{\text{C}} \text{g}_{\text{cat}}^{-1}$) ($\text{wt}\% \text{h}^{-1}$)
1-2	$\text{Ni}_{10}\text{Ce}_{90}$	36.9	100.00	0.0181	0.08
	$\text{Ni}/\text{Al}_2\text{O}_3$	205.9	83.47	-	2.28
3-4	$\text{Al}_{\text{N}5}\text{Ni}_{10}\text{Ce}_{85}$	39.6	94.22	0.0138	0.03
	$\text{Al}_{\text{N}15}\text{Ni}_{10}\text{Ce}_{75}$	61.9	87.93	0.0109	0.19
	$\text{Al}_{\text{A}15}\text{Ni}_{10}\text{Ce}_{75}$	54.1	112.13	0.0093	0.38
	$\text{Zr}_{\text{N}15}\text{Ni}_{10}\text{Ce}_{75}$	39.2	106.29	0.0134	0.09
	$\text{Zr}_{\text{A}5}\text{Ni}_{10}\text{Ce}_{85}$	45.1	111.04	0.0125	0.24
	$\text{Zr}_{\text{A}15}\text{Ni}_{10}\text{Ce}_{75}$	47.4	106.97	0.0109	0.38

^a Measured after calcination in air at 700 °C for 2h, multipoint BET.

^b Operating conditions: T = 600 °C; P = 1 bar; total flow: 65 ml min^{-1} ($\text{CH}_4/\text{CO}_2/\text{Ar} = 16.9/15.1/68$); catalyst weight: 0.100 g; Time-on-stream: 10 h.

^c Operating conditions: catalyst weight: ≈ 0.050 g; T increasing rate: 15 °C min^{-1} ; air total flow: 15 ml min^{-1} .

After the activity of $\text{Ni}/\text{Al}_2\text{O}_3$ stabilized at 30.1 % of CH_4 conversion and 37.7 % of CO_2 conversion, the conversion of CO_2 slowly decreased while CH_4 consumption slowly increased, leading to reactor plugging by coking after 380 min. These results confirm that carbon formation is dominated by methane decomposition.

The gas hourly space velocities (GHSVs) of these catalysts are of interest. The GHSVs of $\text{Ni}_{10}\text{Ce}_{90}$ and $\text{Ni}/\text{Al}_2\text{O}_3$ were 139,000 (h^{-1}) and 36,000 (h^{-1}), respectively. Considering the surface area and GHSV of each catalyst, the active sites of $\text{Ni}_{10}\text{Ce}_{90}$ seem to be much more effective than that of $\text{Ni}/\text{Al}_2\text{O}_3$. The conversions of both catalysts do not reach thermodynamic equilibrium for two reasons: space velocity and deactivation. Testing 200 mg of $\text{Ni}_{10}\text{Ce}_{90}$ (GHSV 70,000 h^{-1}) and 400 mg of $\text{Ni}_{10}\text{Ce}_{90}$ (GHSV 35,000 h^{-1}) under identical conditions demonstrated that only the latter approached thermodynamic equilibrium with 49.3% CH_4 conversion and 62.7% CO_2 as shown in Figure 16.

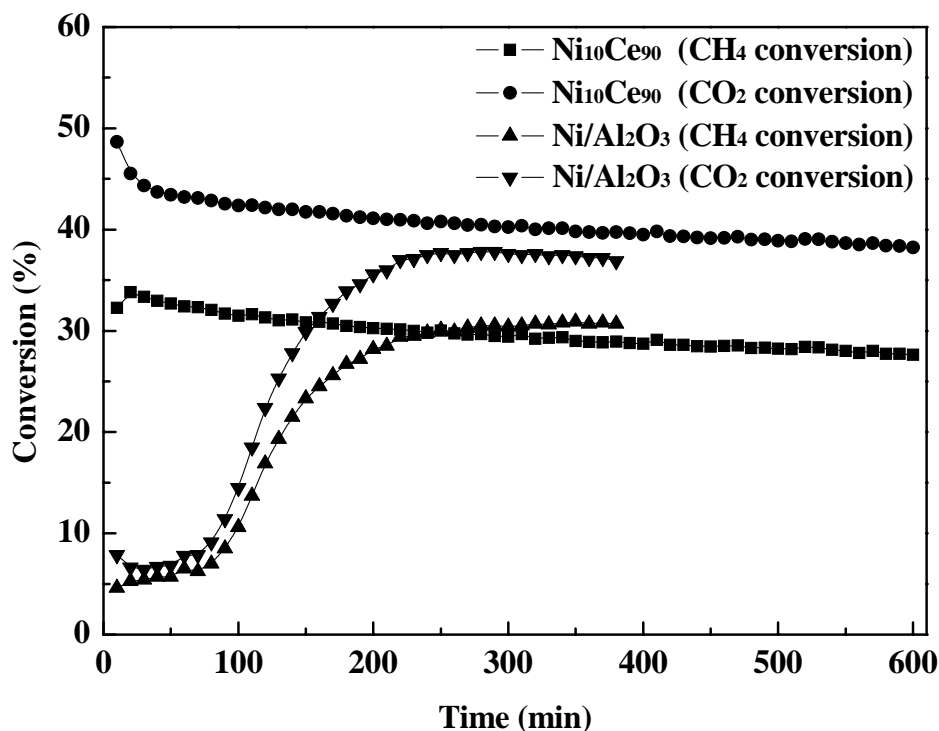


Figure 15. Time dependence of the catalytic activity and stability of Ni₁₀Ce₉₀ and Ni/Al₂O₃ in conventional test: CH₄ conversion (■) and CO₂ conversion (●) of Ni₁₀Ce₉₀; CH₄ conversion (▲) and CO₂ conversion (▼) of Ni/Al₂O₃. Operating conditions: T = 600 °C; P = 1 bar; total flow: 65 ml min⁻¹ (CH₄/CO₂/Ar = 16.9/15.1/68); catalyst weight: 0.100 g.

Similarly, it was reported that the conversions approaching those defined by thermodynamic equilibrium can be obtained over most of the nickel and noble metal based catalyst, as long as contact times are kept long enough [26]. For 100 mg of Ni₁₀Ce₉₀, the GHSV of 139,000 (h⁻¹) is too high to reach thermodynamic equilibrium. It also implies that our reaction conditions stay in the kinetic regime to avoid mass transfer limitation. Catalyst deactivation within the first 10 min also often contributes to this partial conversion. However, because reaching thermodynamic equilibrium would not reveal any differences in catalytic performance, these reaction conditions were chosen deliberately.

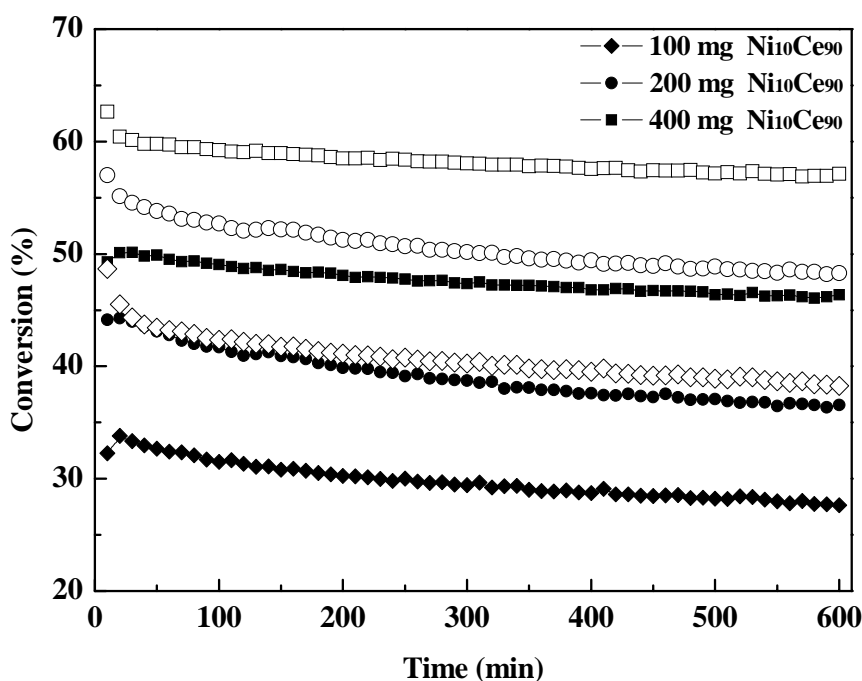


Figure 16. Time dependence of the catalytic activity depending on the amount of Ni₁₀Ce₉₀: CH₄ conversion (◆) and CO₂ conversion (◇) of 100 mg Ni₁₀Ce₉₀; CH₄ conversion (●) and CO₂ conversion (○) of 200 mg Ni₁₀Ce₉₀; CH₄ conversion (■) and CO₂ conversion (□) of 400 mg Ni₁₀Ce₉₀. Operating conditions: T = 600 °C; P = 1 bar; total flow: 65 ml min⁻¹ (CH₄/CO₂/Ar = 16.9/15.1/68).

The results of the conventional study within 60 min of reaction time are in accordance with those of the high-throughput screening for 3500 s. Initial high activity followed by rapid deactivation of Ni₁₀Ce₉₀ and low activity of Ni/Al₂O₃ were observed in both experiments. The good agreement between the combinatorial results and the results obtained under conventional reaction conditions confirms that the development of catalysts for the CO₂ reforming of methane can be carried out reliably using a simple high-throughput method.

Carbon (coke) deposition is thermodynamically favoured at our experimental conditions of low temperature (600 °C) and a high CH₄/CO₂ ratio of 1.12. It has been reported

that at low CH_4/CO_2 ratios (< 1) and high-temperature (> 1000 °C), carbon formation is significantly reduced [15,19,21-23]. The weight change during TPO of $\text{Ni}_{10}\text{Ce}_{90}$ used for 600 min and $\text{Ni}/\text{Al}_2\text{O}_3$ for 380 min was measured by TGA. The weights of sample were normalized with respect to the initial sample weight and then differentiated with respect to temperature for d-TGA pattern. The d-TGA profiles are shown in Figure 17.

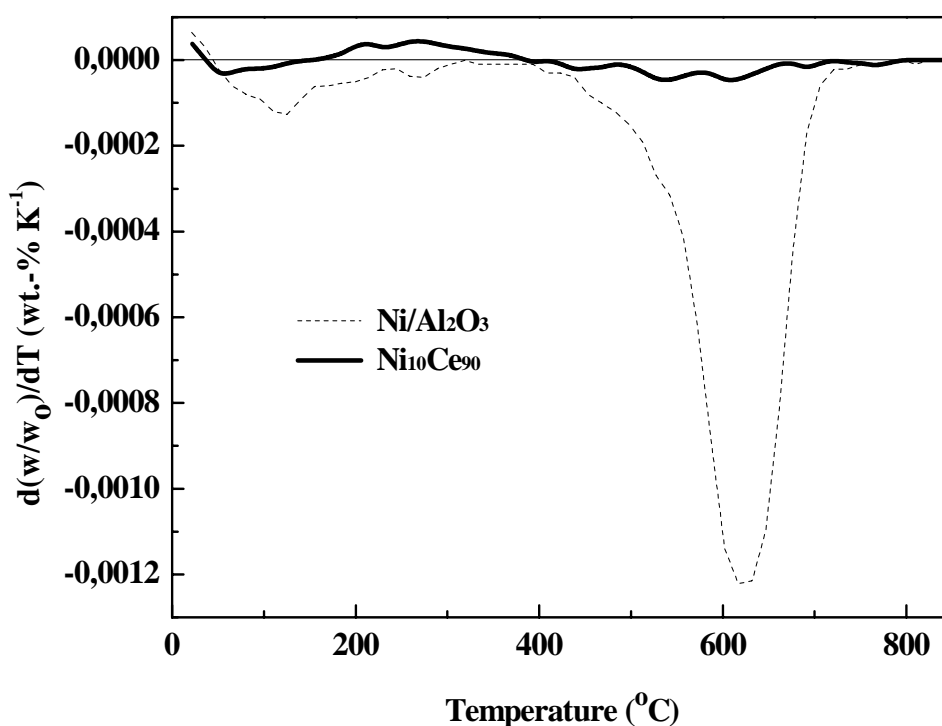


Figure 17. d-TGA profile of used $\text{Ni}_{10}\text{Ce}_{90}$ (—) (after 600 min reaction time) and used $\text{Ni}/\text{Al}_2\text{O}_3$ (-----) (after 380 min reaction time). Operating conditions: catalyst weight: ≈ 0.050 g; T increasing rate: 15 °C min^{-1} ; air total flow: 15 ml min^{-1} .

Two main peaks appeared for the used $\text{Ni}/\text{Al}_2\text{O}_3$. The first peak, observed between 50 and 320 °C with a weight loss of 0.22 $\text{wt}\%$ (h^{-1}), can be assigned to water desorbing from the catalyst surface. The second weight loss occurred in the temperature range of 400 - 800 °C with a weight change of 2.28 $\text{wt}\%$ (h^{-1}), and can be assigned to oxidation of deposited carbon.

The d-TGA pattern of the used $\text{Ni}_{10}\text{Ce}_{90}$ showed three different peaks. The first peak, at 40-155 °C with a weight loss of 0.01 wt% (h^{-1}), can be assigned to desorption of water. The third peak, at 400–800 °C with a weight loss of 0.08 wt% (h^{-1}), can be assigned to the oxidation of carbon deposition as in the case of $\text{Ni}/\text{Al}_2\text{O}_3$. The second peak, representing a weight gain rather than a weight loss, appeared at 160-385 °C with a weight change of 0.06 wt% (h^{-1}). This surprising behaviour is attributed to the reoxidation of some oxygen vacancies generated during the reaction. However, determining the amount of chemisorbed oxygen was difficult, because the first and second peaks overlapped. As shown in Figure 18, the weight gain peak was also observed in d-TGA results on fresh $\text{Ni}_{10}\text{Ce}_{90}$ reduced by hydrogen, but it was not detected in d-TGA results on fresh $\text{Ni}_{10}\text{Ce}_{90}$ calcined in ambient air. A study of three-way catalysts found a similar weight recovery when pulses of hydrogen were followed by pulses of oxygen on cerium oxide [161].

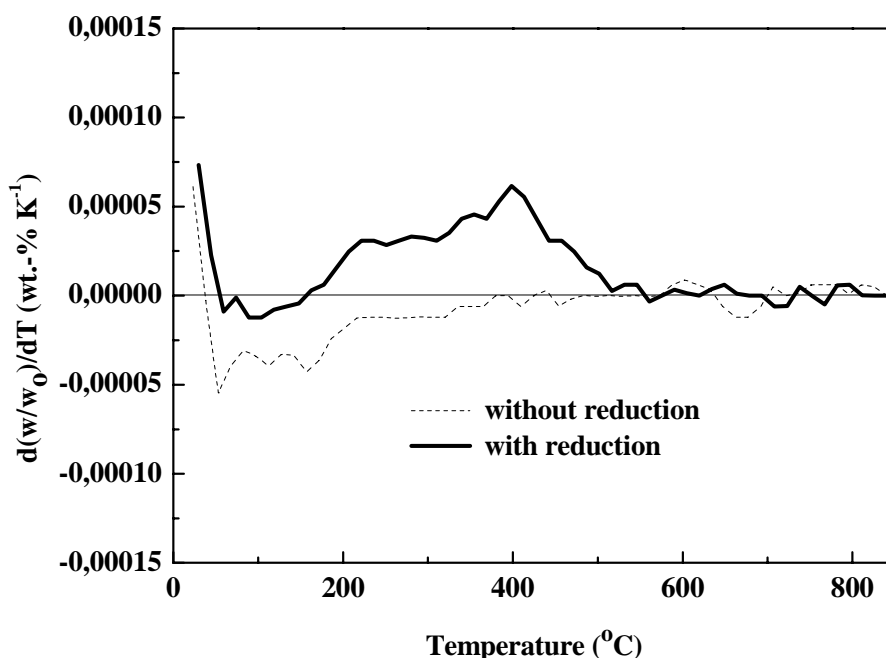


Figure 18. d-TGA profile of fresh $\text{Ni}_{10}\text{Ce}_{90}$ without reduction step (-----) and with reduction step (—). Operating conditions: catalyst weight: ≈ 0.050 g; T increasing rate: $15^{\circ}\text{C min}^{-1}$; air total flow: 15 ml min^{-1} .

2.1.4. High-throughput experiments (generations 3 and 4)

A major drawback of the $\text{Ni}_{10}\text{Ce}_{90}$ is deactivation. To reduce deactivation of $\text{Ni}_{10}\text{Ce}_{90}$, a third oxide of 15 mol% (54 different elements) was introduced using the sol-gel process. An $\text{M}_{15}\text{Ni}_{10}\text{Ce}_{75}$ library was prepared and tested (generation 3). $\text{Ni}_{10}\text{Ce}_{90}$ was used as reference catalyst during generations 3 and 4. Among the 54 samples of the $\text{M}_{15}\text{Ni}_{10}\text{Ce}_{75}$ library, only a few catalysts, including $(\text{Al}_N, \text{Al}_A, \text{Si}, \text{Ta}, \text{Zr}_N, \text{Zr}_A)_{15}\text{Ni}_{10}\text{Ce}_{75}$, showed comparable activity and better stability for 800 s relative to $\text{Ni}_{10}\text{Ce}_{90}$. To reduce false negatives due to slowly activated candidates, which could originate from relatively short time on stream, $(\text{Cd}, \text{Rb}, \text{Sc}, \text{Se})_{15}\text{Ni}_{10}\text{Ce}_{75}$ were also chosen, due to their low but increasing activity with time (see Figure 19). Figure 19a depicts the relative activities (%) of $\text{Ni}_{10}\text{Ce}_{90}$ and 10 candidates after 800 s of reaction time. The deactivation rate was 0.08 h^{-1} for $\text{Ni}_{10}\text{Ce}_{90}$ and 0 for the 10 candidates. These ten samples and $\text{Ni}_{10}\text{Ce}_{90}$ were checked again for 3500 s. The relative activities (%) of $\text{Ni}_{10}\text{Ce}_{90}$ and the 10 candidates for 3500 s are shown in Figure 19b. $(\text{Cd}, \text{Rb}, \text{Sc}, \text{Se})_{15}\text{Ni}_{10}\text{Ce}_{75}$ revealed only poor activity during the measurement. Therefore, these four catalysts were excluded in the next generation of catalysts. Comparable activity and a reduced deactivation rate were observed for $(\text{Al}_N, \text{Al}_A, \text{Si}, \text{Ta}, \text{Zr}_N, \text{Zr}_A)_{15}\text{Ni}_{10}\text{Ce}_{75}$ relative to $\text{Ni}_{10}\text{Ce}_{90}$. Deactivation rates of 0.08 h^{-1} for $\text{Ni}_{10}\text{Ce}_{90}$ and 0, 0.03, 0.04, 0.06, 0.04, and 0.04 h^{-1} for $(\text{Al}_N, \text{Al}_A, \text{Si}, \text{Ta}, \text{Zr}_N, \text{Zr}_A)_{15}\text{Ni}_{10}\text{Ce}_{75}$ were observed. These catalysts are the hits of generation 3, selected for further improvements.

In generation 4, the amount of third element was varied stepwise in 5, 15, 45, and 75 mol% for selected catalysts of generation 3. Figure 20a describes the relative activities (%) of $\text{Ni}_{10}\text{Ce}_{90}$ and $(\text{Al}_N, \text{Al}_A, \text{Si}, \text{Ta}, \text{Zr}_N, \text{Zr}_A)_y\text{Ni}_{10}\text{Ce}_{90-y}$ ($y = 5, 15, 45, 75$) mixed oxides after 800 s of reaction time. Some of these, including $(\text{Al}_{N5}, \text{Al}_{N15}, \text{Al}_{A5}, \text{Al}_{A15}, \text{Al}_{A45}, \text{Si}_5, \text{Si}_{15}, \text{Si}_{45}, \text{Si}_{75}, \text{Ta}_{15}, \text{Zr}_{N5}, \text{Zr}_{N15}, \text{Zr}_{N75}, \text{Zr}_{A5}, \text{Zr}_{A15})\text{Ni}_{10}\text{Ce}_{90-y}$, exhibited similar activities and lower deactivation rates compared with $\text{Ni}_{10}\text{Ce}_{90}$.

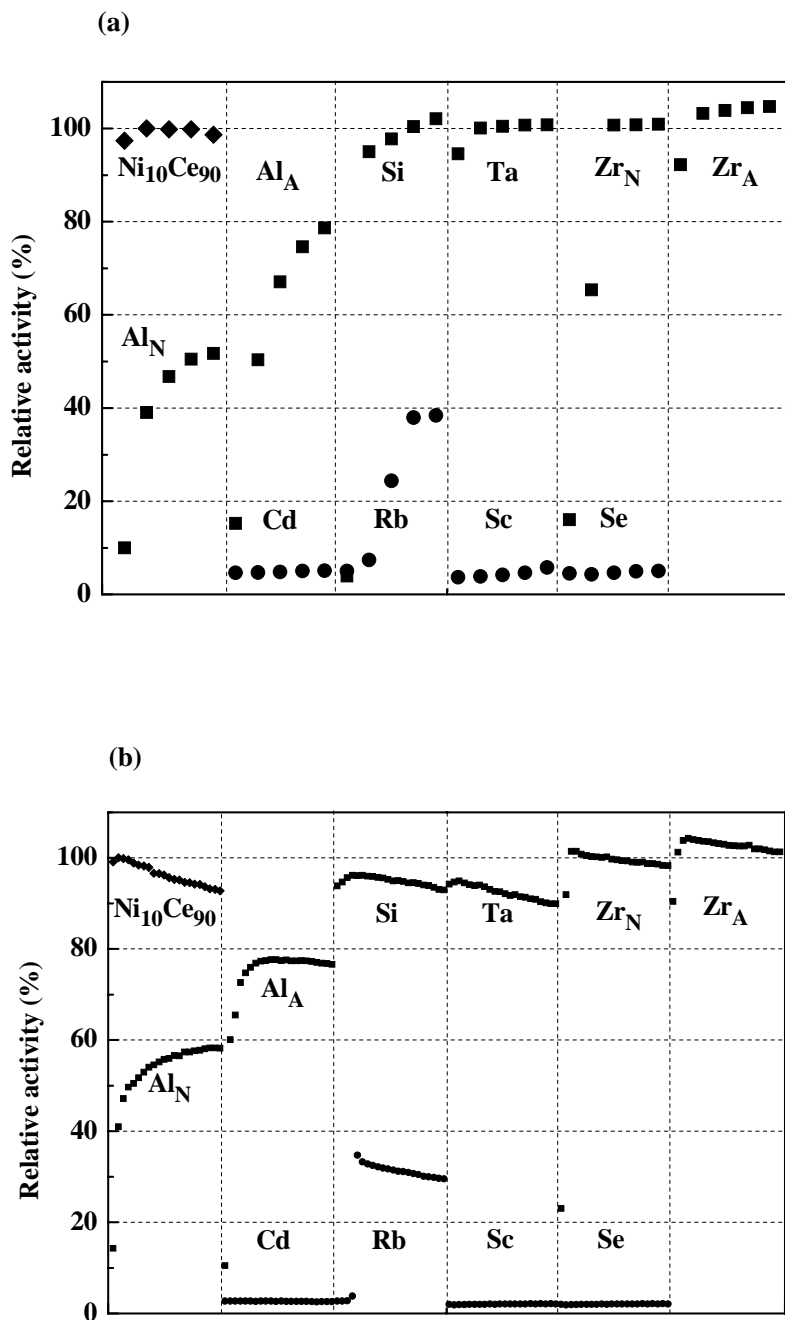


Figure 19. Time dependence of the catalytic activity (%) of selected materials on the $\text{M}_{15}\text{Ni}_{10}\text{Ce}_{75}$ library relative to the reference catalyst $\text{Ni}_{10}\text{Ce}_{90}$ in high-throughput tests during (a) 800 and (b) 3500 s: (◆) $\text{Ni}_{10}\text{Ce}_{90}$; (■) $(\text{Al}_\text{N}, \text{Al}_\text{A}, \text{Si}, \text{Ta}, \text{Zr}_\text{N}, \text{Zr}_\text{A})_{15}\text{Ni}_{10}\text{Ce}_{75}$; (●) $(\text{Cd}, \text{Rb}, \text{Sc}, \text{Se})_{15}\text{Ni}_{10}\text{Ce}_{75}$. Operating conditions: $T = 600\text{ }^\circ\text{C}$; $P = 1\text{ bar}$; total flow: 10 ml min^{-1} ($\text{CH}_4/\text{CO}_2 = 1.12$).

A zero deactivation rate was found for all of these materials except $\text{Ni}_{10}\text{Ce}_{90}$ (0.08 h^{-1}), $\text{Al}_{A45}\text{Ni}_{10}\text{Ce}_{45}$ (0.01 h^{-1}), and $\text{Si}_5\text{Ni}_{10}\text{Ce}_{85}$ (0.01 h^{-1}). $(\text{Al}_{A75}, \text{Zr}_{A45}, \text{Zr}_{A75})\text{Ni}_{10}\text{Ce}_{90-y}$ were also selected because of their zero deactivation rates despite low relative activities. The selected samples and $\text{Ni}_{10}\text{Ce}_{90}$ were retested for another 3500 s. Among these samples, $(\text{Al}_{N5}, \text{Al}_{N15}, \text{Al}_{A15}, \text{Zr}_{N15}, \text{Zr}_{A5}, \text{Zr}_{A15})\text{Ni}_{10}\text{Ce}_{90-y}$ had activities comparable to the activity of $\text{Ni}_{10}\text{Ce}_{90}$ and a deactivation rate of $<0.04 \text{ h}^{-1}$, as shown in Figure 20b. The deactivation rates of these catalysts were 0.08 h^{-1} for $\text{Ni}_{10}\text{Ce}_{90}$ and 0.04, 0, 0.03, 0.03, 0.04, and 0.03 h^{-1} for $(\text{Al}_{N5}, \text{Al}_{N15}, \text{Al}_{A15}, \text{Zr}_{N15}, \text{Zr}_{A5}, \text{Zr}_{A15})\text{Ni}_{10}\text{Ce}_{90-y}$, respectively, which were selected as hit catalysts from generation 4. The high-throughput optimization was terminated at this stage.

2.1.5. Conventional testing (after generations 3 and 4)

The best catalysts from generation 4 were synthesized and examined by conventional experiments. Figure 21 and 23 gives an overview of the conventional test results of $\text{Al}_{A15}\text{Ni}_{10}\text{Ce}_{75}$, $\text{Zr}_{N15}\text{Ni}_{10}\text{Ce}_{75}$ and $\text{Al}_{N15}\text{Ni}_{10}\text{Ce}_{75}$, $\text{Al}_{N15}\text{Ni}_{10}\text{Ce}_{75}$, $\text{Zr}_{A5}\text{Ni}_{10}\text{Ce}_{85}$, $\text{Zr}_{A15}\text{Ni}_{10}\text{Ce}_{75}$ in comparison with $\text{Ni}_{10}\text{Ce}_{90}$, respectively. The d-TGA profile of used $(\text{Al}_{N5}, \text{Al}_{N15}, \text{Al}_{A15}, \text{Zr}_{N15}, \text{Zr}_{A5}, \text{Zr}_{A15})\text{Ni}_{10}\text{Ce}_{90-y}$ in comparison with used reference $\text{Ni}_{10}\text{Ce}_{90}$ after 600 min of reaction time are shown in Figure 22.

Table 3 summarizes the physical properties and results of conventional testing and TGA of these selected catalysts (see page 40). The maximum relative activity (%) was defined as $[(\text{the maximum amount of CO produced on a catalyst})/(\text{the maximum amount of CO produced on } \text{Ni}_{10}\text{Ce}_{90}) \times 100]$ during 10 h of reaction. The maximum activity was observed at the first measurement after 10 min in all catalysts but $\text{Al}_{N5}\text{Ni}_{10}\text{Ce}_{85}$ (30 min) and $\text{Al}_{N15}\text{Ni}_{10}\text{Ce}_{75}$ (210 min). The surface areas of all catalysts were slightly increased relative to that of $\text{Ni}_{10}\text{Ce}_{90}$, especially those of $\text{Al}_{N15}\text{Ni}_{10}\text{Ce}_{75}$ and $\text{Al}_{A15}\text{Ni}_{10}\text{Ce}_{75}$.

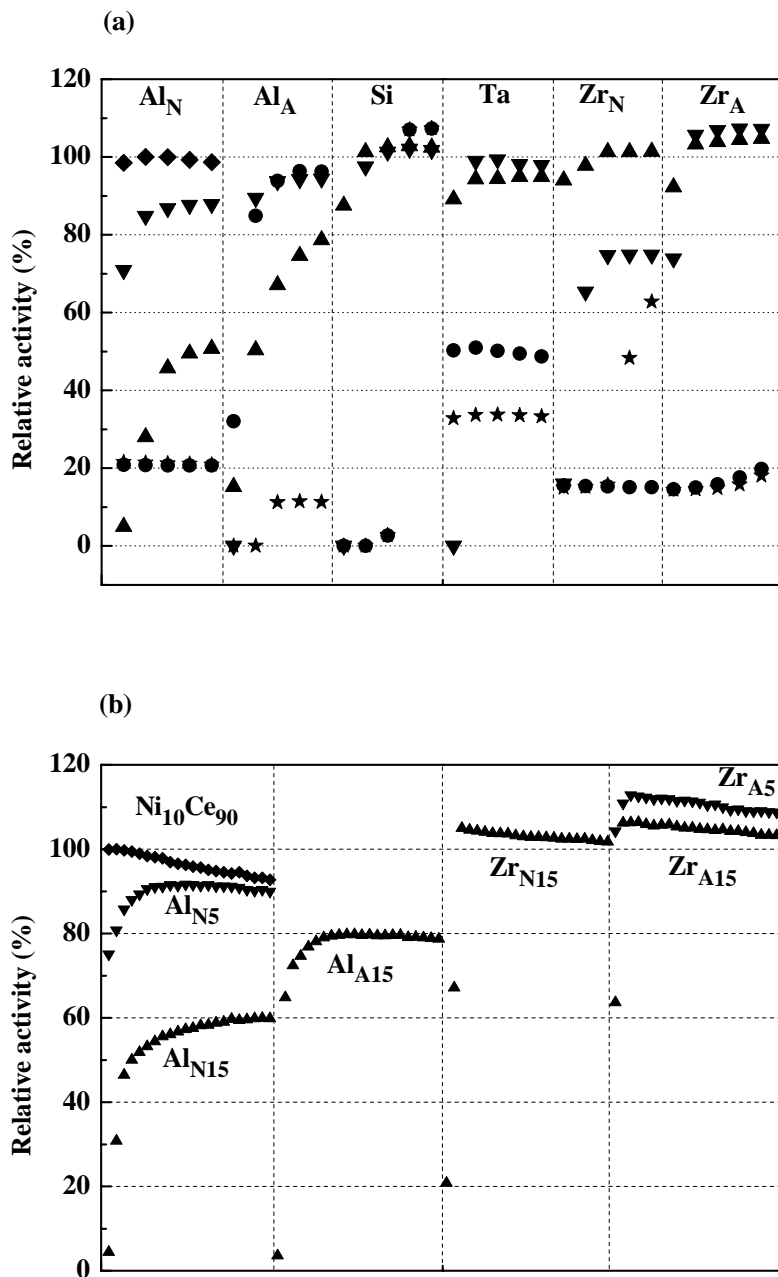


Figure 20. Time dependence of the catalytic activity (%) of selected materials on the (Al_N , Al_A , Si, Ta, Zr_N , Zr_A) $_yNi_{10}Ce_{90-y}$ ($y = 5, 15, 45, 75$) library relative to the reference catalyst $Ni_{10}Ce_{90}$ in high-throughput tests during (a) 800 and (b) 3500 s: (\blacklozenge) $Ni_{10}Ce_{90}$; $y = (\blacktriangledown)$ 5; (\blacktriangle) 15; (\bullet) 45; (\blackstar) 75 mol%. Operating conditions: $T = 600$ °C; $P = 1$ bar; total flow: 10 ml min^{-1} ($CH_4/CO_2 = 1.12$).

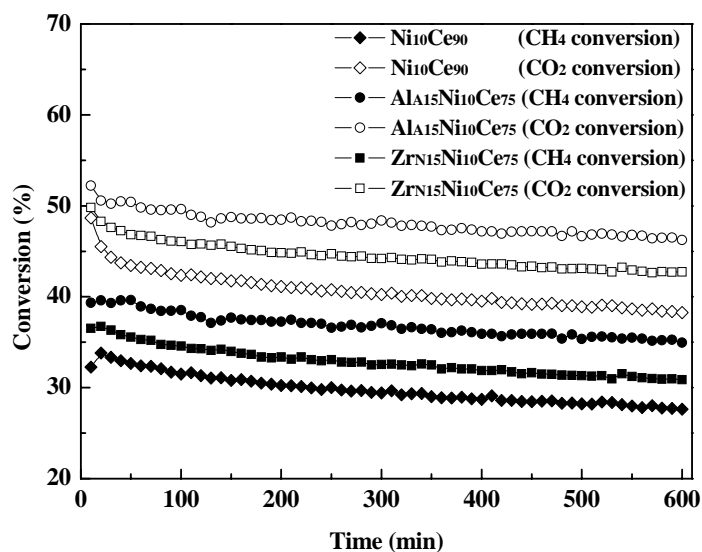


Figure 21. Time dependence of the catalytic activity of Al₁₅Ni₁₀Ce₇₅ and Zr₁₅Ni₁₀Ce₇₅ in comparison with Ni₁₀Ce₉₀ in conventional tests: CH₄ (◆) and CO₂ (◇) conversion of Ni₁₀Ce₉₀; CH₄ (●) and CO₂ (○) conversion of Al₁₅Ni₁₀Ce₇₅; CH₄ (■) and CO₂ (□) conversion of Zr₁₅Ni₁₀Ce₇₅. Operating conditions: T = 600 °C; P = 1 bar; total flow: 65 ml min⁻¹ (CH₄/CO₂/Ar = 16.9/15.1/68); catalyst weight: 0.100 g.

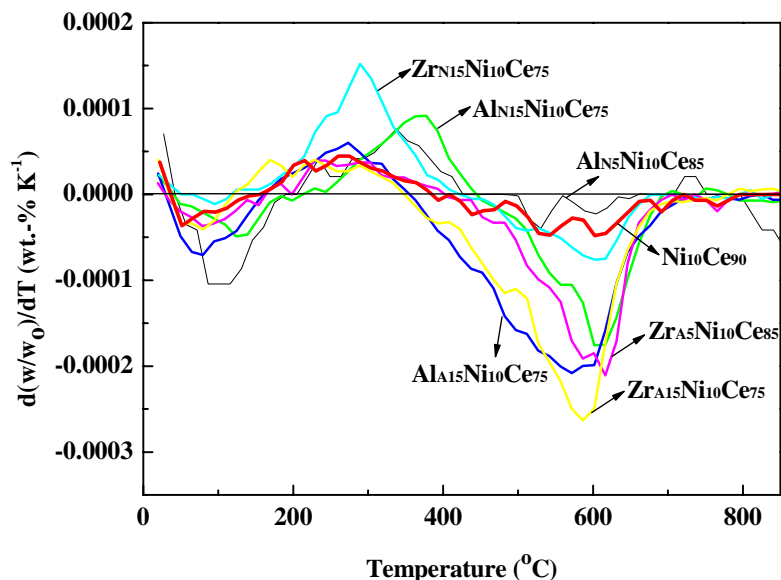


Figure 22. d-TGA profile of used (Al_{N5}, Al_{N15}, Al_{A15}, Zr_{N15}, Zr_{A5}, Zr_{A15})Ni₁₀Ce_{90-y} in comparison with the reference Ni₁₀Ce₉₀ after 600 min reaction time. Operating conditions: catalyst weight: ≈ 0.050 g; T increasing rate: 15 °C min⁻¹; air total flow: 15 ml min⁻¹.

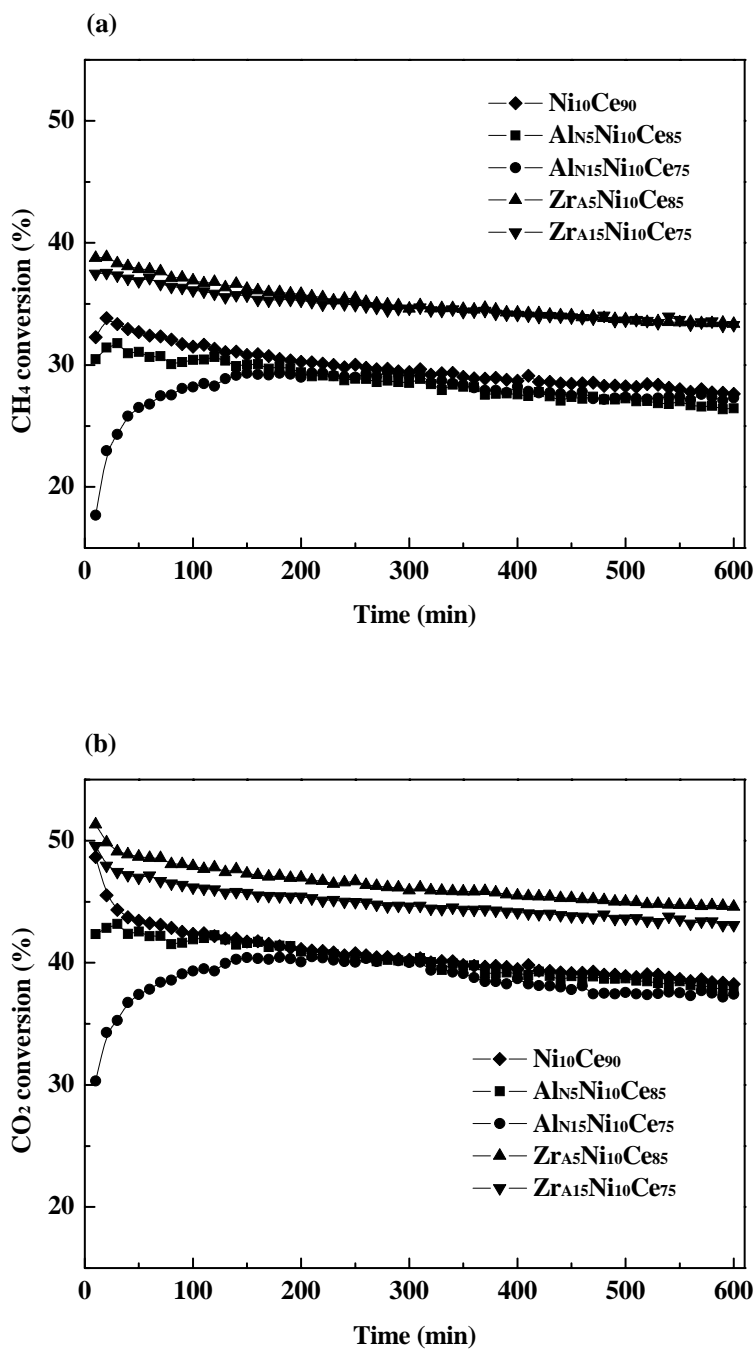


Figure 23. Time dependence of (a) CH₄ conversion and (b) CO₂ conversion of (■) Al_{N5}Ni₁₀Ce₈₅, (●) Al_{N15}Ni₁₀Ce₇₅, (▲) Zr_{A5}Ni₁₀Ce₈₅, and (▼) Zr_{A15}Ni₁₀Ce₇₅ in comparison with (◆) Ni₁₀Ce₉₀ in conventional tests. Operating conditions: T = 600 °C; P = 1 bar; total flow: 65 ml min⁻¹ (CH₄/CO₂/Ar = 16.9/15.1/68); catalyst weight: 0.100 g.

Figure 24 compares high-throughput testing for 3500 s and conventional testing within the first 60 min. The relative activities after the same time on stream were very similar for ($\text{Al}_{\text{N}5}$, $\text{Zr}_{\text{N}15}$, $\text{Zr}_{\text{A}5}$, $\text{Zr}_{\text{A}15}$) $\text{Ni}_{10}\text{Ce}_{90-y}$ but increased for $\text{Al}_{\text{N}15}\text{Ni}_{10}\text{Ce}_{75}$ and $\text{Al}_{\text{A}15}\text{Ni}_{10}\text{Ce}_{75}$. This finding is attributed to the different catalyst loading methods in high-throughput testing and conventional testing. In the high-throughput experiment, the same volume of catalyst powder is filled in library wells, and the same weight is charged in the conventional gas-phase reactor. On BET measurements, $\text{Al}_{\text{N}15}\text{Ni}_{10}\text{Ce}_{75}$ and $\text{Al}_{\text{A}15}\text{Ni}_{10}\text{Ce}_{75}$ showed much larger surface areas than $\text{Ni}_{10}\text{Ce}_{90}$, which may be the reason for the increased activity in the conventional tests.

The ternary component of the catalysts affected the catalytic properties in the following order: (1) maximum activity: $\text{Al}_{\text{A}15} \approx \text{Zr}_{\text{A}5} > \text{Zr}_{\text{A}15} \approx \text{Zr}_{\text{N}15} > \text{None} > \text{Al}_{\text{N}5} > \text{Al}_{\text{N}15}$; (2) deactivation rate: $\text{None} > \text{Al}_{\text{N}5} > \text{Zr}_{\text{N}15} > \text{Zr}_{\text{A}5} > \text{Al}_{\text{N}15} \approx \text{Zr}_{\text{A}15} > \text{Al}_{\text{A}15}$; (3) carbon deposition: $\text{Al}_{\text{A}15} \approx \text{Zr}_{\text{A}15} > \text{Zr}_{\text{A}5} > \text{Al}_{\text{N}15} > \text{Zr}_{\text{N}15} \approx \text{None} \approx \text{Al}_{\text{N}5}$. It has been shown that third elements affect the behaviour of catalysts of lower activity ($\text{Al}_{\text{N}5}$, $\text{Al}_{\text{N}15}$) and higher activity ($\text{Al}_{\text{A}15}$, $\text{Zr}_{\text{A}5}$, $\text{Zr}_{\text{A}15}$ and $\text{Zr}_{\text{N}15}$) and increase their stability in comparison with $\text{Ni}_{10}\text{Ce}_{90}$. Carbon deposition increased slightly in all samples but $\text{Al}_{\text{N}5}\text{Ni}_{10}\text{Ce}_{85}$ and $\text{Zr}_{\text{N}15}\text{Ni}_{10}\text{Ce}_{75}$. $\text{Al}_{\text{A}15}\text{Ni}_{10}\text{Ce}_{75}$ seems to be a good new catalyst with respect to its activity and stability despite its tendency towards carbon deposition, and $\text{Zr}_{\text{N}15}\text{Ni}_{10}\text{Ce}_{75}$ is most attractive because of its high activity and low tendency towards coking despite its deactivation behaviour.

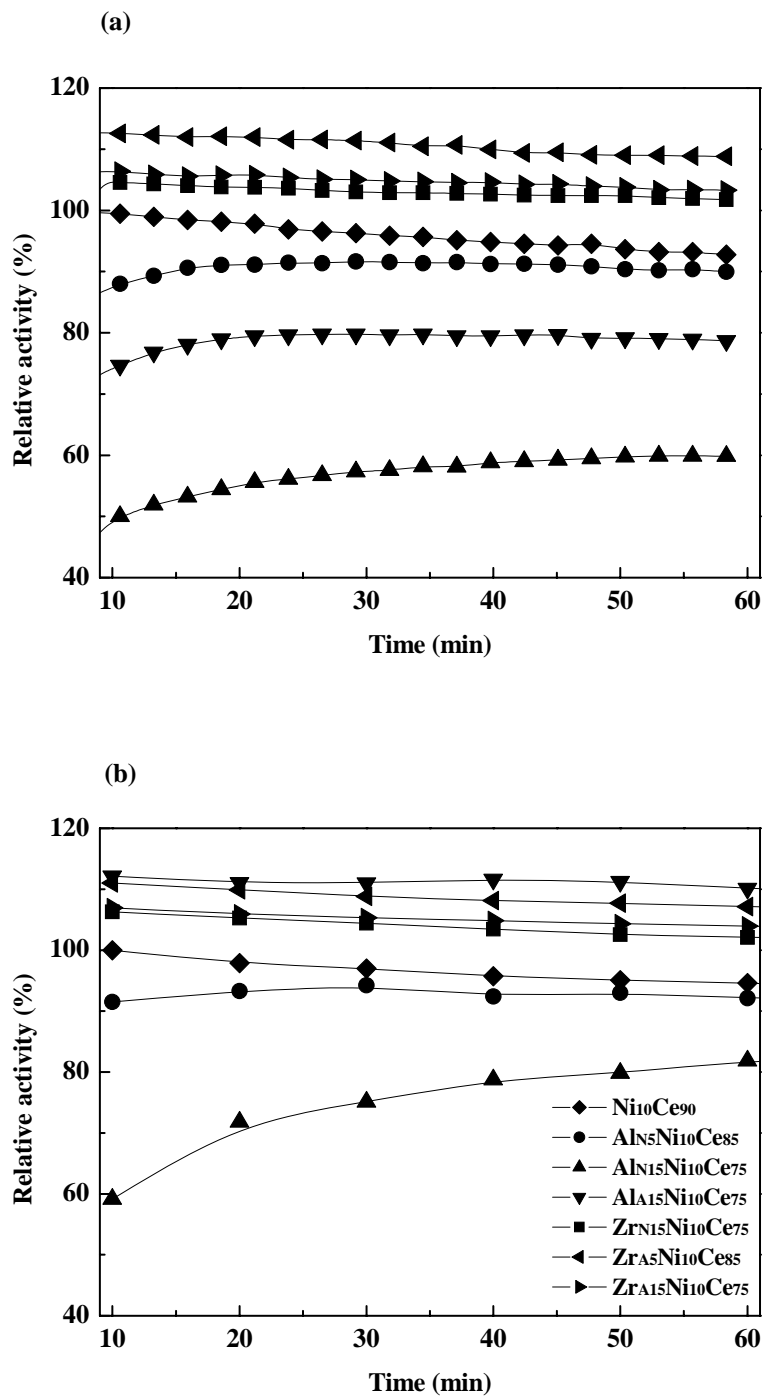


Figure 24. Time dependence of the catalytic activity (%) of the best catalysts relative to the reference $\text{Ni}_{10}\text{Ce}_{90}$ in (a) high-throughput testing during 3500 s and (b) conventional tests within the first 3600 s: (◆) $\text{Ni}_{10}\text{Ce}_{90}$; (●) $\text{Al}_{\text{N}5}\text{Ni}_{10}\text{Ce}_{85}$; (▲) $\text{Al}_{\text{N}15}\text{Ni}_{10}\text{Ce}_{75}$; (▼) $\text{Al}_{\text{A}15}\text{Ni}_{10}\text{Ce}_{75}$; (■) $\text{Zr}_{\text{N}15}\text{Ni}_{10}\text{Ce}_{75}$; (◄) $\text{Zr}_{\text{A}5}\text{Ni}_{10}\text{Ce}_{85}$; (►) $\text{Zr}_{\text{A}15}\text{Ni}_{10}\text{Ce}_{75}$.

2.2. Mechanistic study of Ni-Ce mixed oxide

In chapter 2.1, high-throughput synthesis and screening techniques were used in the search for and optimization of new autoactivation catalysts for the CO₂ reforming of methane and the results from HTE were confirmed in conventional studies. Best catalysts discovered were Ni-based mixed oxide and among them a new Ni₁₀Ce₉₀ mixed oxide catalyst was identified, which exhibits several unusual features: (1) a lack of coking; (2) immediate activity (no need for prereduction), and (3) high catalytic activity. Although a slow but continuous catalyst deactivation was recognized for Ni₁₀Ce₉₀, it could be strongly reduced by doping with 15 mol% Al or Zr.

In order to learn more about the structural features connected to catalytic activity and stability of this Ni-Ce mixed oxide, the Ni₁₀Ce₉₀ mixed oxide is investigated by X-ray diffraction (XRD) and pulse experimentation.

2.2.1. Catalyst performance and carbon deposition

The Ni_xCe_{100-x} (x = 0, 10, 100) mixed oxides were prepared by the procedure similar to those described in sol-gel preparation method 3 (see chapter 3.1) in a conventional manner. For comparison, the 10 mol% Ni catalyst supported on commercial γ -Al₂O₃, referred to as Ni/Al₂O₃, was prepared by wet impregnation. By BET measurements of each material after calcination at 700 °C, the surface areas of fresh ceria (19.7 m² g⁻¹), nickel oxide (29.4 m² g⁻¹) and Ni₁₀Ce₉₀ mixed oxide (36.9 m² g⁻¹) have a low surface area, and γ -Al₂O₃ (255.0 m² g⁻¹) and Ni/Al₂O₃ (205.9 m² g⁻¹) have a relatively high surface area.

Catalytic activity tests of Ni₁₀Ce₉₀ and Ni/Al₂O₃ were performed for the CO₂ reforming

of methane after *in situ* oxidation or reduction at the reaction temperature (600 °C). The GHSVs of Ni₁₀Ce₉₀ and Ni/Al₂O₃ were 139,000 (h⁻¹) and 36,000 (h⁻¹), respectively. Table 4 summarizes the catalytic performance and tendency to coking on Ni/Al₂O₃ and Ni₁₀Ce₉₀ contingent on the different pretreatments.

Table 4. Catalytic activity and coking rate on Ni₁₀Ce₉₀ and Ni/Al₂O₃ depending on the different treatment

Catalyst	Treatment ^a	Conversion (%) ^b				TGA ^c coke (g _C g _{cat} ⁻¹) (wt% h ⁻¹)
		10 min		600 min		
		CH ₄	CO ₂	CH ₄	CO ₂	
Ni/Al ₂ O ₃	oxidation	4.6	7.9	30.7 ^d	36.9 ^d	2.28
	reduction	38.8	48.5	38.0	45.4	1.00
Ni ₁₀ Ce ₉₀	oxidation	32.3	48.7	27.6	38.3	0.08
	reduction	6.2	15.2	4.9	6.6	0.01

^a Treated *in situ* at 600 °C for 2 h in flowing air or hydrogen (50 ml min⁻¹).

^b Operating conditions: $T = 600$ °C; $P = 1$ bar; total flow: 65 ml min⁻¹ (CH₄/CO₂/Ar = 16.9/15.1/68); catalyst weight: 0.100 g; Time-on-stream: 10 h.

^c Operating conditions: catalyst weight: ≈ 0.050 g; T increasing rate: 15 °C min⁻¹; air total flow: 15 ml min⁻¹.

^d Measured after 380 min due to reactor clogging.

The oxidized Ni/Al₂O₃ showed a low initial activity which did not start to increase until after almost 80 min, and catalytic activity stabilized only after about 240 min (long induction period). Moreover, Ni/Al₂O₃ led to reactor plugging after only 380 min due to strong carbon deposition (2.28 wt% h⁻¹). The prereduced Ni/Al₂O₃ revealed an immediate activity and relatively high rate of coke formation (1.00 wt% h⁻¹) although reactor plugging was not detected. For the Ni/Al₂O₃ catalyst, a prereduction step or long induction period was required in order to reach catalytic activity and carbon deposition was favoured irrelevant to the pretreatment conditions. In strong contrast, the oxidized Ni₁₀Ce₉₀ showed a rapid startup operation and high

coking resistance (0.08 wt\% h^{-1}), while a low activity and negligible tendency to coking (0.01 wt\% h^{-1}) were found in prereduced $\text{Ni}_{10}\text{Ce}_{90}$. Comparing the oxidized and reduced $\text{Ni}_{10}\text{Ce}_{90}$, oxidized $\text{Ni}_{10}\text{Ce}_{90}$ was much more active than the reduced one and both samples showed the high resistance to carbon deposition and the continuous decrease of the conversions. S. Wang and G.Q. Lu reported that, in the catalytic activity tests after prereduction, Ni/CeO_2 showed much lower activity and carbon deposition relative to $\text{Ni}/\text{Al}_2\text{O}_3$ [52], in agreement with our results in Table 4.

In order to elucidate the effect of treatment conditions (oxidation, reduction, or inertness) on the catalytic activity in more detail, $\text{Ni}_{10}\text{Ce}_{90}$ catalysts were tested with different sequences of regeneration procedures as shown in Figure 25. In panel A of Figure 25, fresh $\text{Ni}_{10}\text{Ce}_{90}$ (after in situ oxidation) always exhibits an immediate high catalytic activity, which slowly decreases. After about 150 min of reaction time the catalyst was regenerated with air, in the other 2 experiments with Ar, and in the last with hydrogen (regeneration time always 30 min, not included in Figure 25). The results are depicted in Figure 25B. The treatment with air led to full recovery of the initial activity. After Ar treatment, deactivation continued. H_2 treatment led to a dramatic reduction of catalytic activity. After another 150 min of reaction time, the catalysts were regenerated again (see Figure 25C). When the air-regenerated catalyst was regenerated with air again, most of its activity was recovered. The catalyst regenerated originally with Ar recovered most of its original activity after regeneration with air, while deactivation continued when it was regenerated with Ar once more. The sample deactivated by the regeneration with hydrogen recovered only little of its original activity by the final air regeneration.

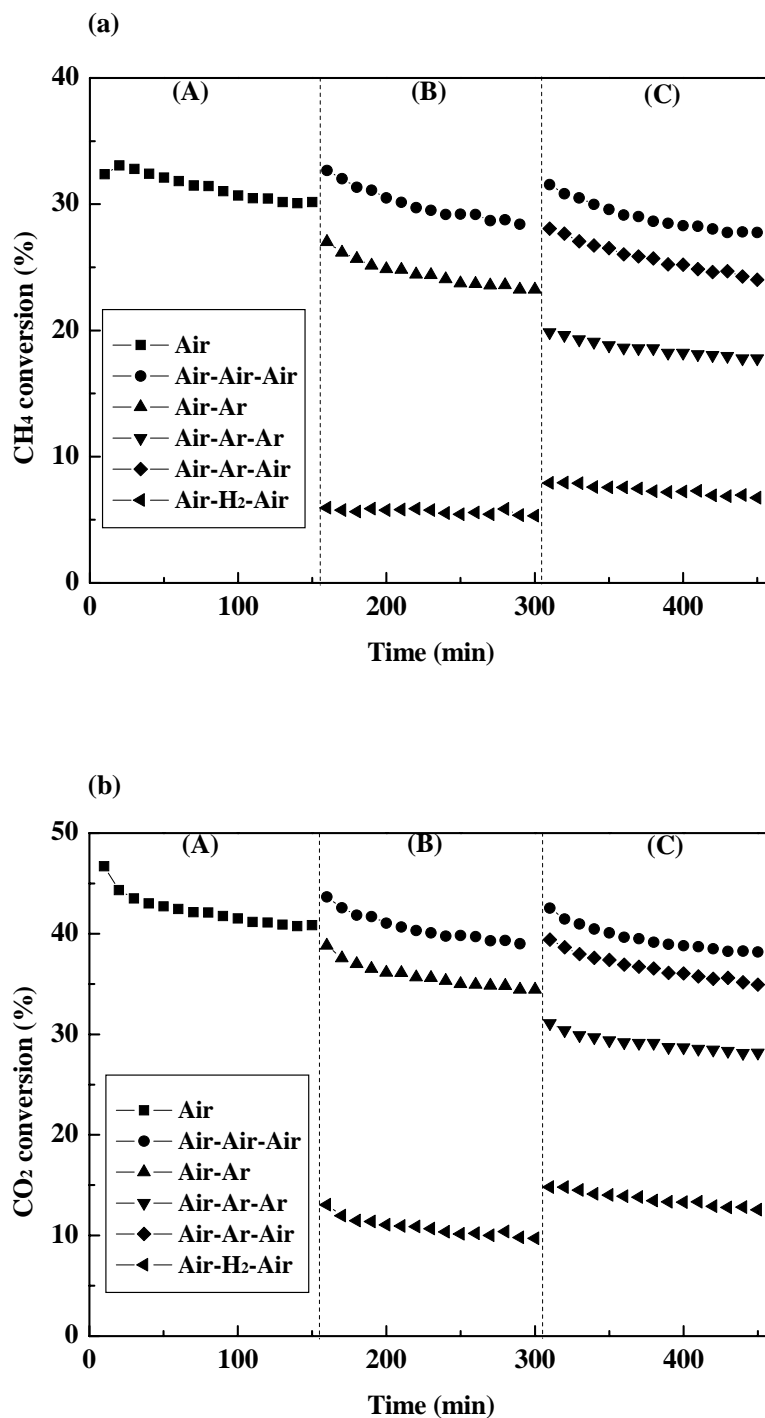


Figure 25. Time dependence of the catalytic activity and stability of 100 mg $\text{Ni}_{10}\text{Ce}_{90}$ on a variety of regeneration conditions: (a) CH_4 conversion and (b) CO_2 conversion. Operating conditions: $T = 600\text{ }^\circ\text{C}$; $P = 1\text{ bar}$; total flow: 65 ml min^{-1} ($\text{CH}_4/\text{CO}_2/\text{Ar} = 16.9/15.1/68$).

2.2.2. Characterization of Ni/Al₂O₃ catalyst

To see the effect of catalyst structure on the activity, XRD measurements were performed for the Ni/Al₂O₃ catalysts in as prepared state, after 2 h of reduction, and after 30 min and 380 min of reaction. In Figure 26 the XRD pattern of as prepared, reduced and tested Ni on γ -Al₂O₃ are shown in relation to the pure, undoped support. The XRD pattern of “as prepared” Ni/Al₂O₃ reveals the main peaks at $2\theta = 37.3^\circ$, 45.5° and 65.3° corresponding to the reflections (311), (400) and (440) of cubic Al₂O₃. The absence of reflections at $2\theta = 43.3^\circ$ and 63.0° indicates that no NiO has been formed in the Ni/Al₂O₃ catalyst. Possible reaction product of the wet impregnation method is the spinel phase NiAl₂O₄, which crystallizes isotypically to the γ -Al₂O₃ support in a fcc oxygen packing with partial occupation of voids. Because of this structure relation a solid solution between the two boundary phases is formed, which can be described by the formula Ni_{3x}Al_{8-2x}O₁₂ ($0 \leq x \leq 1$). Due to the very similar lattice dimensions, the composition of the product formed cannot be deduced from inspection of the diffraction pattern alone, instead of this a Rietveld refinement of the complete diffraction pattern seemed advisable. But on the other hand, the diffraction pattern in Figure 26 are characterized by very broad reflections due to the poor crystallinity and small crystallite size of the calcined reaction product, which hampered all results from Rietveld refinements because of the low significance level of the refinement results. Major difference between the diffraction pattern of NiAl₂O₄ and γ -Al₂O₃ is the intensity of the (222) reflection at about $2\theta = 39.4^\circ$ (compare Figures 26a and b). From the low intensity of the (222) reflection in the diffraction pattern of the reaction product, we deduce a spinel formation according to the formula given above with undetermined Ni content, in agreement with former investigations [41].

For the reduced Ni/Al₂O₃ catalyst, a new peak at $2\theta = 51.8^\circ$ as well as a line broadening at the lower angle side of the spinel (400) reflection at $2\theta = 45.5^\circ$ is interpreted as formation of metallic nickel. When a diffraction pattern was measured for the sample after the

reaction of fresh catalyst, no significant change was detectable after 30 min of reaction (not shown) compared with the as prepared Ni/Al₂O₃. Whereas after 380 min of reaction, the peak at $2\theta = 51.8^\circ$ and line broadening at the lower angle side of the spinel (400) reflection at $2\theta = 45.5^\circ$ are detectable as similarly to be recognized in the reduced catalyst, and very broad diffraction intensity around $2\theta = 26.4^\circ$ is assigned to the formation of carbon.

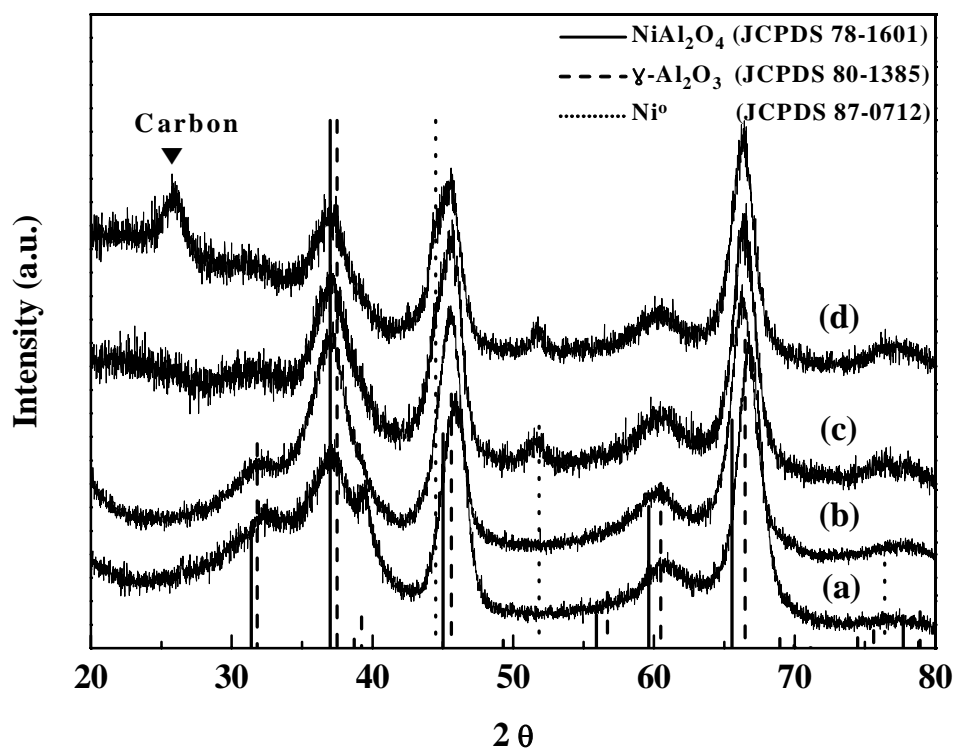


Figure 26. XRD patterns of as prepared, reduced and tested Ni/Al₂O₃ relative to the fine γ -Al₂O₃ support: (a) γ -Al₂O₃, (b) as prepared Ni/Al₂O₃, (c) reduced Ni/Al₂O₃ (after 2 h reduction of sample (b)), and (d) tested Ni/Al₂O₃ (after 380 min reaction of sample (b)).

In the catalytic testing, the oxidized Ni/Al₂O₃ kept the low initial activity until almost 80 min. From the XRD pattern of Ni/Al₂O₃ catalyst, the nickel in as prepared state was present

in the form of NiAl_2O_4 spinel which maintained its state for at least 30 min of reaction. The $\text{Ni}/\text{Al}_2\text{O}_3$ catalyst reduced for 2 h or tested for about 240 min revealed the high and stabilized catalytic conversions. Here, the Ni oxidation state was Ni^0 , which represents presumably an active center for the reforming reaction. Thus, the slow increase of conversion during the activation period is attributed to the continuous reduction of the $\text{Ni}_{3x}\text{Al}_{8-2x}\text{O}_{12}$ species by methane, which can be promoted by product gas (hydrogen) according to the following equation: $\text{Ni}_{3x}\text{Al}_{8-2x}\text{O}_{12} + 3x \text{H}_2 \rightarrow 3x \text{Ni} + (4-x) \text{Al}_2\text{O}_3 + 3x \text{H}_2\text{O}$. The XRD characterization of $\text{Ni}/\text{Al}_2\text{O}_3$ indicates that the catalytic activity change is correlated with the Ni oxidation state and the long induction period of $\text{Ni}/\text{Al}_2\text{O}_3$ catalyst is due to a slow decomposition of NiAl_2O_4 spinel to metallic nickel and Al_2O_3 .

Severe coke formation on the tested $\text{Ni}/\text{Al}_2\text{O}_3$ was supported by XRD and TPO studies. From the result of following pulse experiments for nickel oxide, reduced nickel has an ability of methane decomposition to generate H_2 and carbon and the surface carbon on metallic nickel is not apt to be removed by the gas phase component CO_2 . Additionally, it has been known that $\gamma\text{-Al}_2\text{O}_3$ is an irreducible support to hardly offer lattice oxygen [185]. Thus, a lack of oxygen supported from gas phase or catalyst support being capable of eliminating the surface carbon on Ni^0 contributes to the high coking tendency of $\text{Ni}/\text{Al}_2\text{O}_3$.

2.2.3. Characterization of Ni-Ce mixed oxide

XRD measurements were performed for $\text{Ni}_{10}\text{Ce}_{90}$ catalysts in as prepared state, after 2 h of reduction, and after 30 min and 600 min of reaction. For fresh CeO_2 and NiO prepared by the sol-gel method, the XRD pattern revealed a fluorite structure-type ($a = 5.4135(1) \text{ \AA}$) and cubic rock-salt structure ($a = 4.1793(1) \text{ \AA}$), respectively. These data were used as reference. The XRD patterns of the artificial sample (physical mixing of the nickel oxide and cerium oxide prepared by the sol-gel method, the molar ratio of $\text{Ni} : \text{Ce} = 1 : 9$) in as prepared and reduced

state are shown in Figures 27a and b. Clearly, the reflections of oxidized nickel, i.e. NiO (I_{100} at $2\theta=43.4^\circ$), on the as prepared sample and metallic nickel (I_{100} at $2\theta=44.5^\circ$) on the reduced one are detectable.

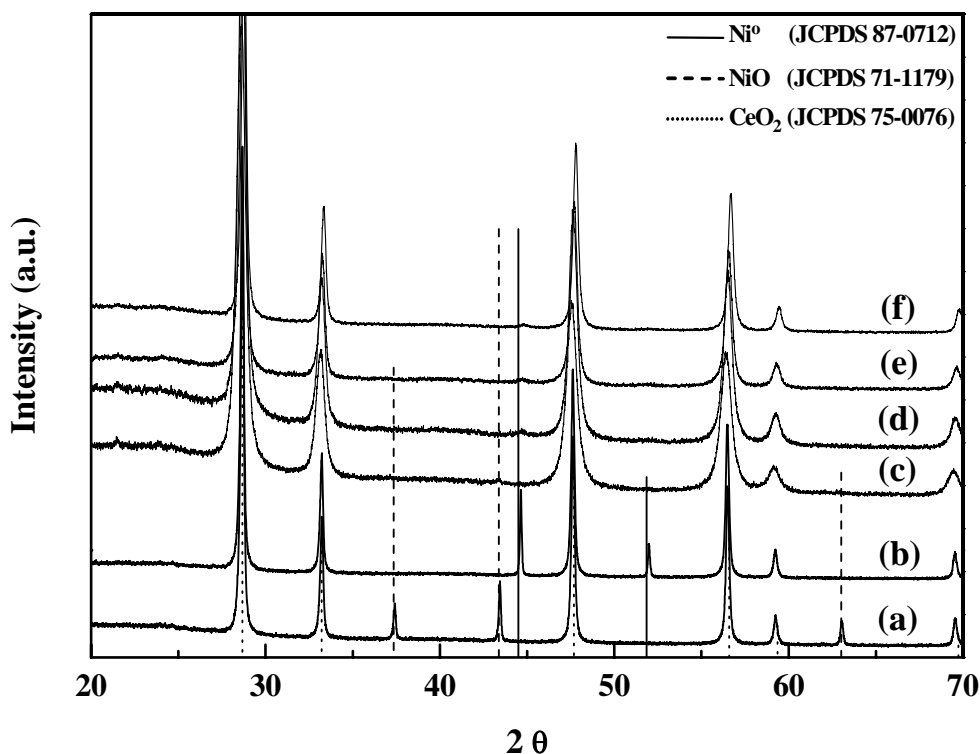


Figure 27. XRD patterns of (a) the as prepared artificial sample (physical mixing of the nickel oxide and cerium oxide prepared by the sol-gel method, the molar ratio of Ni:Ce = 1:9), (b) after reduction of sample (a), (c) the as prepared $Ni_{10}Ce_{90}$, (d) after reaction of sample (c), (e) after reduction of sample (c), and (f) after reaction of sample (e).

The XRD patterns of the as prepared, reduced and tested $Ni_{10}Ce_{90}$ catalysts are shown in Figures 27c - f. The patterns are dominated by the diffraction peaks of the ceria substrate revealing a much lower peak widths FWHM, i.e. a much better crystallinity and larger crystallite size compared to $\gamma-Al_2O_3$, but lower crystallinity as the pure oxide as prepared by the

sol-gel method. The reflections of oxidized nickel (I_{100} at $2\theta=43.4^\circ$) and metallic nickel (I_{100} at $2\theta=44.5^\circ$) on the catalysts are very weak, together with the line broadening indicating the presence of very small particles. The small metal particles and their high dispersion of $\text{Ni}_{10}\text{Ce}_{90}$ are presumably attributed to an intrinsic result of the acid catalyzed sol-gel preparation, well-known to provide atomically dispersed mixed oxides [162,163]. Moreover, a linear decrease of the CeO_2 lattice parameter with increasing Ni amount was identified, i.e. for the pure CeO_2 $a = 5.4135(1) \text{ \AA}$, for as prepared $\text{Ni}_{10}\text{Ce}_{90}$ $a = 5.4124(3) \text{ \AA}$, and for $\text{Ni}_{20}\text{Ce}_{80}$ $a = 5.411(1) \text{ \AA}$, which follows Vegard's law (see Figure 42 in chapter 2.3). This suggests an oxide solid solution formed in Ni-Ce mixed oxide system with incorporation of some Ni^{2+} ions into the ceria lattice, in agreement with former investigations [164,165]. The formation of the solid solution also seems due to the atomic dispersion of metal cations in the beginning of the acid catalyzed sol-gel process. The lack of a carbon peak (at $2\theta=26.4^\circ$) in the XRD patterns of tested samples confirms high coking resistivity of this $\text{Ni}_{10}\text{Ce}_{90}$ mixed oxide, which is consistent with our TPO study.

XPS was used to obtain further information about the valency/oxidation state of elements and surface composition of the Ni-Ce mixed oxide by inspecting the spectral line shape as well as the intensities of the Ce 3d and Ni 2p core level electrons. Due to the surface sensitivity of XPS, special precautions were taken to avoid any contact with air before introduction in the XPS analysis chamber. Additionally, the samples were mixed with zirconium to reduce charging of the non-conducting samples during the measurement, as described in the experimental section. Despite the comparable photoemission cross sections of Ce 3d and Ni 2p, the Ni 2p intensity strongly dropped below the nominal 10:90 ratio for the $\text{Ni}_{10}\text{Ce}_{90}$ catalysts, and due to the very weak intensities, even a qualitative interpretation of the Ni 2p line shape was not possible. Even in the case of $\text{Ni}_{20}\text{Ce}_{80}$ catalysts with the higher Ni/Ce ratio, the Ni 2p intensity was still very weak. In Figure 28, the Ce 3d spectra of $\text{Ni}_{20}\text{Ce}_{80}$ catalyst in as prepared state, after reduction for 2 h, and after reaction for 2 h are presented and are

compared to the Ce 3d spectra of Ce_2O_3 and CeO_2 [186,187]. According to literature data [164,178,188], the CeO_2 spectrum (representing Ce^{4+}) is labelled by v, v', v'' and u, u', u'' , describing the $3d_{5/2}$ and $3d_{3/2}$ photoelectron intensities for $4f^2, 4f^1, 4f^0$ occupation, while v' and u' represents the lower binding energy intensities of the $3d_{5/2}$ and $3d_{3/2}$ electrons for the $4f^1/4f^2$ configuration in Ce_2O_3 (representing Ce^{3+}). By comparing the observed 3d envelope with those previously reported for Ce^{4+} and Ce^{3+} [178,186-188], the Ce 3d spectra of the catalysts in Figures 28a-c are very similar to the Ce 3d spectrum of CeO_2 (cf., e.g., the strong $3d_{3/2}$ ($4f^0$) contributions (u''), that are missing in Ce_2O_3 [187]) and therefore, the Ce is mainly of Ce^{4+} character. But in the cases of Figures 28b and c, i.e. after reduction as well as after reaction, the spectra also exhibit clearly visible v' and u' contributions, indicating, that the catalysts then also contain small amounts of Ce^{3+} . Thus, the surface of both the reduced and used samples is formed by a mixture of Ce^{4+} and Ce^{3+} , while the surface of the fresh catalysts seems to be formed by Ce^{4+} , exclusively.

From XPS analysis, as a surface sensitive technique (with a probing depth of about 1-2 nm), the distribution of Ce and Ni seems to be not homogeneous within the catalyst, at least within an area of a few atomic layers. Due to the nearly vanishing Ni intensities (not shown), the probed surface area of a single grain must be strongly enriched with Ce, or, on the other hand, the inner core of the grain must be enriched with Ni.

A slow but continuous deactivation during the reaction and dramatic loss of catalytic activity after hydrogen treatment were observed for the $\text{Ni}_{10}\text{Ce}_{90}$ catalyst. By BET measurements, the surface area of $\text{Ni}_{10}\text{Ce}_{90}$ showed no obvious change within experimental error after 10 h of reaction (decrease from 36.9 to 35.2 $\text{m}^2 \text{g}^{-1}$) or 2 h of reduction (increase from 36.9 to 38.2 $\text{m}^2 \text{g}^{-1}$), indicating that no sintering effect occurs under our conditions. Moreover, XRD characterization and TPO study of tested $\text{Ni}_{10}\text{Ce}_{90}$ exhibited negligible coke formation. Therefore, the deactivation observed during the reaction or reduction is more likely due to a loss of active sites. Since the XRD reflections corresponding to Ni phase of the

$\text{Ni}_{10}\text{Ce}_{90}$ catalyst were very weak, together with line broadening due to its very small particles of high dispersion or the formation of Ni-Ce solid solution, the oxidation state of nickel could not be determined from the XRD measurement alone. From XPS analysis, the mixture of Ce^{4+} and Ce^{3+} was identified in the surface of both reduced and tested Ni-Ce mixed oxide. But, the valance state of nickel was unclear due to its very weak intensities. To shed more light on the species of active site, a series of pulse experiments was carried out.

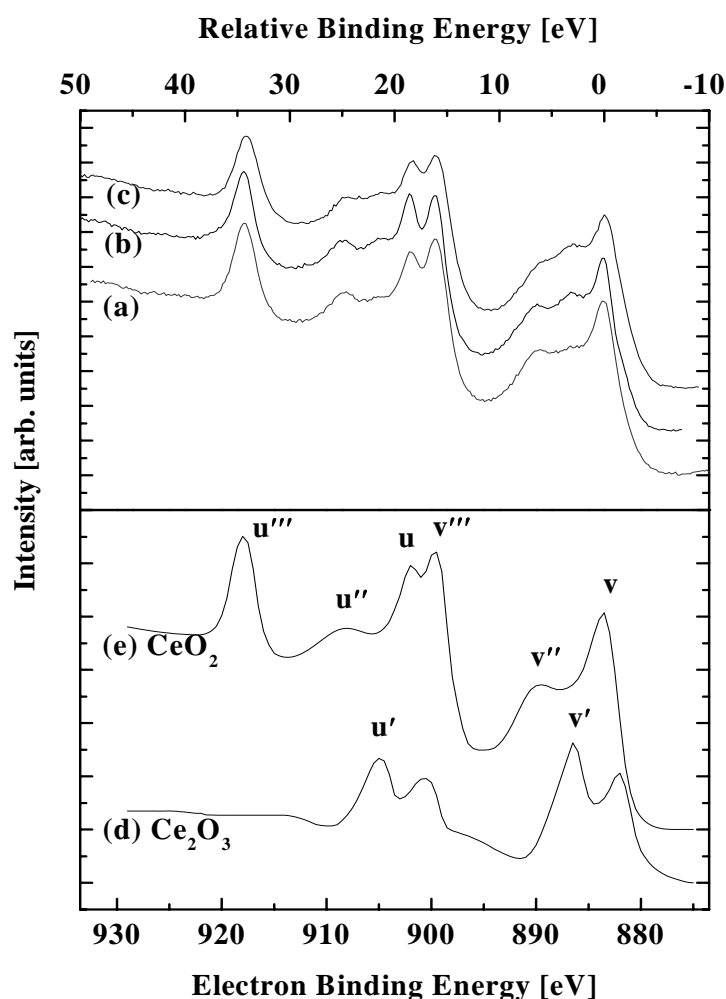


Figure 28. Ce 3d XPS spectra for (a) as prepared $\text{Ni}_{20}\text{Ce}_{80}$, (b) reduced $\text{Ni}_{20}\text{Ce}_{80}$ (after 2 h reduction of sample (a)), and (c) tested $\text{Ni}_{20}\text{Ce}_{80}$ (after 2 h reaction of sample (a)). The spectra for Ce_2O_3 (d) and CeO_2 (e) are taken from ref. [187], the original data were published in ref. [186]

2.2.4. Pulse experiments

General

Pulse experiments have been performed as a useful tool for mechanistic studies of the methane dry reforming on prereduced Pt/ZrO₂ [166,167], Pt/Al₂O₃ [167], Pd/CeO₂ [168], Pd/ZrO₂ [168], Rh/Al₂O₃ [74], and fresh CeO₂ [169] catalysts. During pulse experiment, gas pulses (CH₄, CO₂ or H₂) with a volume of 100 μl (ca. 4.07 μmol) were passed at 600 °C over the catalyst sample using Ar as carrier gas (30 ml min⁻¹). The break between consecutive pulses was 5 min. The pulses of a different gas were introduced after stabilization for 30 min in flowing Ar (30 ml min⁻¹) at 600 °C. The products were monitored on-line by a quadrupole mass spectrometer. The argon intensity of each pulse was chosen for internal standardization as representative within the chronological progress recording the detection sensitivity over the whole experiment. The normalized areas under a peak were integrated and then converted to molar fraction using a conversion factor that was determined after the experiments. Figure 29 demonstrates the procedure of normalization of raw data with respect to the argon intensity followed by transformation of integrated areas to molar fraction using a conversion factor.

Prior to taking the pulse data, the catalyst was treated for 150 min in a flow of Ar instead of air. In the case of air pretreatment, additional 7 hours were required to stabilize mass-spectrometric response signals of nitrogen and oxygen in flowing Ar. Since no activity difference depending on *in situ* air or Ar pretreatment at 600 °C was found in reaction tests for 10 h (not shown), all samples were treated in flowing Ar for 150 min before a pulse experiment. Thus, in the system of CH₄ or H₂ pulsed experiment, the only source of oxygen is the catalyst itself. Among the products (i.e., H₂, H₂O, CO, and CO₂), the detection time of 5 min was not sufficient for water due to interaction with the walls of the capillary connecting the reactor with the QMS. Therefore, the amount of water released was determined indirectly based on the amount of educt-pulses consumed.

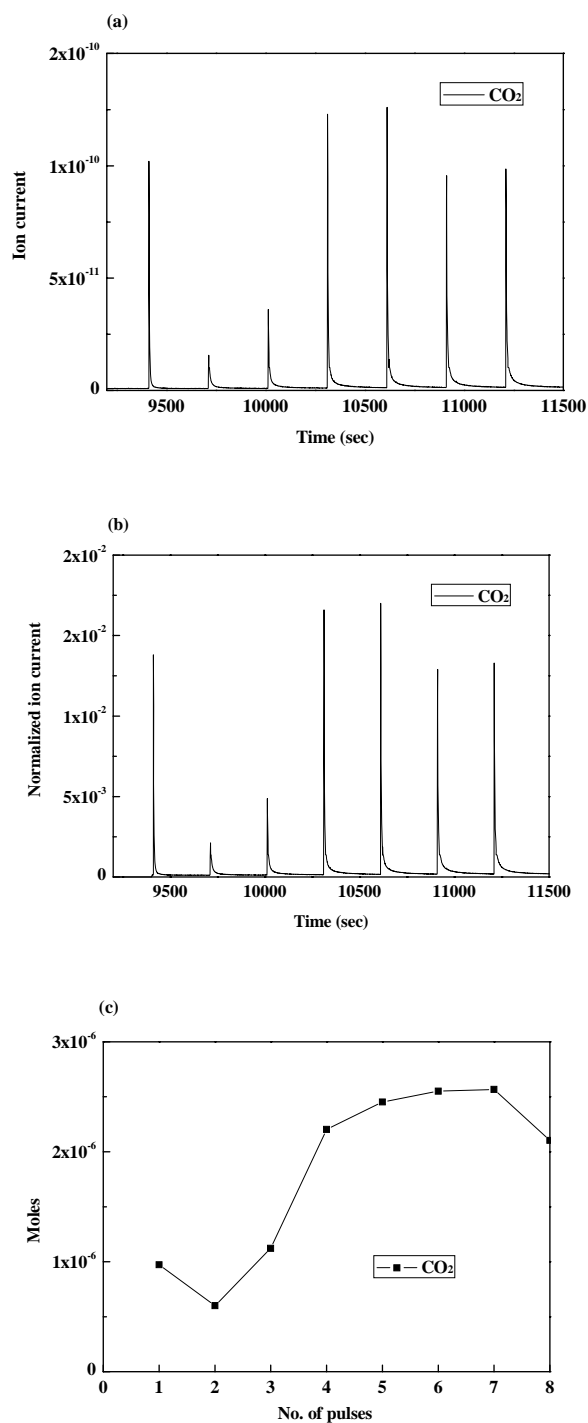


Figure 29. Example of procedures obtaining pulse data: (a) raw MS data, (b) normalized data with respect to argon intensity (internal standard), and (c) molar fraction of integrated areas using a conversion factor. Operating conditions: $T = 600 \text{ }^\circ\text{C}$; $P = 1 \text{ bar}$; Ar flow: 30 ml min^{-1} ; pulse volume: $100 \text{ }\mu\text{l}$ ($4.07 \text{ }\mu\text{mol}$).

A blank reaction test without catalyst confirmed the reactor itself was not catalytically active. The formation of trace amounts of products during the blank tests (less than 0.5 % of that during the blank test of the product gases) is attributed to thermal reaction and registered as background. The conditions of pulse experiments are summarized in Table 5. The carbon balance was determined by [(the sum amount of CO and CO₂ produced)/(the amount of CH₄ consumed)] for CH₄ pulses and [(the amount of CO produced)/(the amount of CO₂ consumed)] for CO₂ pulses.

Table 5. Conditions of pulse experiments^a

Catalyst	W _{catal.} (mg)	Pulse sequence					Pulse No.
Empty	0	CH ₄	-	CO ₂			15-15
CeO ₂	100	CH ₄	-	CO ₂			15-15
	100	H ₂	-	CH ₄	-	CO ₂	8-8-7
NiO	20	CH ₄	-	CO ₂			15-15
	20	H ₂	-	CH ₄	-	CO ₂	15-19-15
	4.60	H ₂	-	CH ₄	-	CO ₂	15-15-15
Ni ₁₀ Ce ₉₀	100	CH ₄	-	CO ₂	-	CH ₄	20-20-20
	100	H ₂	-	CH ₄	-	CO ₂	15-15-15

^a Operating conditions: T = 600 °C; P = 1 bar; Ar flow: 30 ml min⁻¹; pulse volume: 100 μl (4.07 μmol).

Cerium oxide

When CH₄ or CO₂ pulses were applied to 100 mg ceria, there was no detectable product formation exceeding the background. Attempts to activate the ceria by H₂ pulses also failed. This denotes a negligible interaction of ceria with CH₄, CO₂ or H₂ at 600 °C, which is in perfect agreement with literature data (the oxidation of CH₄ by CeO₂ becomes thermodynamically viable only at temperatures higher than 650 °C [169] and the reduction peak of pure CeO₂ in the H₂-TPR profile was observed at about 830 °C [165]).

Nickel oxide

During the experiment of 15 CH₄ followed by 15 CO₂ pulses on 20 mg of nickel oxide again no catalytic activity was detectable, while 15 pulses of H₂ over the NiO resulted in quantitative conversion. This indicates that hydrogen is a stronger reducing agent for the NiO than methane. In panel A of Figure 30, the amount of water released is determined indirectly by the amount of H₂ consumed. While the amount of oxide oxygen calculated in 20 mg NiO is 26.8×10^{-5} mol, the amount of oxygen consumed by the H₂-pulses is 6.1×10^{-5} mol for quantitative conversions, as summarized in Table 6. The mechanism of NiO reduction by hydrogen has been examined by J.A. Rodriguez et al. [170], who observed that crystalline or powdered forms of NiO are directly reduced to metallic nickel at 400-460 °C without detectable formation of intermediate phases.

Table 6. The amount of oxygen consumed during the pulse experiments

Catalyst	W _{catal.} (mg)	Theor. oxygen amount ($\times 10^{-5}$ moles) ^a	Consumed oxygen amount for complete oxidation of the reducing agent ($\times 10^{-5}$ moles) ^b				Pulse No.
			H ₂	-	CH ₄	Sum	
NiO	20	26.8	6.1	-	8.7	14.8	15-19
	4.60	6.2	5.6	-	0.9	6.4	15-15
Ni ₁₀ Ce ₉₀	100	6.2			6.5	6.5	0-20
	100	6.2	5.7	-	0.9	6.6	15-15

^a The amount of oxygen contained in Ni-O is calculated on the basis of the catalysts weight.

^b The amount of consumed oxygen for complete oxidation is calculated on the basis of the hydrogen consumption for H₂ pulses and the CO₂ production for CH₄ pulses.

When the partly reduced NiO was exposed to additional 19 pulses of CH₄, H₂O and CO₂ were produced with no decrease in activity and negligible formation of H₂ and CO, consuming another 8.7×10^{-5} mol of the remaining oxygen in the NiO (see Figure 30B). In panel B of Figure 30, the amount of H₂O is determined indirectly by [(the amount of CH₄ consumed)-

0.5*(the amount of H₂ produced)]*2 although it was unstable due to the lack of stability of the reaction. Since unreduced NiO does not convert CH₄, the Ni⁰ produced by the preceding H₂-pulses must be the active sites. When an additional 15 CO₂-pulses were now applied to this highly reduced Ni⁰/NiO, no products were detectable, which implies that the partially reduced nickel oxide cannot dissociate CO₂ for complete or partial reoxidation.

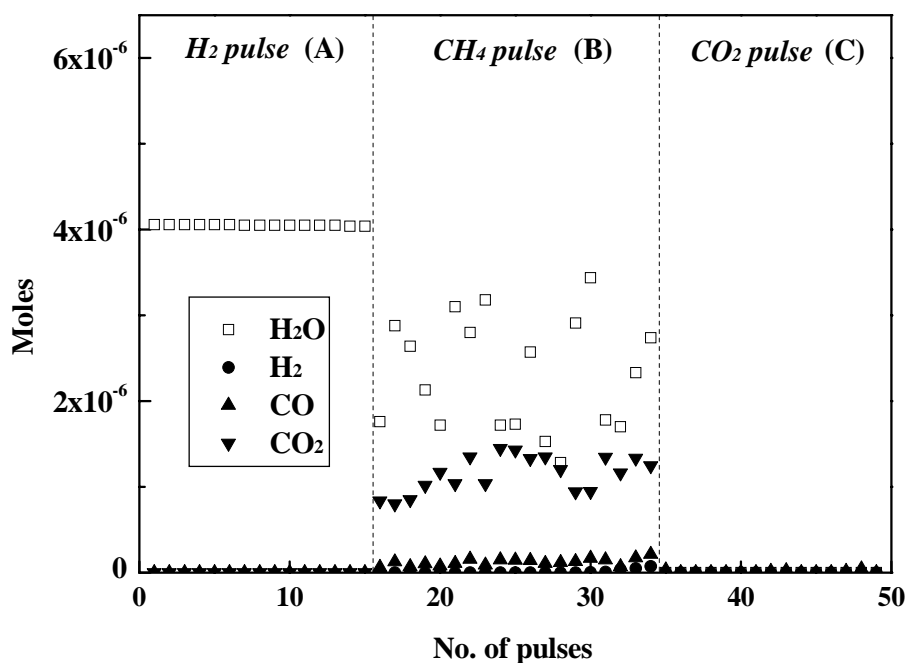


Figure 30. The amount of products from consecutive pulses of (A) 15 H₂, (B) 19 CH₄, and (C) 15 CO₂ over 20 mg NiO. The amount of H₂O is determined indirectly by the amount of H₂ consumed in panel A and by [(the amount of CH₄ consumed)-0.5*(the amount of H₂ produced)]*2 in panel B. Operating conditions: T = 600 °C; P = 1 bar; Ar flow: 30 ml min⁻¹; pulse volume: 100 μl (4.07 μmol).

The experiment was repeated with only 4.6 mg NiO corresponding to the amount of nickel oxide in 100 mg Ni₁₀Ce₉₀. The amount of oxide oxygen calculated in 4.6 mg NiO is 6.2×10⁻⁵ mol. Figure 31 gives the amount of products during the experiment of consecutive 15

H₂ – 15 CH₄ - 15 CO₂ pulses. In Figure 31, the amount of water released is determined indirectly by the amount of H₂ consumed in panel A and by [(the amount of CH₄ consumed)-0.5*(the amount of H₂ produced)]*2 in panel B, respectively. With the reduced amount of NiO the H₂ conversion began to decrease after 4 pulses (see Figure 31A), indicating that most, but not all NiO was reduced. From Figure 31A it can be estimated, that about 5.6×10^{-5} mol of oxygen are consumed by the hydrogen, which corresponds to approximately 90 % of the oxygen content of the NiO.

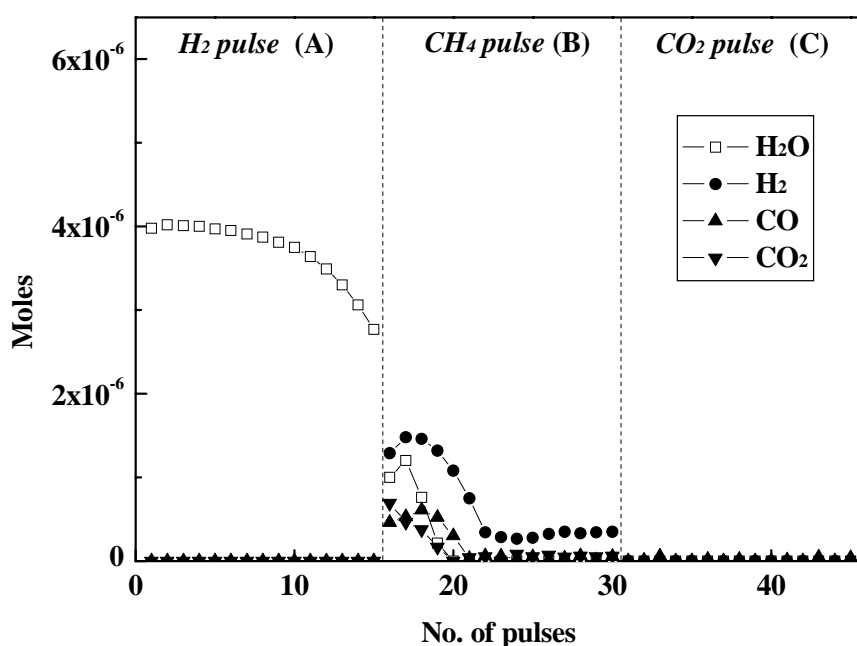


Figure 31. The amount of products from 15 consecutive pulses of (A) H₂, (B) CH₄, and (C) CO₂ over 4.60 mg NiO. The amount of H₂O is determined indirectly by the amount of H₂ consumed in panel A and by [(the amount of CH₄ consumed)-0.5*(the amount of H₂ produced)]*2 in panel B. Operating conditions: T = 600 °C; P = 1 bar; Ar flow: 30 ml min⁻¹; pulse volume: 100 μl (4.07 μmol).

When the 15 CH₄ pulses were applied to this highly reduced NiO, only the first 5 CH₄ pulses produced still a little H₂O and CO₂ next to H₂ and CO, all of which rapidly declined (see

Figure 31B). The formation of H₂O and CO₂ is attributed to the complete oxidation of methane with the oxygen remaining in NiO as described in the study of 20 mg NiO. The sum amount of oxygen consumption for the formation of H₂O and CO₂ in Figure 31A and B was 6.4×10^{-5} mol, as summarized in Table 6. H₂/CO ratios were about 3 until pulse 5. A H₂/CO ratio above 2 indicates carbon formation on the catalyst surface. After pulse 6, hydrogen remained the only significant product. Apparently the remaining oxygen in the NiO is consumed by the first 5 methane pulses and methane decomposition dominates on the reduced nickel to generate carbon and H₂. When the experiment was continued with CO₂ pulses, no product was detectable (see Figure 31C). This proves that the carbon on metallic nickel derived from the methane decomposition does not react with CO₂ from the gas phase, and it confirms further that the metallic nickel is incapable of dissociating CO₂ for reoxidation of Ni. No interaction between the carbon on metallic nickel and gas phase CO₂ can explain the formation of non-removable carbon on Ni/Al₂O₃. This is quite different from the result with prerduced Rh/Al₂O₃ where most of the surface carbon on Rh is successfully oxidized to CO by CO₂ from the gas phase (Eley–Rideal type mechanism) [74].

Ni₁₀Ce₉₀ mixed oxide

The products from consecutive 20 CH₄ - 20 CO₂ - 20 CH₄ pulses on 100 mg Ni₁₀Ce₉₀ at 600 °C are depicted in Figure 32. In panel A of Figure 32, the amount of H₂O is determined indirectly by [(the amount of CH₄ consumed)-0.5*(the amount of H₂ produced)]*2. When the first 8 CH₄ pulses were introduced to Ni₁₀Ce₉₀, H₂O and CO₂ were the main products. H₂O/CO₂ ratios of about 2 and carbon balances of unity were found (see panel A of Figure 32b), implying that the complete oxidation of methane occurred without carbon formation. Furthermore, there seems to be a formation period, since highest activity is reached only after 5 pulses.

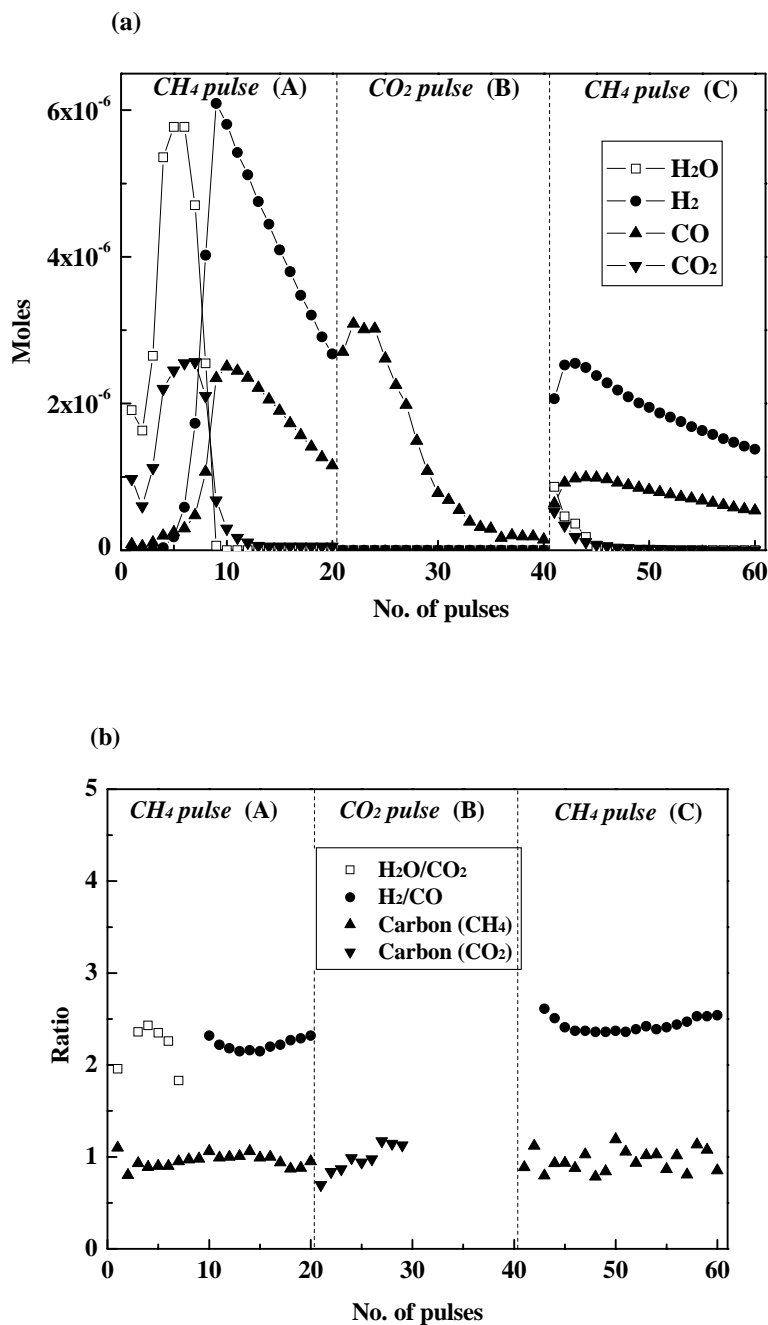


Figure 32. (a) The amount of products from 20 consecutive pulses of (A) CH_4 , (B) CO_2 , and (C) CH_4 over 100 mg $\text{Ni}_{10}\text{Ce}_{90}$. (b) The ratio of (\square) $\text{H}_2\text{O}/\text{CO}_2$, (\bullet) H_2/CO , (\blacktriangle) carbon determined by [(the sum amount of CO and CO_2 produced)/(the amount of CH_4 consumed)] for CH_4 pulses, and (\blacktriangledown) carbon determined by [(the amount of CO produced)/(the amount of CO_2 consumed)] for CO_2 pulses. The amount of H_2O is determined indirectly by [(the amount of CH_4 consumed) - 0.5*(the amount of H_2 produced)]*2. Operating conditions: $T = 600\text{ }^\circ\text{C}$; $P = 1\text{ bar}$; Ar flow: 30 ml min^{-1} ; pulse volume: $100\text{ }\mu\text{l}$ ($4.07\text{ }\mu\text{mol}$).

Since this catalyst was not reduced, the question can then be asked where this reaction occurs. Neither NiO nor CeO₂ activate CH₄ as has been shown. Therefore, it is assumed that the interfacial oxygen in the Ni-Ce boundary (Ni-O-Ce site) is the active component for the complete oxidation of methane. This is not unreasonable, since several studies point to the formation of M-O-CeO₂ surface complexes with metals such as Pd, Pt, Rh, and Au at the interface (see Figure 33) [171,172,189,190]. As summarized in Table 6, the oxygen consumed by total methane oxidation on the Ni₁₀Ce₉₀ is 6.5×10^{-5} mol, which corresponds to about the total oxygen content of the Ni-oxygen in the catalyst. Moreover, for the Ni₂₀Ce₈₀ mixed oxide the amount of oxygen consumed by total methane oxidation (15.5×10^{-5} mol) is increased by factor of 2.3 relative to Ni₁₀Ce₉₀ (see Figure 43 in chapter 2.3).

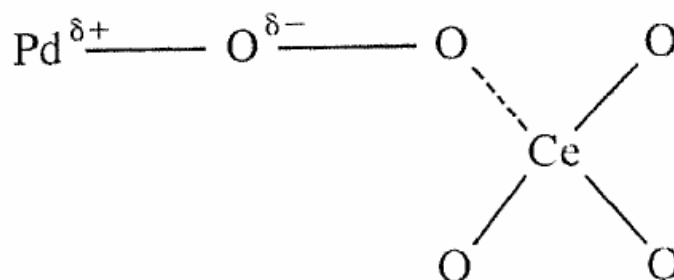


Figure 33. Proposed structure of the oxidized surface species on Pd/CeO₂ catalyst system [171].

After the 8th pulse, the formation of CO₂ and H₂O ceased and the product was dominated by H₂ and CO, whose formation continuously decreased. Here, the oxygen consumed must originate from the ceria lattice. It is believed that storage oxygen in the ceria is provided to the active Ni-Ce sites which are now depleted of the original oxygen, leading to the creation of oxygen vacancies in the ceria. The amount of syngas formed is conceivably based on the diffusion rate of lattice oxygen correlated to oxygen concentration gradient. The H₂/CO ratios produced remained close to 2 and carbon balances were about unity (see panel A of Figure 32b). Therefore, no indication for carbon deposition on the Ni₁₀Ce₉₀ by CH₄ pulses was obtained.

When the catalyst is now subjected to CO₂ pulses, CO₂ is converted exclusively into an equivalent of CO as shown in panel B of Figure 32. The total amount of CO obtained from CO₂ during the 20 pulses was 2.51×10^{-5} mol. Since CO₂ pulses revealed no activity with the as prepared Ni₁₀Ce₉₀ (not shown) as well as with reduced nickel (see Figure 31C), the CO formation either indicates, that reduced Ni-Ce sites are reoxidized or that the ceria oxygen vacancies created during the methane pulses 8-20 are supplemented by CO₂ dissociation. From the result of the following 20 CH₄ pulses (see below), the CO formation seems to arise from the reoxidation of the ceria oxygen vacancies. When compared with the total amount of CO released from the CH₄ pulses in panel A (2.55×10^{-5} mol), the oxygen vacancies are fully replenished by CO₂ dissociation. Comparing the CO production rate of two processes (creation and recovery of oxygen vacancies) in Figure 32a, the supplement of oxygen vacancies in panel B is clearly faster than their generation in panel A, indicating that the oxygen vacancies react extremely fast with CO₂ to be easily replenished.

The following 20 CH₄ pulses produced essentially H₂ and CO and only trace amounts of H₂O and CO₂. The amount of H₂O and CO₂ released in Figure 32C dramatically decreases compared with that in Figure 32A. Since regeneration of the Ni-O-Ce-sites should have led to total oxidation, this supports that the oxygen used for the initial formation of H₂O and CO₂ is not regenerated and only ceria oxygen vacancies are reoxidized by the CO₂ treatment. CO₂ dissociation apparently allows the recharge of the oxygen vacancies in the ceria lattice, but not a direct recharge of the consumed interfacial oxygen of the Ni-Ce boundary. H₂/CO ratios were about 2 although they slightly increased in comparison with those of the first 20 CH₄ pulses. After the full supplementation of oxygen vacancies by CO₂ dissociation, the deactivation for syngas production was getting much slower but the amount of H₂ and CO released decreased remarkably (compare Figure 32A and C). This might be due to microstructural changes during the depletion of reactive oxygen by the continuing methane pulses.

Another series of pulse experiments was conducted, starting with H₂-pulses. The

continuous results of the 15 H₂ - 15 CH₄ - 15 CO₂ pulses on 100 mg Ni₁₀Ce₉₀ are revealed in Figure 34. While the first 10 pulses of hydrogen were converted completely, the conversion dropped during the remaining 5 pulses. Total oxygen consumption was 5.7×10^{-5} mol. During the following 15 CH₄ pulses the small amount of CO₂ initially formed corresponds to the 0.9×10^{-5} mol of oxygen remaining in the NiO. The sum amount of oxygen consumption for the formation of H₂O and CO₂ in Figures 34A and B is 6.6×10^{-5} mol - very close to the total oxygen content of the NiO in the catalyst

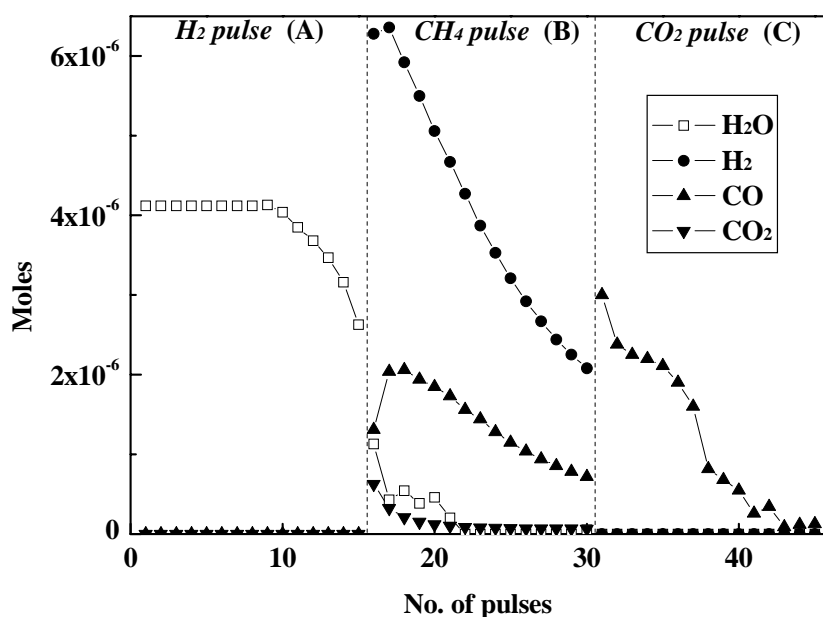


Figure 34. The amount of products from 15 consecutive pulses of (A) H₂, (B) CH₄, and (C) CO₂ over 100 mg Ni₁₀Ce₉₀. The amount of H₂O is determined indirectly by the amount of H₂ consumed in panel A and by [(the amount of CH₄ consumed)-0.5*(the amount of H₂ produced)]*2 in panel B. Operating conditions: T = 600 °C; P = 1 bar; Ar flow: 30 ml min⁻¹; pulse volume: 100 μl (4.07 μmol).

In panel B, the product is dominated by H₂ and CO formation in amounts comparable to those formed during the CH₄ pulses in Figure 32A. Considering the total amount of oxygen

consumption for the complete oxidation of methane in Figure 34A (6.5×10^{-5} mol), the similar behaviour and amount of production seem to be reasonable because of its generation on similar amounts of the active Ni-Ce sites. When the 15 CO₂ pulses were applied to Ni₁₀Ce₉₀, CO₂ was converted exclusively again into an equivalent of CO. Sum amount of CO obtained was 2.01×10^{-5} mol. As compared with the sum amount of CO released by CH₄ (2.07×10^{-5} mol), the ceria oxygen vacancies were completely replenished again by CO₂ dissociation.

2.2.5. Suggested mechanism

From this investigation, the interfacial oxygen in the Ni-Ce boundary of the Ni₁₀Ce₉₀ catalyst seems to be an active component for the complete oxidation of methane, because (i) nickel oxide or cerium oxide itself shows no activity with methane, (ii) the amount of oxygen consumed by the total oxidation of methane on Ni₁₀Ce₉₀ is close to the total oxygen content of the Ni-oxygen in the catalyst (see Table 6), and (iii) for Ni₂₀Ce₈₀ the amount of oxygen consumed by the complete oxidation of methane increases by factor of 2.3 compared to Ni₁₀Ce₉₀. Therefore, 1 mol CH₄ is converted to 2 mol H₂O and 1 mol CO₂ at the Ni-Ce boundary accompanying the consumption of the interfacial oxygen. The resulting site is considered as the active site for the reforming reaction where subsequently 1 mol CH₄ is reformed through the reaction with the oxygen migrated from ceria lattice to release 2 mol H₂ and 1 mol CO. The reaction is concomitant with the creation of oxygen vacancies of the ceria lattice. Thereafter, the oxygen vacancies are supplemented by oxygen arising from the dissociative adsorption of 1 mol CO₂ to produce 1 mol CO. However, the consumed interfacial oxygen in the Ni-Ce boundary cannot be recovered by CO₂ dissociation.

Based on these suggestions, the origin of unusual Ni₁₀Ce₉₀ mixed oxide properties for the CO₂ reforming of methane can be discussed. First, the catalytic property in the absence of a prereduction step relies on the reactivity of oxygen contained in the Ni species. The immediate

activity of $\text{Ni}_{10}\text{Ce}_{90}$ is based on the active interfacial oxygen in the Ni-Ce boundary (Ni-O-Ce site) which leads to the complete oxidation of methane and the creation of active sites for the following reforming reaction, while the strong interaction of NiAl_2O_4 spinel retards the activity of $\text{Ni}/\text{Al}_2\text{O}_3$. Second, the coking resistance relies on the reactivity of lattice oxygen in the catalyst support. The ceria lattice oxygen with high mobility participates in the reforming reaction through migration, leading to the formation of CO and oxygen vacancies of ceria lattice. On the other hand, there is no interaction between the surface carbon on metallic nickel and lattice oxygen of $\gamma\text{-Al}_2\text{O}_3$, resulting in the formation of non-removable carbon in $\text{Ni}/\text{Al}_2\text{O}_3$ catalyst. Finally, based on the negligible amount of surface area loss and coke formation during reaction, the continuous deactivation behaviour of $\text{Ni}_{10}\text{Ce}_{90}$ mainly occurs due to a loss of active sites. In the pulse experiment of $\text{Ni}_{10}\text{Ce}_{90}$, the continuing consumption of reactive oxygen in the condition of no supplement or delayed replenishment results in deactivation. Thus, in the CO_2 reforming of methane reaction, a balanced rate between the generation and supplement of oxygen vacancies seems to be required to avoid deactivation.

2.3. Composition and dopant effect on Ni-Ce mixed oxide

In chapter 2.1, from the results of the high-throughput experiment and their confirmation in a conventional manner, a non-precious metal catalyst, Ni₁₀Ce₉₀ mixed oxide was noted as a unique catalyst to show a rapid activation in the absence of catalyst prereduction and high coking resistance as well as high activity in the CO₂ reforming of methane. But, a slow but continuous deactivation of the catalyst was also recognized. In chapter 2.2, the exceptional properties of Ni₁₀Ce₉₀ mixed oxide were demonstrated by X-ray diffraction (XRD) and pulse experimentation, and from those results a reaction mechanism was proposed.

In chapter 2.1, the catalyst deactivation behaviour was improved with the help of high-throughput methods. Best results were determined by doping with 15 mol% Al or Zr in Ni₁₀Ce₇₅. Here, the doping effect on the catalytic activity and stability are investigated for Zr doped Ni₁₀Ce catalysts and the Ni-Cu-Ce ternary mixed oxides as a model system.

2.3.1. Ni_xCu_yCe_z mixed oxides

The automated synthesis of a Ni_xCu_yCe_z mixed oxide library ($0 \leq x, y, z \leq 100$, 10 mol% increment) with 66 ternary compositions was performed using a commercial pipetting robot. The procedure similar to that described in sol-gel preparation method 3 (see chapter 3.1) was used for library synthesis. The catalyst library was screened in a simple high-throughput reactor system at 600 °C connected to a micro-gas chromatograph for product analysis. In a standard high-throughput screening, the sampling needle was kept inside the hole for 820 s with six GC runs or for 3850 s with 28 GC runs to evaluate the activity and stability of each catalyst. Catalyst activity and stability was determined by the amount of CO produced and its deactivation rate, respectively. Stability tests take a longer time than initial activity tests. However,

the stability test can eliminate false positives (i.e., rapidly deactivating materials) and false negatives (i.e., materials that activate slowly). The chemical composition of each catalyst in the library was verified by XRF.

Each position of the $\text{Ni}_x\text{Cu}_y\text{Ce}_z$ ($0 \leq x, y, z \leq 100$, 10 mol% increment) library with 66 ternary compositions was tested during 820 s with six GC runs. After sequential testing of whole compositions, the relative activity (%) for the $\text{Ni}_x\text{Cu}_y\text{Ce}_z$ library was presented relative to the activity of the reference catalyst $\text{Rh}_1\text{Zr}_{20}\text{Al}_{79}$, as shown in Figure 35. The color corresponds to the measured relative activity. As shown in Figure 35a, the comparable activities in the first measurements were observed for the Ni-Ce mixed oxides with Cu addition of 0 and 10 % except $\text{Cu}_{10}\text{Ni}_{90}$, and Ni-Cu-Ce mixed oxides with Cu addition of 20 and 30 % in the ceria rich region such as $\text{Ni}_{10}\text{Cu}_{20}\text{Ce}_{70}$, $\text{Ni}_{20}\text{Cu}_{20}\text{Ce}_{60}$, $\text{Ni}_{30}\text{Cu}_{20}\text{Ce}_{50}$, and $\text{Ni}_{10}\text{Cu}_{30}\text{Ce}_{60}$. In the second measurements, most mixed oxides showed the comparable activities except the Cu-Ce mixed oxides without Ni addition, $\text{Ni}_{10}\text{Cu}_{90}$, and pure Ni as shown in Figure 35b. After the second measurements, CO production on most catalysts continuously decreased as shown in Figure 35c–f. From the results, it can be thought the Cu component doped in Ni-Ce mixed oxide retards the property of autoactivation. In Figure 36, the first and second measurements data of $\text{Ni}_x\text{Cu}_y\text{Ce}_z$ ternary composition spreads are approximated within the search space by using Kriging method with aid of S. Sieg [173]. The color in this figure corresponds to the estimated relative activity.

Considering the stability determined by deactivation rate, the most stable compositions were involved in the Ni-Ce mixed oxides without Cu addition. It was reported that $\text{CuNi}/\text{Al}_2\text{O}_3$ catalysts added over 5 % Cu deactivated more rapidly than the $\text{Ni}/\text{Al}_2\text{O}_3$ catalyst without Cu component while 1 % Cu addition enhanced the stability and the activity [174]. Similarly, in the high-throughput screening for activity and stability on $\text{Ni}_x\text{Cu}_y\text{Ce}_z$ ternary mixed oxides, the addition of Cu component led to a negative effect on the stability as well as initial activity.

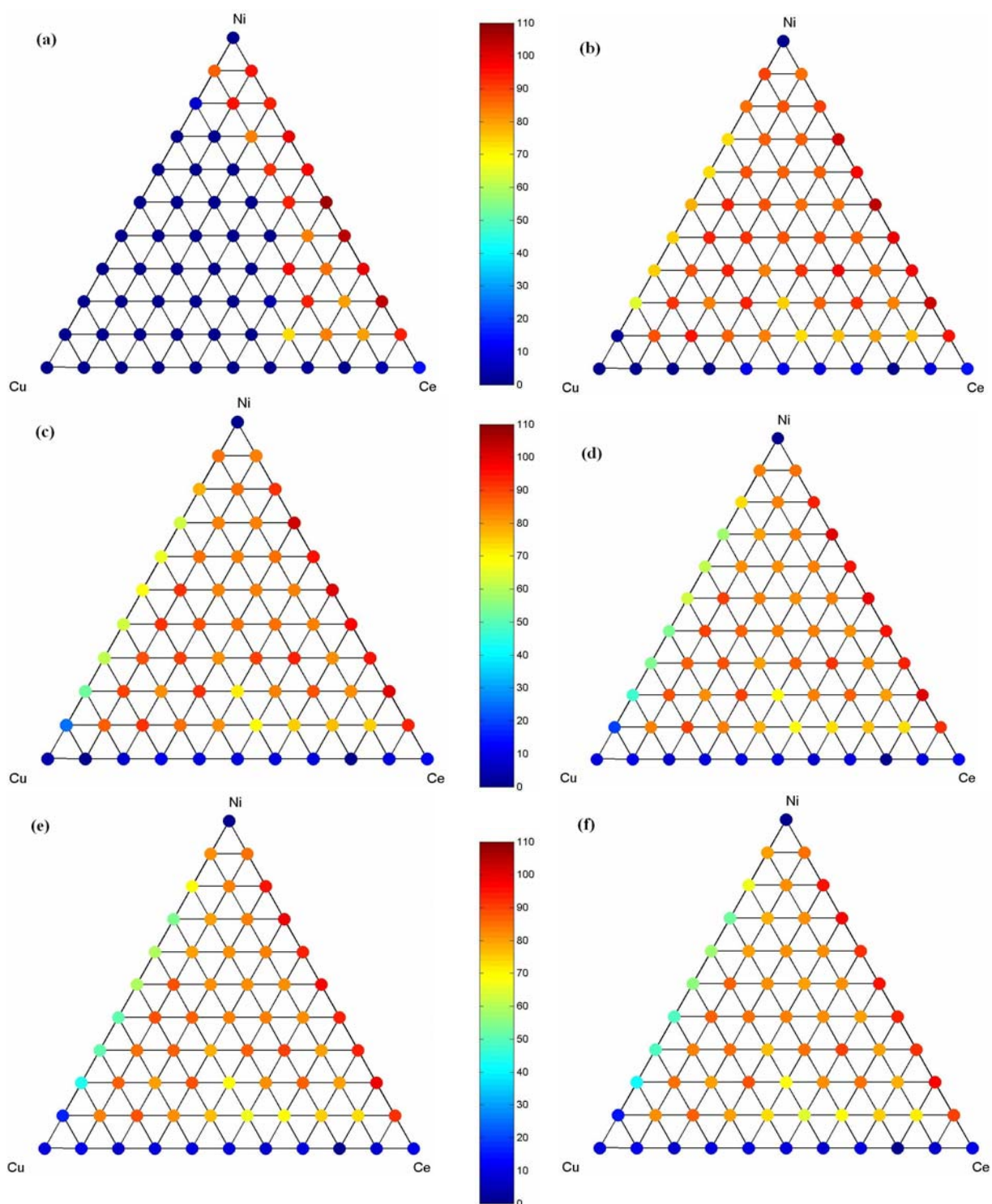


Figure 35. Relative catalytic activity (%) of the ternary composition $\text{Ni}_x\text{Cu}_y\text{Ce}_z$ ($0 \leq x, y, z \leq 100$, 10 mol% increment) library relative to the reference catalyst $\text{Rh}_1\text{Zr}_{20}\text{Al}_{79}$ at (a) 1st, (b) 2nd, (c) 3rd, (d) 4th, (e) 5th, and (f) 6th measurements in high-throughput tests during 820 s. Operating conditions: $T = 600$ °C; $P = 1$ bar; total flow: 10 ml min^{-1} ($\text{CH}_4/\text{CO}_2 = 1.12$). The color corresponds to the measured relative activity.

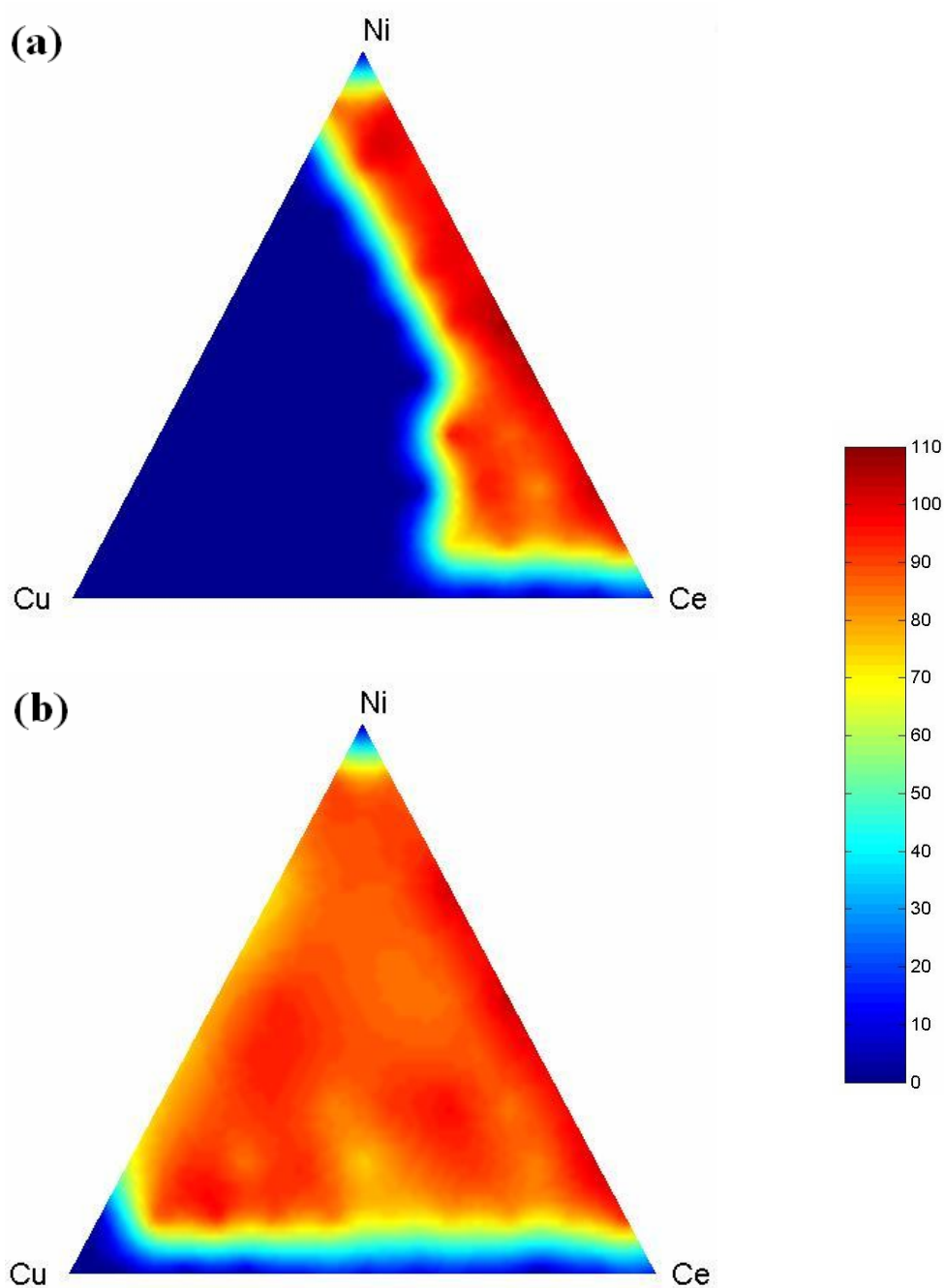


Figure 36. Approximated relative activity using the Kriging approach of the ternary composition $N_xCu_yCe_z$ ($0 \leq x, y, z \leq 100$, 10 mol% increment) library relative to the reference catalyst $Rh_1Zr_{20}Al_{79}$ in high-throughput tests during 820 s at (a) first and (b) second measurements. Operating conditions: $T = 600$ °C; $P = 1$ bar; total flow: 10 ml min^{-1} ($CH_4/CO_2 = 1.12$). The color corresponds to the estimated relative activity.

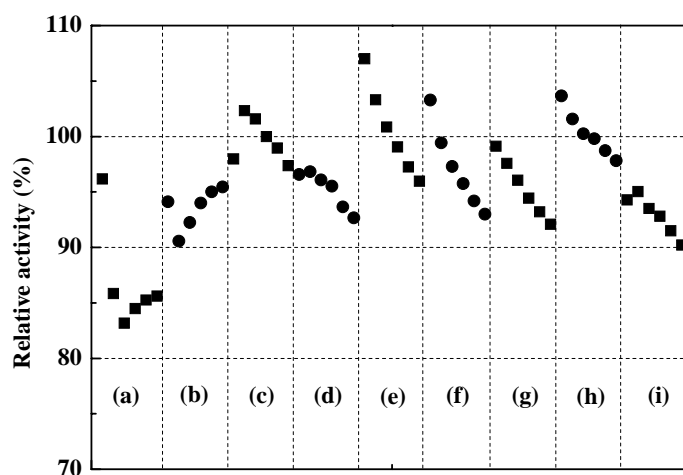


Figure 37. Time dependence of the catalytic activity (%) of the $\text{Ni}_x\text{Ce}_{100-x}$ ($10 \leq x \leq 90$, 10 mol% increment) mixed oxides relative to the reference catalyst $\text{Rh}_1\text{Zr}_{20}\text{Al}_{79}$ in high-throughput tests during 820 s: $x =$ (a) 90, (b) 80, (c) 70, (d) 60, (e) 50, (f) 40, (g) 30, (h) 20, (i) 10. Operating conditions: $T = 600\text{ }^\circ\text{C}$; $P = 1\text{ bar}$; total flow: 10 ml min^{-1} ($\text{CH}_4/\text{CO}_2 = 1.12$).

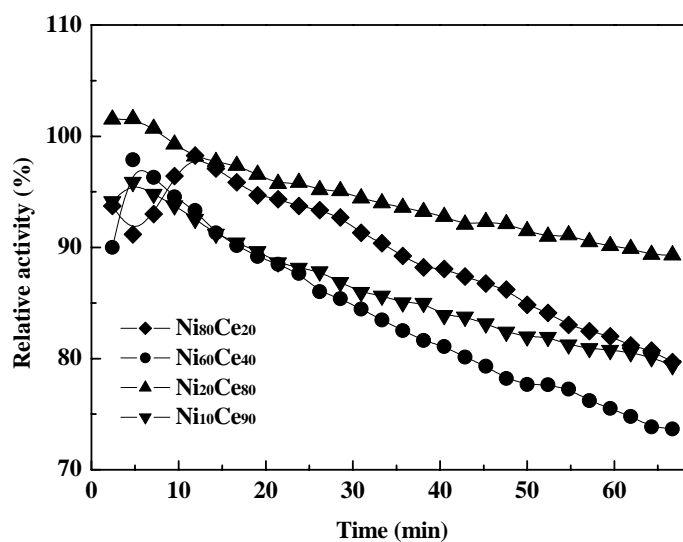


Figure 38. Time dependence of the catalytic activity (%) of the $\text{Ni}_x\text{Ce}_{100-x}$ ($x = 10, 20, 60, 80$) mixed oxides relative to the reference catalyst $\text{Rh}_1\text{Zr}_{20}\text{Al}_{79}$ in high-throughput tests during 3850 s: (\blacklozenge) $\text{Ni}_{80}\text{Ce}_{20}$; (\bullet) $\text{Ni}_{60}\text{Ce}_{40}$; (\blacktriangle) $\text{Ni}_{20}\text{Ce}_{80}$; (\blacktriangledown) $\text{Ni}_{10}\text{Ce}_{90}$. Operating conditions: $T = 600\text{ }^\circ\text{C}$; $P = 1\text{ bar}$; total flow: 10 ml min^{-1} ($\text{CH}_4/\text{CO}_2 = 1.12$).

Therefore, our focus moved to finding the optimal composition of Ni-Ce binary mixed oxides with higher activity and stability. Figure 37 depicts the relative activities (%) of the $\text{Ni}_x\text{Ce}_{100-x}$ ($0 < x < 100$, 10 mol% increment) mixed oxides during 820 s with six GC runs. Among those samples, $\text{Ni}_{80}\text{Ce}_{20}$ in (b), $\text{Ni}_{60}\text{Ce}_{40}$ in (d), $\text{Ni}_{20}\text{Ce}_{80}$ in (h), and $\text{Ni}_{10}\text{Ce}_{90}$ in (i), were selected as hits for the subsequent stability tests due to the comparable activity and higher stability. The selected samples were retested for another 3850 s as shown in Figure 38. Among the four samples, $\text{Ni}_{20}\text{Ce}_{80}$ and $\text{Ni}_{10}\text{Ce}_{90}$ showed comparable activity and the best stability.

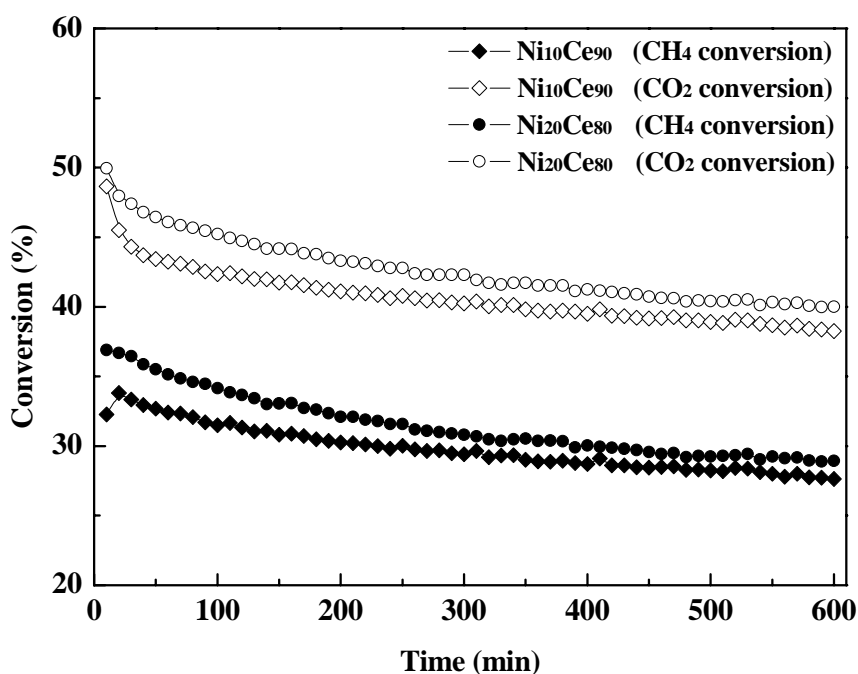


Figure 39. Time dependence of the catalytic activity of $\text{Ni}_{10}\text{Ce}_{90}$ and $\text{Ni}_{20}\text{Ce}_{80}$ in conventional tests: CH_4 conversion (\blacklozenge) and CO_2 conversion (\diamond) of $\text{Ni}_{10}\text{Ce}_{90}$; CH_4 conversion (\bullet) and CO_2 conversion (\circ) of $\text{Ni}_{20}\text{Ce}_{80}$. Operating conditions: $T = 600$ °C; $P = 1$ bar; total flow: 65 ml min^{-1} ($\text{CH}_4/\text{CO}_2/\text{Ar} = 16.9/15.1/68$); catalyst weight: 0.100 g.

The two promising catalysts were synthesized and examined in a conventional manner, and then characterized by TPO, XRD, and pulse experimentation. Conventional test results of

$\text{Ni}_{20}\text{Ce}_{80}$ and $\text{Ni}_{10}\text{Ce}_{90}$ during 600 min of reaction time are shown in Figure 39. The results of the conventional study within 60 min of reaction time are in accordance with those of the high-throughput screening for 3850 s. Both catalysts demonstrated a high initial activity with no prereduction, and $\text{Ni}_{20}\text{Ce}_{80}$ has a higher activity than $\text{Ni}_{10}\text{Ce}_{90}$ supporting Ni-Ce interface as active site. The good agreement between the combinatorial results and the results obtained under conventional reaction conditions confirms that the development of catalysts for CO_2 reforming of methane can be carried out reliably using our simple high-throughput method. Table 7 summarizes the physical properties and results of conventional testing and TGA of both catalysts. On BET measurements, the surface area of $\text{Ni}_{20}\text{Ce}_{80}$ was slightly higher than that of $\text{Ni}_{10}\text{Ce}_{90}$. Similar stability was identified for both catalysts from the similar deactivation rate while a slightly higher tendency towards coking of $\text{Ni}_{20}\text{Ce}_{80}$ was demonstrated in the TPO study of the used catalysts. The d-TGA profiles of the catalysts are shown in Figure 40.

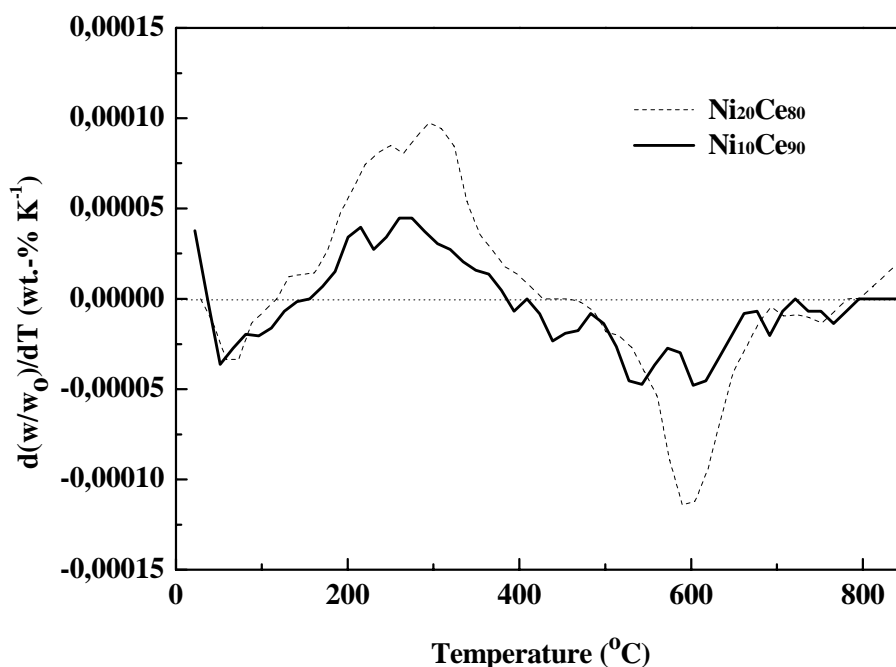


Figure 40. d-TGA profile of used $\text{Ni}_{10}\text{Ce}_{90}$ (—) and used $\text{Ni}_{20}\text{Ce}_{80}$ (-----) after 600 min reaction time. Operating conditions: catalyst weight: ≈ 0.050 g; T increasing rate: $15\text{ }^\circ\text{C min}^{-1}$; air total flow: 15 ml min^{-1} .

Table 7. Physical property, TGA and results of conventional tests of selected catalysts

Catalyst	$S_{\text{BET}}^{\text{a}}$ ($\text{m}^2 \text{g}^{-1}$)	Conventional testing ^b		TGA ^c	XRD
		Max. relative activity (%)	Deactivation rate (h^{-1})	coke ($\text{g}_\text{C} \text{g}_{\text{cat}}^{-1}$) ($\text{wt}\% \text{h}^{-1}$)	Ceria lattice parameter α (\AA)
$\text{Ni}_{10}\text{Ce}_{90}$	36.9	100.00	0.0181	0.08	5.4124(3)
$\text{Ni}_{20}\text{Ce}_{80}$	38.8	106.49	0.0181	0.11	5.411(1)
$\text{Zr}_5\text{Ni}_{10}\text{Ce}_{85}$	-	92.25	0.0207	0.15	5.3965(4)
$\text{Zr}_{15}\text{Ni}_{10}\text{Ce}_{75}$	39.2	106.29	0.0134	0.09	5.369(1)
$\text{Zr}_{45}\text{Ni}_{10}\text{Ce}_{45}$	-	45.03	0.0058	0.01	5.2583(3)
$\text{Zr}_{75}\text{Ni}_{10}\text{Ce}_{45}$	-	79.15	0.0387	0.01	5.1281(7)

^a Measured after calcination in air at 700 °C for 2h.

^b Operating conditions: T = 600 °C; P = 1 bar; total flow: 65 ml min^{-1} ($\text{CH}_4/\text{CO}_2/\text{Ar} = 16.9/15.1/68$); catalyst weight: 0.100 g; Time-on-stream: 10 h.

^c Operating conditions: catalyst weight: ≈ 0.050 g; T increasing rate: 15 °C min^{-1} ; air total flow: 15 ml min^{-1} .

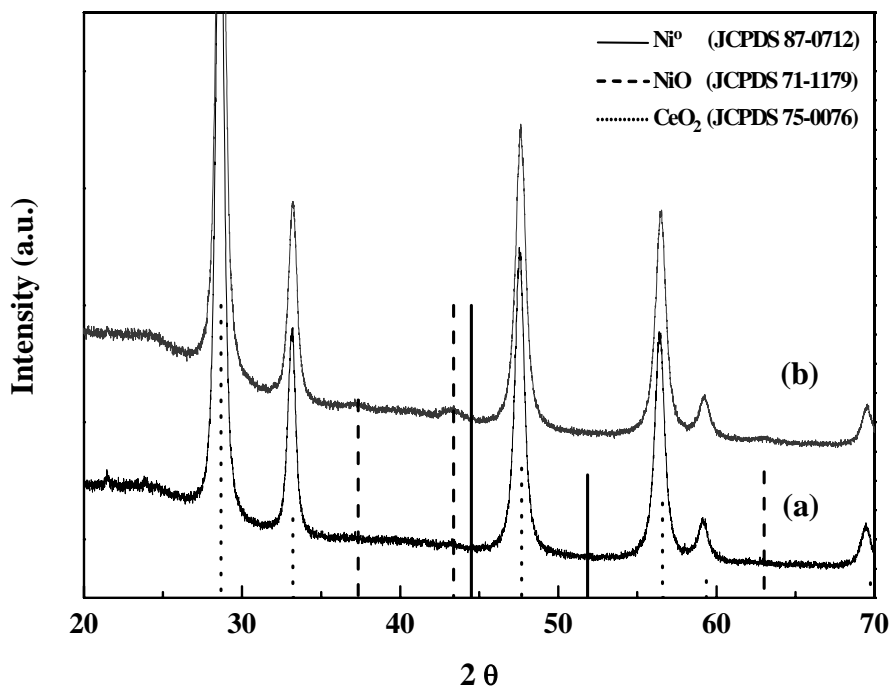


Figure 41. XRD patterns of the as prepared (a) $\text{Ni}_{10}\text{Ce}_{90}$ and (b) $\text{Ni}_{20}\text{Ce}_{80}$.

The XRD patterns of the as prepared $\text{Ni}_{10}\text{Ce}_{90}$ and $\text{Ni}_{20}\text{Ce}_{80}$ are shown in Figure 41. Both patterns are dominated by the diffraction peaks of the ceria substrate, a fluorite structure. At higher Ni content, the reflections of oxidized nickel (I_{100} at $2\theta=43.4^\circ$) are slightly increased. However, these peaks on the catalysts are very weak, together with the line broadening indicating the presence of very small particles. The small metal particles and their high dispersion of these catalysts are attributed to an intrinsic result of the acid catalyzed sol-gel preparation, well-known to provide atomically dispersed mixed oxides [162,163]. The ceria lattice parameters obtained from the XRD reflections of the as prepared $\text{Ni}_{10}\text{Ce}_{90}$ and $\text{Ni}_{20}\text{Ce}_{80}$ are shown in Table 7. As shown in Figure 42, the linear decrease of the CeO_2 lattice parameters was identified as increasing of Ni content for the pure CeO_2 ($a=5.4135(1)$ Å), as prepared $\text{Ni}_{10}\text{Ce}_{90}$ ($a=5.4124(3)$ Å), and $\text{Ni}_{20}\text{Ce}_{80}$ ($a=5.411(1)$ Å), which follows Vegard's law. This probably suggests an oxide solid solution formed in Ni-Ce mixed oxide system with incorporation of some Ni^{2+} ions into the ceria lattice, in agreement with former investigations [164,165]. The formation of the solid solution also seems due to the atomic dispersion of metal cations in the beginning of the acid catalyzed sol-gel method. The size of nickel particles could not be determined with acceptable significance because of the low intensity-to-noise ratio of the corresponding reflections.

The products from consecutive 25 CH_4 pulses on 100 mg $\text{Ni}_{20}\text{Ce}_{80}$ at 600 °C are depicted in Figure 43. When the first 14 CH_4 pulses were introduced to $\text{Ni}_{20}\text{Ce}_{80}$, H_2O and CO_2 were overwhelming products. In the case of $\text{Ni}_{10}\text{Ce}_{90}$, H_2O and CO_2 were main products during the first 8 CH_4 pulses (see panel A of Figure 32a). The total amount of oxygen consumption for the complete oxidation of methane was 15.5×10^{-5} mol on $\text{Ni}_{20}\text{Ce}_{80}$. Comparing the sum amount of oxygen consumption for the complete oxidation of methane between $\text{Ni}_{10}\text{Ce}_{90}$ (6.5×10^{-5} mol) and $\text{Ni}_{20}\text{Ce}_{80}$ (15.5×10^{-5} mol), the higher Ni content led the bigger amount of oxygen consumption for the complete oxidation of methane although the amount of oxygen consumption was not exact correlated with the amount of Ni probably since the dispersion of

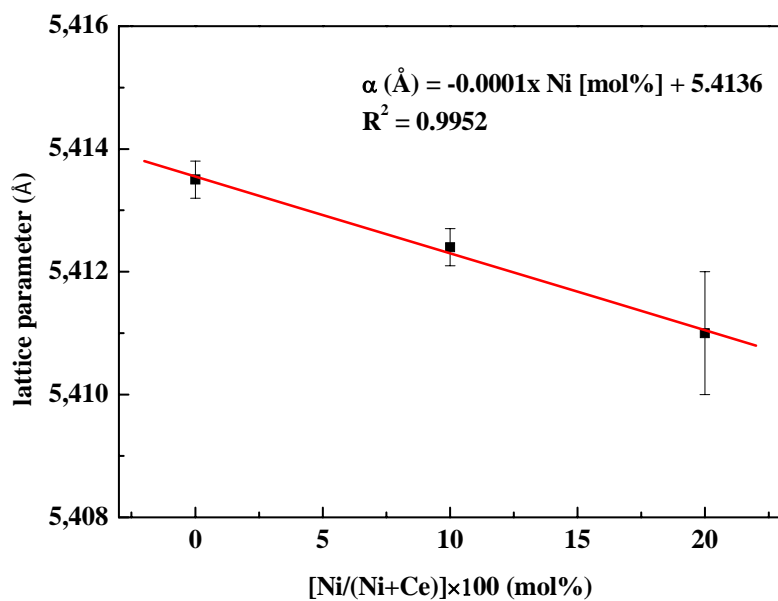


Figure 42. Relation between the composition and lattice parameter in $\text{Ni}_x\text{Ce}_{100-x}$ ($x = 0, 10, 20$).

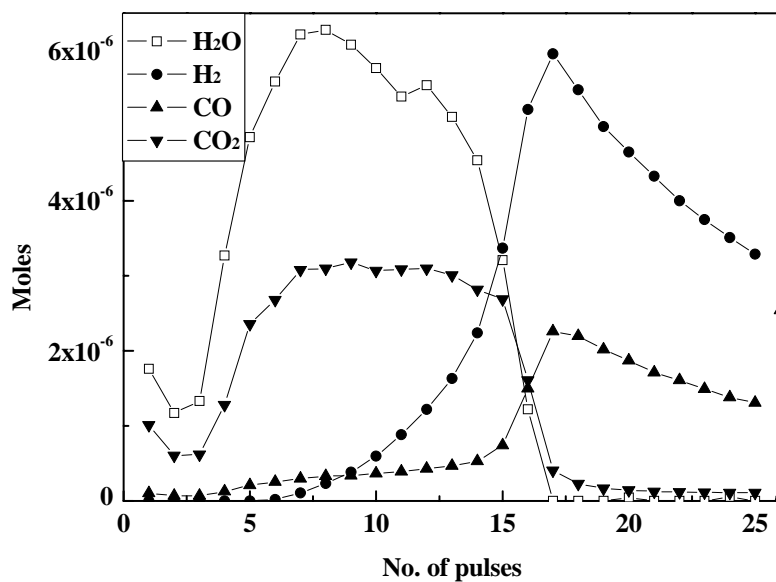


Figure 43. The amount of products from 25 consecutive pulses of CH_4 over 100 mg $\text{Ni}_{20}\text{Ce}_{80}$. The amount of H_2O is determined indirectly by $[(\text{the amount of } \text{CH}_4 \text{ consumed}) - 0.5 * (\text{the amount of } \text{H}_2 \text{ produced})] * 2$. Operating conditions: $T = 600 \text{ }^\circ\text{C}$; $P = 1 \text{ bar}$; Ar flow: 30 ml min^{-1} ; pulse volume: $100 \text{ } \mu\text{l}$ ($4.07 \text{ } \mu\text{mol}$).

nickel species may not be identical. This observation supports the Ni-Ce interface is the active site for the complete oxidation of methane, which proposed in chapter 2.2.5. The maximum CH₄ conversion was detectable at pulse 14. After the pulse 15, the formation of H₂ and CO dominated clearly, but decreased continuously. Overall, Ni₂₀Ce₈₀ behaved analogously to the Ni₁₀Ce₉₀ catalyst confirming the initial observation.

2.3.2. Zr_xNi₁₀Ce_{90-x} mixed oxide

In chapter 2.1, Zr₁₅Ni₁₀Ce₇₅ was the most promising catalyst because of its high activity and low tendency towards coking despite its deactivation behaviour. The property of Zr₁₅Ni₁₀Ce₇₅ was investigated by pulse experiments. The products from consecutive 35 CH₄ pulses on 100 mg Zr₁₅Ni₁₀Ce₇₅ at 600 °C are depicted in Figure 44. When the first 20 CH₄ pulses were introduced to Zr₁₅Ni₁₀Ce₇₅, H₂O and CO₂ were main products although the first 12 CH₄ pulses allowed small amount of H₂O and CO₂. Comparing the pulse number on Zr₁₅Ni₁₀Ce₇₅ before reaching the maximum production point of H₂O and CO₂ with that on Ni₁₀Ce₉₀ and Ni₂₀Ce₈₀ during CH₄-pulsed experiment, a slow activation property of Zr₁₅Ni₁₀Ce₇₅ was recognized (compare Figure 44 with Figure 43 and panel A of Figure 32a). The relatively slow activation property of Zr₁₅Ni₁₀Ce₇₅ compared with Ni₁₀Ce₉₀ was already observed in its high-throughput testing during 800 s and 3500 s (see Figure 19 and 20). In the chapter 2.2.5, the interfacial oxygen in the Ni-Ce boundary was suggested as an active component for the complete oxidation of methane. Therefore, it is assumed that the 15mol% Zr doping retards the reaction of the interfacial oxygen in the Ni-Ce boundary. After pulse 20, the formation of H₂ and CO dominated although considerable amounts of CO₂ are still formed. The CO product increased continuously in this range and the H₂ production decreased much more slowly compared with Ni₁₀Ce₉₀ and Ni₂₀Ce₈₀.

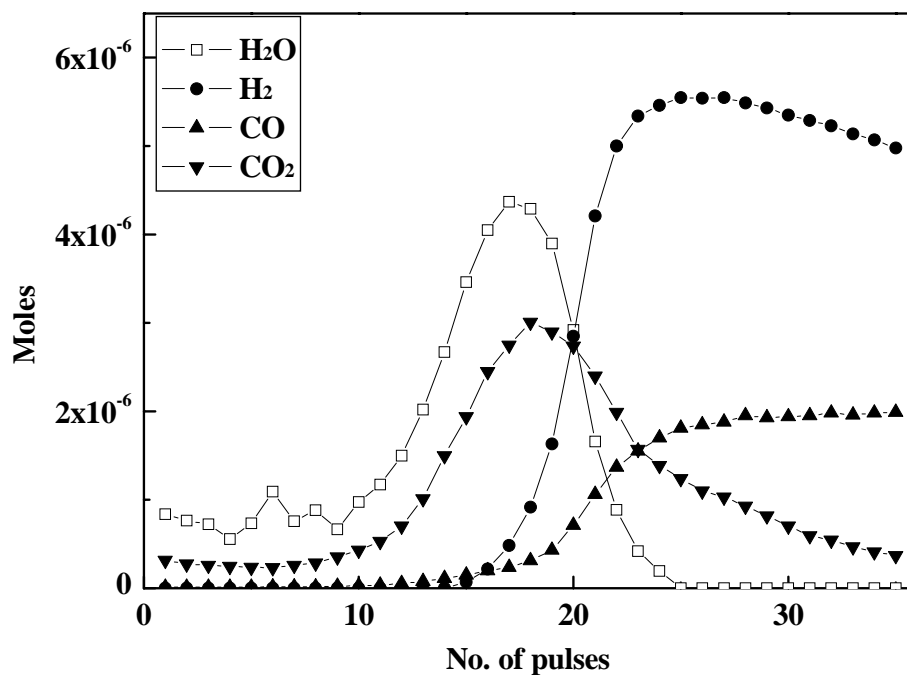


Figure 44. The amount of products from 35 consecutive pulses of CH₄ over 100 mg Zr₁₅Ni₁₀Ce₇₅. The amount of H₂O is determined indirectly by [(the amount of CH₄ consumed)-0.5*(the amount of H₂ produced)]*2. Operating conditions: T = 600 °C; P = 1 bar; Ar flow: 30 ml min⁻¹; pulse volume: 100 μl

Zr_xNi₁₀Ce_{90-x} (x = 5, 15, 45, 75 mol%) catalysts were synthesized and examined in a conventional way in order to check the long-term activity and stability dependence on the amount of Zr. Table 7 summarizes the physical properties and results of conventional testing and TGA of these catalysts in comparison with Ni₁₀Ce₉₀ (see page 82). Figure 46 shows the conventional test results of these catalysts, and Figure 45 reveals the TPO study of the used catalysts in comparison with Ni₁₀Ce₉₀. The results of the conventional study are in accordance with those of the high-throughput screening for 800 s and 3500 s within the same time range (compare Figure 46 with Figure 19 and 20). The coking resistivity was improved with increasing Zr amount. Considering activity, stability, and coking resistance, 5 % Zr leads to a

negative dopant effects while 15 % Zr dopant sample shows higher activity and stability in comparison with $\text{Ni}_{10}\text{Ce}_{90}$. When the molar amount of Zr and Ce is same, an interesting behaviour was observed. The $\text{Zr}_{45}\text{Ni}_{10}\text{Ce}_{45}$ shows best stability and low tendency towards carbon deposition. However, in $\text{Zr}_{45}\text{Ni}_{10}\text{Ce}_{45}$ activity is delayed until after almost 100 min, and catalytic activity stabilized at quite low conversions only after about 250 min (long induction period). $\text{Zr}_{75}\text{Ni}_{10}\text{Ce}_{15}$ leads to a negative dopant effects on its activity and stability.

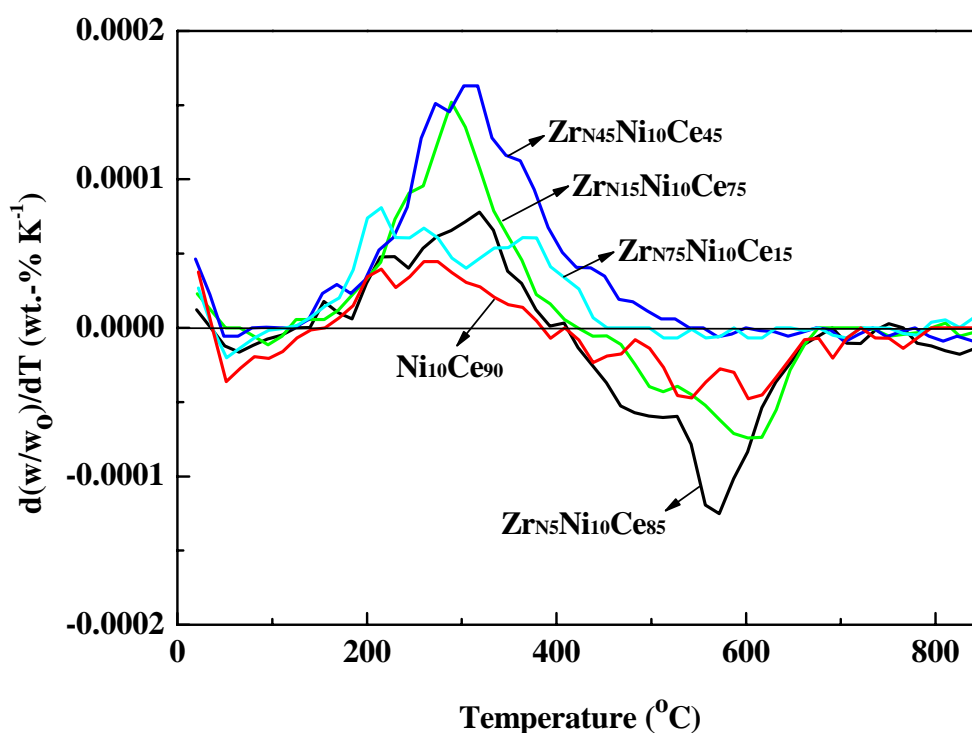


Figure 45. d-TGA profile of used $\text{Zr}_x\text{Ni}_{10}\text{Ce}_{90-x}$ ($x = 5, 15, 45,$ and 75) in comparison with the reference $\text{Ni}_{10}\text{Ce}_{90}$ after 600 min reaction time. Operating conditions: catalyst weight: ≈ 0.050 g; T increasing rate: $15^\circ\text{C min}^{-1}$; air total flow: 15 ml min^{-1} .

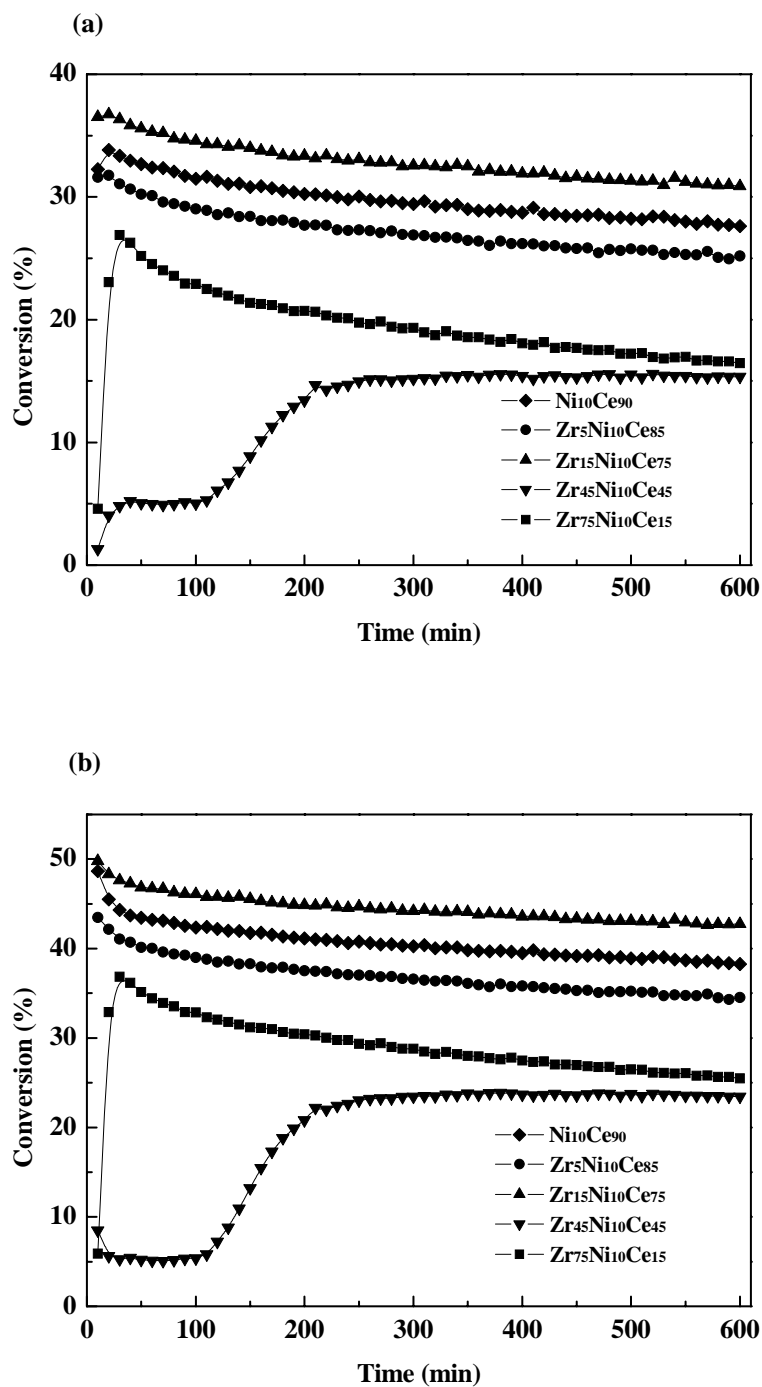


Figure 46. Time dependence of (a) CH₄ conversion and (b) CO₂ conversion of Zr_{N_x}Ni₁₀Ce_{90-x} (x = 5, 15, 45, 75) relative to Ni₁₀Ce₉₀ in conventional tests: (◆) Ni₁₀Ce₉₀; (●) Zr₅Ni₁₀Ce₈₅; (▲) Zr₁₅Ni₁₀Ce₇₅; (▼) Zr₄₅Ni₁₀Ce₄₅; (■) Zr₇₅Ni₁₀Ce₁₅. Operating conditions: T = 600 °C; P = 1 bar; total flow: 65 ml min⁻¹ (CH₄/CO₂/Ar = 16.9/15.1/68); catalyst weight: 0.100 g.

The XRD pattern of the as prepared $Zr_xNi_{10}Ce_{90-x}$ ($x = 0, 5, 15, 45,$ and 75) are shown in Figure 47. The patterns of $Ni_{10}Ce_{90}$ are dominated by the diffraction peaks of the ceria substrate, a fluorite structure. The powders showed the same crystal structure after Zr addition. However, the diffraction angle of their peaks gradually shifted towards higher values with increasing Zr amount. The lattice parameters of each sample are shown in Table 7, and as a function of Zr amount in Figure 48. As the amount of Zr, which has a smaller ionic diameter than Ce increases, the lattice parameter of the samples decreases linearly. The dependence of the lattice parameter (\AA) on the Zr amount follows Vegard's law. Therefore, it is assumed that the CeO_2 and ZrO_2 form a solid solution.

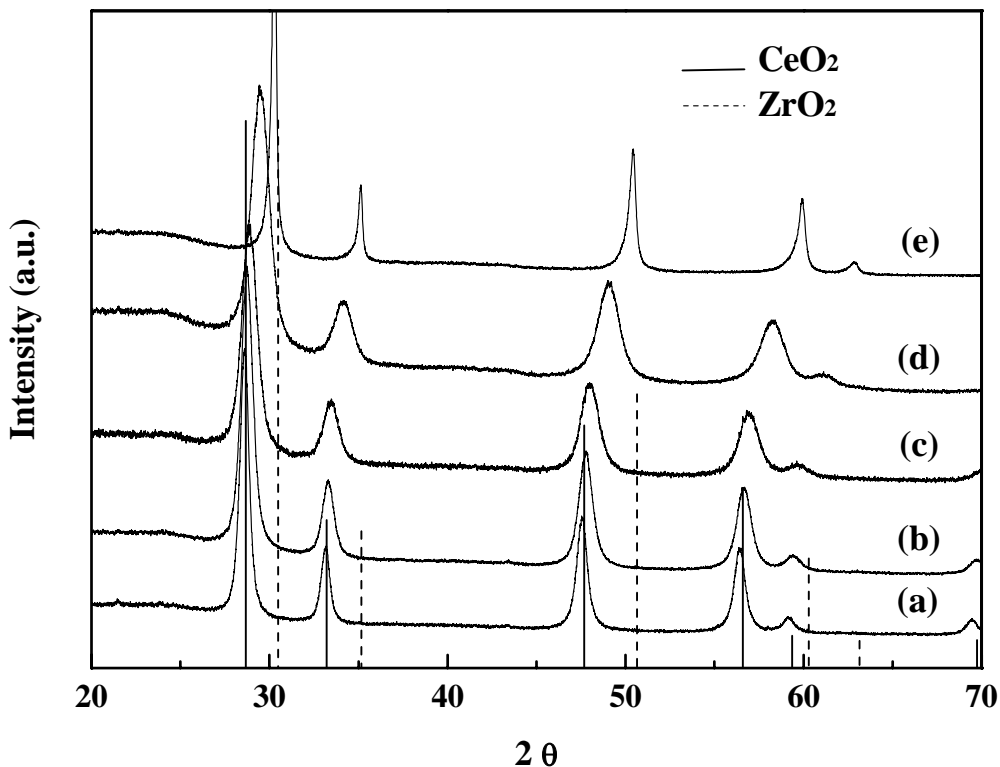


Figure 47. XRD patterns of the as prepared $Zr_xNi_{10}Ce_{90-x}$; $x =$ (a) 0, (b) 5, (c) 15, (d) 45, (e) 75.

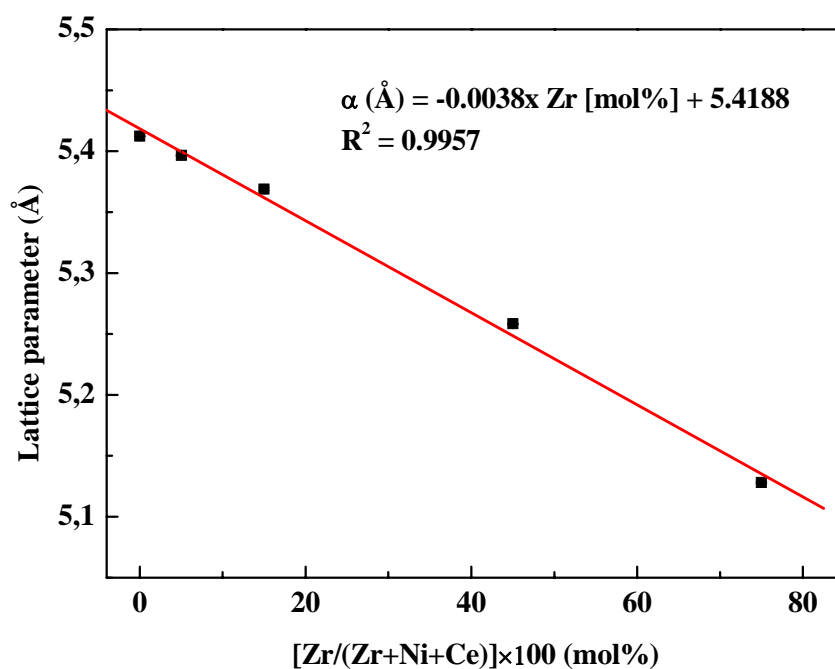


Figure 48. Relation between the composition and lattice parameter in $Zr_xNi_{10}Ce_{90-x}$.

Ceria is commonly used as the primary component of oxygen storage and release capacity materials (OSC materials). Thus, a method that has been proposed and implemented as a purpose for improving the oxygen storage/release capacity (OSC) involves production of solid solutions by introducing an element having a smaller ionic diameter than Ce ions into the ceria [175,176]. By doing so, the space surrounding the oxygen is increased, thereby facilitating reversible storage and release of oxygen in the matrix [177]. In Figure 44, the amount of CO and H₂ production on Zr₁₅Ni₁₀Ce₇₅ decreased much more slowly to be compared with Ni₁₀Ce₉₀. It is probably due to the improvement of OSC by formation of CeO₂-ZrO₂ solid solution, which is confirmed in Figure 47 and 48. Graziani and co-workers reported that incorporation of ZrO₂ into the CeO₂ lattice strongly promotes the reducibility of metal-loaded mixed oxides, and in the Rh-loaded Ce_{1-x}Zr_xO₂ (x = 0.1–0.9, 0.1 mol% increment), the addition of an increasing amount of ZrO₂ lowers the temperature of the reduction, reaching a minimum for the cubic

Rh/Ce_{0.5}Zr_{0.5}O₂, ca. 500 K lower than the temperature of reduction of bulk Rh/CeO₂ [175,176]. Similarly, Resasco and co-workers reported that in the Pt-loaded Ce_{1-x}Zr_xO₂ (x = 0.25, 0.5, 0.75), the reducibility of the support correlated with its oxygen exchange capacity, and has a maximum at the composition Ce_{0.5}Zr_{0.5}O₂. [178]. Therefore, the highest OSC of Zr₄₅Ni₁₀Ce₄₅ presumably leads the catalyst to best stability and low tendency towards carbon deposition.

2.4. Combinatorial discovery of new catalysts for the selective oxidation of propane to acrylic acid

2.4.1. High-throughput screening (generation 1)

This study was performed in collaboration with K.S. Oh, visiting scientist from Korea. In the present chapter, discovery of new catalytic mixed oxides and optimization of the Mo-V-Te-Nb mixed oxide system for the selective oxidation of propane is investigated using a high-throughput MS screening setup. Conventional preparative methods such as slurry and hydrothermal methods are not suitable for high-throughput screening due to a long period in refluxing at preparation step. Thus, in this study the highly tolerant and simple synthesis recipe based on sol-gel procedures [89,179,180] was used for high-throughput preparation of mixed oxides. The procedure of sol-gel preparation method 1 (see chapter 3.1) was used for the syntheses of ternary and quaternary mixed oxides. Typically, 0.5 M metal precursor solutions except for molybdenum (0.1 M) and tungsten (0.226 M) were prepared by metal alkoxides (vanadium (V) triisopropoxide, iron (III) ethoxide, niobium (V) ethoxide, tantalum (V) ethoxide, manganese (II) propionate, tungsten (VI) isopropoxide in *i*-propanol, and bismuth (III) 2-ethylhexanoate, molybdenum (V) hexanoate in *n*-propanol), nitrate (chromium (III) nitrate in *i*-propanol) or anhydrous metal chlorides (antimony (V) chloride, tellurium (IV) chloride, and niobium (V) chloride in *i*-propanol). The molar ratio of metal:water:acid (propionic acid):complexing agent (4-hydroxy-4-methyl-pentanone):alcohol (isopropanol) was 100:100:6:300:6500. The resulting gels were dried at room temperature for 5 days and calcined in an oven at 65 °C for 5 h and at 250 °C for 5 h. The prepared library was calcined again at 600 °C for 2 h in an oven with inert condition. $\text{Mo}_{60}\text{V}_{20}\text{Te}_{13}\text{Nb}_7$ by slurry method was prepared by

K.S. Oh in a conventional manner, and used as reference catalyst. Some wells were left empty for background, and at least one well was filled with a reference catalyst. The activity of each well was obtained from the amount of acrolein or acrylic acid produced on the catalyst, and represented relative to the activity of the reference catalyst. Therefore, the relative activity (%) of each sample was defined as [(the amount of acrolein or acrylic acid produced on a sample)/(the amount of acrolein or acrylic acid produced on the reference catalyst) × 100].

The catalyst libraries were screened in a simple high-throughput reactor system at 420 °C connected to a QMS for product analysis with aid of R. Richter and H. Hölzén. A liquid mass flow controller (MFC) connected to an autoclave was used to inject desirable amount of water. The injected 10 vol% water was well-mixed with reactant gas (8.7 vol% C₃H₈, 4.9 vol% O₂, and Ar balance with total flow rate of 5 ml min⁻¹) in a micro mixer from IMM. In addition, the whole educt capillary was heated with thin heating elements controlled by a thin thermocouple to prevent liquid condensation. The products were monitored on-line by a QMS. The argon intensity of each signal was chosen for internal standardization as representative within the chronological progress recording the detection sensitivity over the whole experiment. The mass spectrometer is running continuously and assignments of mass spectral data to each catalyst position are made by comparison of the time tables of the HTE saved by the program TestRig [158] and the MS. These files can be analyzed computationally by using MS Express written in our group [181].

In a first generation, 11 elements were selected (Mo, V, Te, Ta, Nb, Sb, W, Cr, Bi, Mn, and Fe). The selection was based on the interesting dehydrogenation and/or oxidation properties of the associated oxides reported in the literature. The prepared library contained only ternary mixed oxides with a molar composition of (33, 33, 33). After the library composed of ternary mixed oxide was calcined and activated, the 207 member library plate was placed into a reactor and heated up to 420 °C. The highest activity for acrolein formation is found at Mo₃₃Cr₃₃Te₃₃ (relative activity of 508 %), V₃₃Cr₃₃Sb₃₃ (487 %), V₃₃Sb₃₃Bi₃₃ (296 %), and Mo₃₃V₃₃Cr₃₃

(234 %). Especially, the $\text{Mo}_{33}\text{Cr}_{33}\text{Te}_{33}$ and $\text{V}_{33}\text{Cr}_{33}\text{Sb}_{33}$ catalysts show high acrolein formation and relatively low CO_2 formation. It is noteworthy that Cr-containing catalysts, including Mo and V, show high acrolein formation among the screened catalysts. On the other hand, Cr-containing catalysts, not including Mo and V, produced more CO_2 than others. About 25 % of the samples from the library produced more CO_2 than the reference catalysts. The formation of acrylic acid was negligible for all the samples except for reference catalysts prepared by the slurry method.

2.4.2. High-throughput screening (generation 2)

Based on the results of generation 1, MoCrTe, VCrSb, and MoVCr were selected as potential catalysts for propane oxidation to acrylic acid. A library with the composition spread of the candidates was prepared, where the three elements were allowed to vary between 0 and 100 mol% in steps of 10 mol%. Figure 49a illustrates the performance of the ternary mixed oxides of V-Cr-Sb. The highest activity for acrolein formation is found at $\text{V}_{10-40}\text{Cr}_{30-40}\text{Sb}_{20-60}$. The most active catalyst is $\text{V}_{20}\text{Cr}_{20}\text{Sb}_{60}$ that shows the acrolein formation of 250 % to be compared with the reference catalyst ($\text{Mo}_{60}\text{V}_{20}\text{Te}_{13}\text{Nb}_7$ prepared by the slurry method). The CO_2 formation is increased in the region $\text{V}_{0-10}\text{Cr}_{60-90}\text{Sb}_{10-30}$, which indicates that the total oxidation occurred in this region. Figure 49b shows the performance of the ternary mixed oxides of Mo-Cr-Te. The highest activity for acrolein formation is observed at $\text{Mo}_{30-40}\text{Cr}_{40-50}\text{Te}_{10-20}$. The most active catalyst in this region is $\text{Mo}_{30}\text{Cr}_{50}\text{Te}_{20}$, which shows the relative activity of 480 %. Total oxidation mainly occurs at the chromium rich region. The relative performance of the ternary mixed oxides of Mo-V-Cr is illustrated in Figure 49c. The highest activity for acrolein formation is found in the region with $\text{Mo}_{10-40}\text{V}_{0-30}\text{Cr}_{50-70}$. The most active catalyst for aldehyde formation is $\text{Mo}_{30}\text{Cr}_{70}$ which shows the relative activity of 250 %. The CO_2 formation is observed only in the region of chromium rich region.

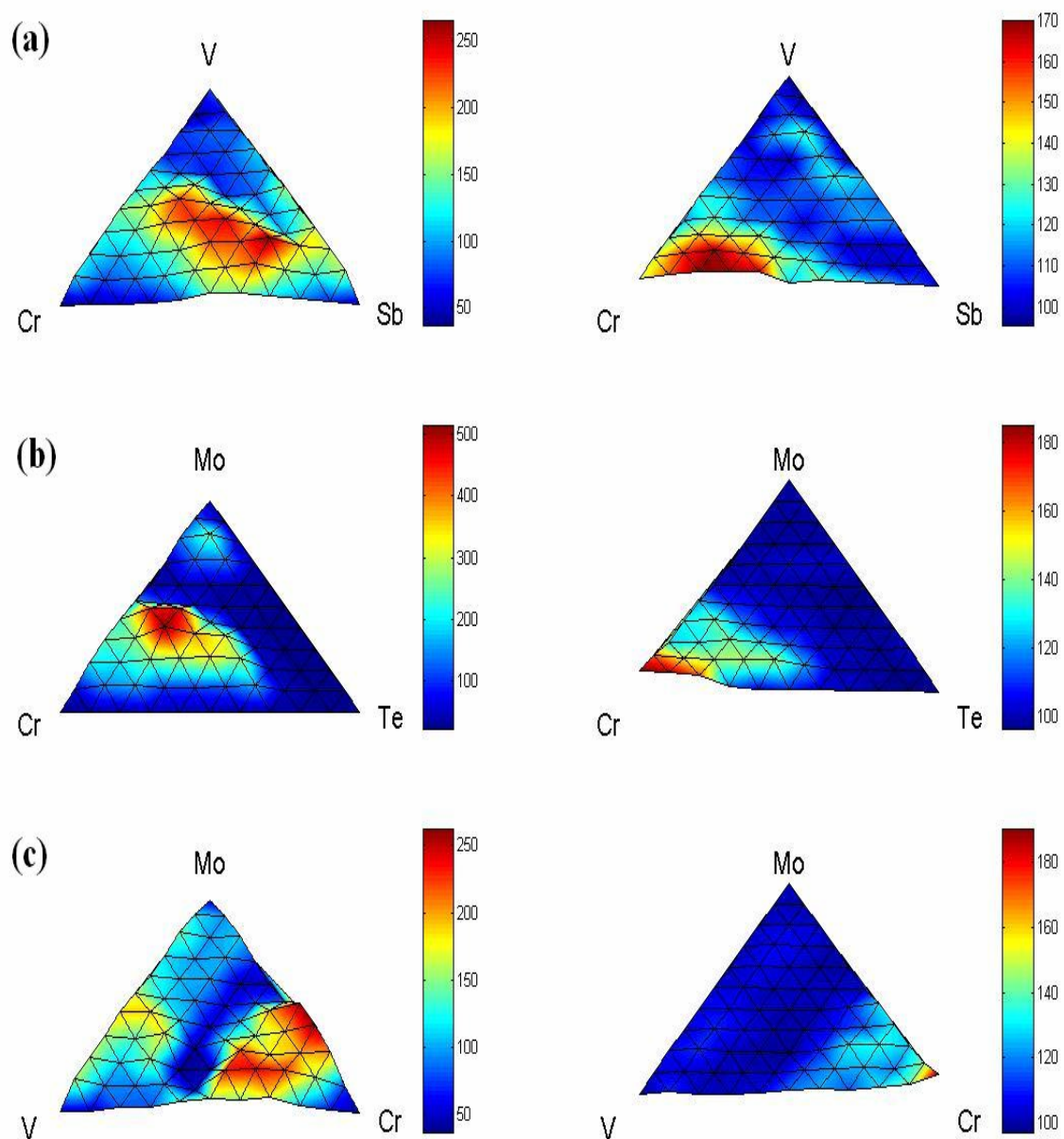


Figure 49. Relative performance of 66 member (a) V-Cr-Sb, (b) Mo-Cr-Te, and (c) Mo-V-Cr oxides: acrolein formation is presented on the left side and CO₂ formation is on the right side of the figures.

From the above results, catalytic property of VCrSb, MoCrTe, MoVCr oxides systems shows high performance for acrolein formation and relatively low CO₂ formation with the catalyst of active for acrolein formation. Cr containing mixed oxides can be potential candidate for acrolein production. However, for all the catalysts, the formation of acrylic acid was negligible.

2.4.3. High-throughput screening (optimization of Mo-V-Te-Nb)

It is well known that quaternary mixed oxides composed of Mo-V-Te-Nb is the most active composition for acrylic acid formation. Based on this result, the quaternary mixed oxide catalyst library was prepared. In the library, Mo was allowed to vary between 50 ~ 100 mol%, Nb was changed between 0 ~ 20 mol%, V and Te was 0 ~ 30 mol%, in steps of 5 mol%, resulting in 190 samples. The highest activity for acrolein formation is found at Mo₆₀₋₈₀V₅₋₂₅Te₅₋₂₀Nb₀₋₁₀. The most active catalyst for acrolein formation is Mo₇₀V₂₅Te₀Nb₅, which shows 125 % of the acrolein formation compared the reference Mo₆₀V₂₀Te₁₃Nb₇. CO₂ production was low for the most active compositions towards aldehyde formation. However, acrylic acid formation was still negligible, maybe due to the influences of synthesis method between sol-gel and slurry method. Thus, this study is continued by K.S. Oh in Korea.

3. Experimental

3.1. High-throughput syntheses of catalyst libraries

Most materials were obtained from commercial sources and used without further purification. A list of the metal complexes and their solvent used as matrix and dopant are described in Table 8 and 9. In the study of the CO₂ reforming of methane, alcoholic solutions of metal nitrates (Ag, Al_N, Ba, Ca, Cd, Ce, Co, Cr, Cs, Cu, Dy, Er, Eu, Fe, Ga, Gd, Ho, In, K, La, Li, Lu, Mg, Mn, Na, Nd, Ni, Pb, Pr, Sc, Sm, Sr, Tb, Tm, Y, and Yb), alkoxides (Al_A, Bi, Ge, Mo, Nb, Pd, Rb, Si, Sn, Ta, Ti, V, W, and Zr_A), chlorides (Hf, Ir, Re, Rh, Ru, Sb, Sn, and Te), bromides (Au and Pt), dinitrate oxide (Zr_N), acid (B), and oxide (Se) were used as standard dopant precursors. Subscripts were used to distinguish dopant elements based on the different kinds of precursors (i.e., “N” for metal nitrate and “A” for metal alkoxide). In the procedure, 1 M matrix and 0.1 M dopant stock solutions were prepared. In the study of the selective oxidation of propane, 0.5 M metal precursor solutions except for molybdenum (0.1 M) and tungsten (0.226 M) were prepared by metal alkoxides (vanadium(V) triisopropoxide, iron(III) ethoxide, niobium(V) ethoxide, tantalum(V) ethoxide, manganese(II) propionate, tungsten(VI) isopropoxide in *i*-propanol, and bismuth(III) 2-ethylhexanoate, molybdenum(V) hexanoate in *n*-propanol), nitrate (chromium(III) nitrate in *i*-propanol) or anhydrous metal chlorides (antimony(V) chloride, tellurium(IV) chloride, and niobium(V) chloride in *i*-propanol).

The automated synthesis of catalysts was carried out with a using a commercial pipetting robot (Lissy, Zinsser Analytic). In the procedure, matrix and dopant stock solutions were positioned in 10 ml vials and used to formulate the final reaction mixture by transferring the aliquots of each stock solution into 2-ml vials, positioned in racks of 50 vials.

Table 8. List of chemicals and their solvents used for matrix and dopant to prepare mixed oxides

Element	Chemical	Solvent ^a	Element	Chemical	Solvent
Ag	AgNO ₃	M	Mo	Mo[OCH(CH ₃) ₂] ₅	I
Al _N	Al(NO ₃) ₃ · 9 H ₂ O	I, M	Mo	Mo[CH ₃ (CH ₂) ₄ CO ₂] ₅	N
Al _A	Al[C ₂ H ₅ CH(CH ₃)O] ₃	I	Na	NaNO ₃	M
Au	AuBr ₃	M	Nb	Nb(OC ₂ H ₅) ₅	I, M
B	B(OH) ₃	I, M	Nb	NbCl ₅	I
Ba	BaCl ₂	M	Nd	Nd(NO ₃) ₃ · 6 H ₂ O	I, M
Bi	Bi[C ₄ H ₉ CH(C ₂ H ₅)COO] ₃	M	Ni	Ni(NO ₃) ₂ · 6 H ₂ O	I, M
Ca	Ca(NO ₃) ₂ · 4 H ₂ O	I, M	Ni	Ni propionate	M
Cd	Cd(NO ₃) ₂ · 4 H ₂ O	I, M	Pb	Pb(NO ₃) ₂	W
Ce	Ce(NO ₃) ₃ · 6 H ₂ O	I, M	Pd	Pd(CH ₃ CO ₂) ₂	M
Co	Co(NO ₃) ₂ · 6 H ₂ O	I, M	Pr	Pr(NO ₃) ₃ · 5 H ₂ O	I, M
Co	Co propionate	E	Pt	PtBr ₄	W
Cr	Cr(NO ₃) ₃ · 9 H ₂ O	I, M	Rb	Rb[CH ₃ COCHCOCH ₃]	M
Cs	CsCl	M	Re	ReCl ₅	M
Cu	Cu(NO ₃) ₂ · 3 H ₂ O	I, M	Rh	RhCl ₃ · 3 H ₂ O	W
Cu	Cu[(CH ₃) ₂ CHO] ₂	I	Ru	RuCl ₃	W
Dy	Dy(NO ₃) ₃ · 5 H ₂ O	I, M	Sb	SbCl ₃	M
Er	Er(NO ₃) ₃ · 5 H ₂ O	I, M	Sc	Sc(NO ₃) ₃ · 5 H ₂ O	I, M
Eu	Eu(NO ₃) ₃ · 6 H ₂ O	I, M	Se	SeO ₂	I, M
Fe	Fe(NO ₃) ₃ · 9 H ₂ O	M	Si	Si(OC ₂ H ₅) ₄	I, M
Fe	Fe(OCH ₂ CH ₃) ₃	I	Sm	Sm(NO ₃) ₃ · 6 H ₂ O	I, M
Ga	Ga(NO ₃) ₃ · xH ₂ O	M	Sn	SnCl ₂ · 2 H ₂ O	I, M
Gd	Gd(NO ₃) ₃ · 6H ₂ O	I, M	Sn	Sn[OCH(CH ₃) ₂] ₄	I
Ge	Ge[OCH(CH ₃) ₂] ₄	I, M	Sr	SrCl ₂	M
Hf	HfCl ₄	I, M	Ta	Ta(OC ₂ H ₅) ₅	I, M
Ho	Ho(NO ₃) ₃ · 5 H ₂ O	I, M	Tb	Tb(NO ₃) ₃ · x H ₂ O	I, M
In	In(NO ₃) ₃ · 5 H ₂ O	M	Te	TeCl ₄	I, M
Ir	IrCl ₃	W	Ti	Ti[OCH(CH ₃) ₂] ₄	I, M
K	KNO ₃	M	Tm	Tm(NO ₃) ₃ · 6 H ₂ O	I, M
La	La(NO ₃) ₃	I, M	V	V[CH ₃ COCHCOCH ₃] ₃	M
Li	LiNO ₃	I, M	W	W[OCH(CH ₃) ₂] ₆	M
Lu	Lu(NO ₃) ₃ · xH ₂ O	I, M	Y	Y(NO ₃) ₃ · 6 H ₂ O	I, M
Mg	Mg(NO ₃) ₂ · 6H ₂ O	I, M	Yb	Yb(NO ₃) ₃ · x H ₂ O	I, M
Mg	Mg propionate	M	Zn	Zn(NO ₃) ₂ · 4 H ₂ O	I, M
Mn	Mn(NO ₃) ₂ · 4H ₂ O	I, M	Zr _N	ZrO(NO ₃) ₂ · x H ₂ O	M
Mn	Mn propionate	M	Zr _A	Zr[O(CH ₂) ₂ CH ₃] ₄	N

^a I, M, E, N and W indicate isopropanol, methanol, ethanol, n-propanol and water, respectively.

Table 9. Elements used for matrix and dopant

Li													B		
Na	Mg												Al	Si	
K	Ca	Sc	Ti	V	Cr	Mn	Fe	Co	Ni	Cu	Zn	Ga	Ge		Se
Rb	Sr	Y	Zr	Nb	Mo		Ru	Rh	Pd	Ag	Cd	In	Sn	Sb	Te
Cs	Ba	Lu	Hf	Ta	W	Re		Ir	Pt	Au		Pb	Bi		
		La	Ce	Pr	Nd		Sm	Eu	Gd	Tb	Dy	Ho	Er	Tm	Yb

Three different kinds of modified acid catalyzed sol-gel procedures were applied to prepare libraries depending on the matrix metal precursor used (i.e., method 1 for alkoxide, method 2 for propionate, and method 3 for nitrate) as follows. The total molar amount of dopant and matrix was set as 200 μmol per sample.

Method 1. This method followed procedures similar to those described in detail previously [89,155,179]. Briefly, the molar ratio of dopant:matrix:water:acid (nitric acid for $\text{E}_x\text{Zr}_{20}\text{Al}_{80-x}$, acetic acid for M_3N_{97} , or propionic acid for the mixed oxides in the study of selective oxidation of propane):complexing agent (4-hydroxy-4-methyl-pentanone):alcohol (isopropanol) was $x:100-x:100:6:300:6500$. The preparation of $\text{Ni}_5\text{Zr}_{20}\text{Al}_{75}$, for example, was carried out by pipetting the following volumes of single solutions in the following sequence: complexing agent (74.1 μl , 600 μmol), 1 M $\text{Zr}[\text{O}(\text{CH}_2)_2\text{CH}_3]_4$ in isopropanol (40.0 μl , 40 μmol), 1 M $\text{Al}[\text{C}_2\text{H}_5\text{CH}(\text{CH}_3)\text{O}]_3$ in isopropanol (150.0 μl , 150 μmol), 0.1 M $\text{Ni}(\text{NO}_3)_2 \cdot 6 \text{H}_2\text{O}$ in isopropanol (100.0 μl , 10 μmol), isopropanol (705.4 μl , 9213 μmol), water (3.6 μl , 200 μmol) and nitric acid (0.5 μl , 12 μmol). The $\text{E}_x\text{Zr}_{20}\text{Al}_{80-x}$ with 59 dopant (E) of three different loading level ($x = 1, 5, 10$), the M_3N_{97} ($\text{N} = \text{Cu}, \text{Fe}, \text{Nb}, \text{Sn}, \text{Ta}, \text{V}$) with 55 dopant (M), ternary mixed oxides $(\text{Z}_1)_{33}(\text{Z}_2)_{33}(\text{Z}_3)_{33}$ ($\text{Z} = \text{Mo}, \text{V}, \text{Te}, \text{Ta}, \text{Nb}, \text{Sb}, \text{W}, \text{Cr}, \text{Bi}, \text{Mn}, \text{Fe}$), ternary mixed oxides $\text{Mo}_x\text{Cr}_y\text{Te}_z$, $\text{V}_x\text{Cr}_y\text{Sb}_z$, $\text{Mo}_x\text{V}_y\text{Cr}_z$ ($0 \leq x, y, z \leq 100$, 10 mol% increment) with 66 compositions, and quaternary mixed oxides $\text{Mo}_a\text{V}_b\text{Te}_c\text{Nb}_d$ ($50 \leq a \leq 100$, $0 \leq b \leq 30$, $0 \leq c \leq 30$, $0 \leq d \leq 20$, 5

mol% increment) with 190 compositions were set by this method.

Method 2. This method also followed procedures similar to those described in detail previously [153,180]. In brief, the molar ratio of dopant:matrix:complexing agent (4-hydroxy-4-methyl-pentanone):alcohol (ethanol) was 3:97:300:2542. For example, Ni₃Co₉₇ was prepared by pipetting the following volumes of single solutions in sequence: 1 M cobalt propionate in ethanol mixed with ethanol and complexing agent (0.34 M, 564.6 μ l, 194 μ mol) and 0.1 M Ni(NO₃)₂·6 H₂O in methanol (60.0 μ l, 6 μ mol). The M₃P₉₇ (P = Co, Mn, Ni) with 55 dopant (M) were prepared by this method.

Method 3. The molar ratio of dopant (0.1 M solution in alcohol):matrix (1 M nitrate solution in methanol):complexing agent (4-hydroxy-4-methyl-pentanone):acid (propionic acid) was 3:97:300:2. The preparation of Ni₃Ce₉₇ was performed by pipetting the following volumes of single solutions in sequence: 1 M Ce(NO₃)₃·6 H₂O in methanol (194.0 μ l, 194 μ mol), 0.1 M Ni(NO₃)₂·6 H₂O in methanol (60.0 μ l, 6 μ mol) and complexing agent mixed with propionic acid (8.06 M, 74.5 μ l, 600 μ mol). The M₃Q₉₇ (Q = Ce, Cr, Ga, In, Zn) with 55 dopant (M) and ternary mixed oxide N_xCu_yCe_z (0 \leq x, y, z \leq 100, 10 mol% increment) with 66 compositions were set by this method.

After the pipetting process of an entire rack was completed, this rack was covered and placed on an orbital shaker (Titramax 100; Heidolph) for 3 h. After removing the lid, the rack was dried for 5 days at 40 °C to allow gel formation and catalyst drying. All samples were calcined in an oven at 65 °C for 5 h (at a heating rate of 0.2 °C min⁻¹) and at 250 °C for 5 h (at a heating rate of 0.2 °C min⁻¹). The catalyst powders obtained were ground in HPLC flasks and manually transferred into 207 hexagonally positioned wells (\varnothing 3.5 mm) in a stainless steel library plate (\varnothing 99 mm). The library was calcined again in an oven heated to 700 °C (in the study for the CO₂ reforming of methane) or to 600 °C in an oven with inert condition (in the study for the selective oxidation of propane) at a heating rate of 2 °C min⁻¹, and kept there for 2 h.

3.2. High-throughput testing of catalyst libraries

In the study for the CO₂ reforming of methane, the open-well, high-throughput reactor system was used at 600 °C connected to a micro-gas chromatograph for product analysis. A capillary bundle containing both the educt gas supply and the product gas sampling system is inserted sequentially into each well of the library plate. Figure 50 shows the drawing of all reactor parts and cross section of the sampling needle. The position of the capillary bundle is fixed while the complete reactor is moved. The high-throughput screenings were controlled by TestRig software by controlling *xyz*-stage movements [158].

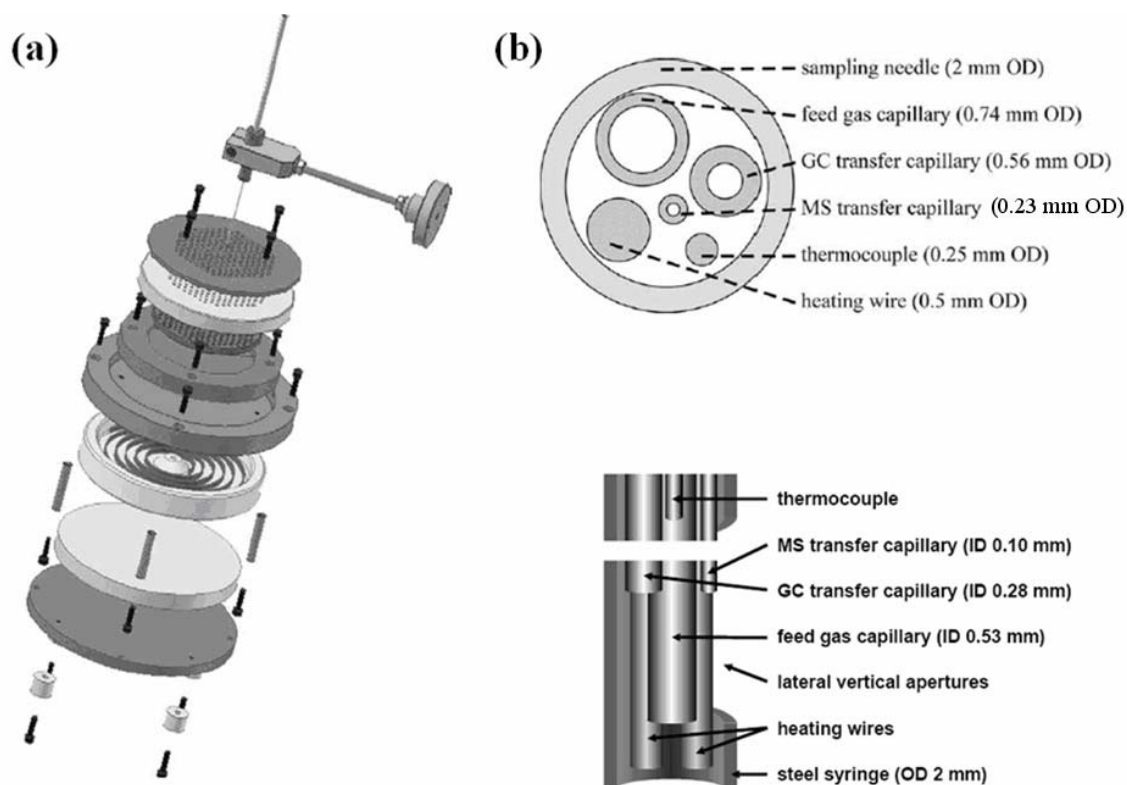


Figure 50. (a) Drawing of the reactor parts and their assembly. (b) Detailed scheme of the capillary bundle in the sampling needle.

The reactant gas, a certified calibration gas mixture composed of 52.8 vol% CH₄ and 47.2 vol% CO₂ (CH₄/CO₂ ratio: 1.12), was used without further purification. The flow rate of this gas mixture was always set to 10 ml min⁻¹. The gas composition of products was analyzed by a micro-gas chromatograph (model CP 4900; Varian) equipped with a thermal conductivity detector (sample time: 25 sec; sample line T: 50 °C; stabilizing time: 5 sec). Two packed columns, Porapak Q (length: 10 m; column T: 60 °C; injector T: 60 °C; inject time: 20 msec; run time: 110 sec) and molecular sieve 5A (length: 10 m; column T: 50 °C; injector T: 50 °C; inject time: 20 msec; backflush time: 10 sec; run time: 110 sec) were used in parallel to separate CH₄, CO₂ and H₂, CH₄, CO. The high-throughput equipment setup is schematically shown in Figure 51.

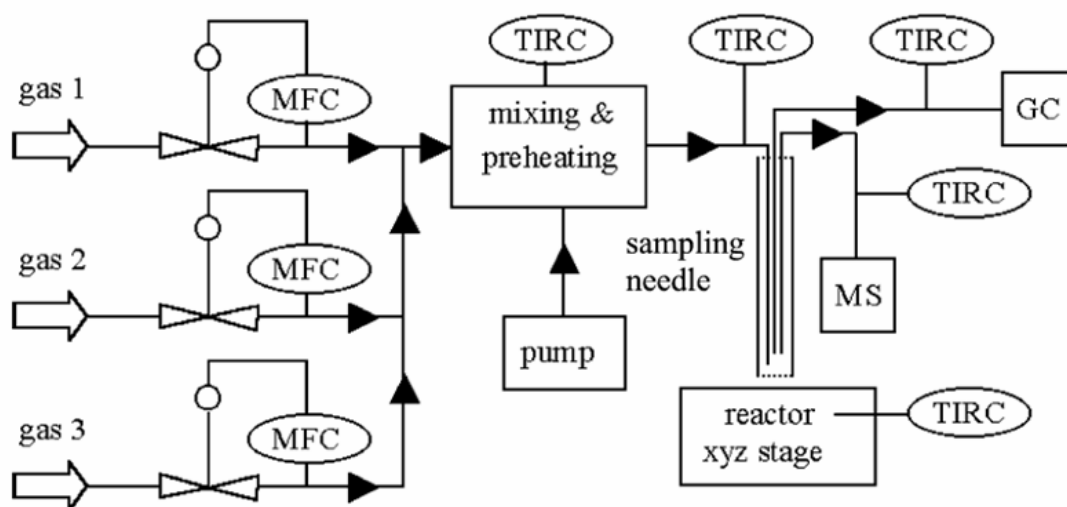


Figure 51. Schematic setup of the high-throughput equipment.

In the high-throughput screening for the selective oxidation of propane, a similar high-throughput reactor system as used in the study for the CO₂ reforming of methane was used at 420 °C connected to a quadrupole mass spectrometer (QMS) for product analysis. A liquid mass flow controller (MFC) connected to an autoclave was used to inject desirable amounts of water.

The injected water was well-mixed with reactant gas in a micro mixer from IMM as shown in Figure 52. In addition, the whole educt line was heated with thin heating elements controlled by a thin thermocouple to prevent liquid condensation. The products were monitored on-line by a quadrupole mass spectrometer (GSD 300 T2, Balzers). The composition of the reactant gas mixture was 8.7 vol% C₃H₈, 4.9 vol% O₂, 10 vol% H₂O, and Ar balance with a total flow rate of 5 ml min⁻¹. The monitored products m/z were 18 (water), 29 (C₃H₈), 40 (Ar), 41 (C₃H₆), 44 (CO₂), 55 (acrolein), and 72 (acrylic acid). In a standard experiment, it took about 120 s (100 s inside the hole for reaction, 10 s outside the hole for waiting, and another 10 s for xyz-stage moving) to evaluate the catalytic activity per well. The data obtained were analyzed computationally with the software MS Express written in our group [181].

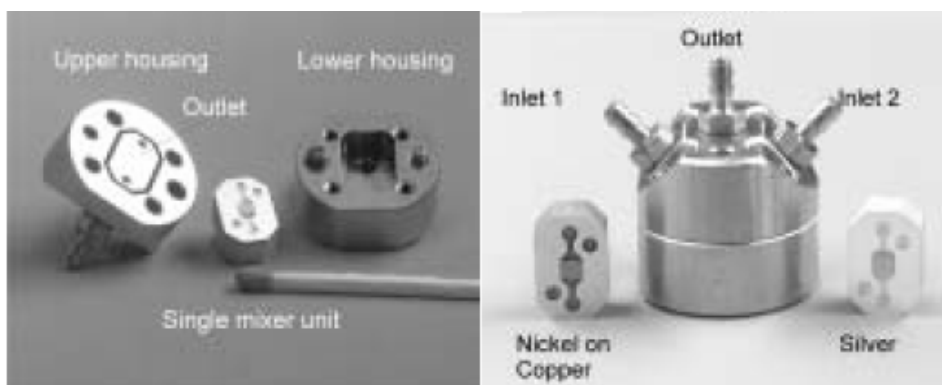


Figure 52. Picture of the micro mixer from IMM [182].

3.3. Conventional catalyst syntheses

The procedure of sol-gel preparation method 3 in the high-throughput synthesis was followed for the 50-times-larger scale in a conventional catalyst synthesis. The preparation of $\text{Al}_{\text{N}5}\text{Ni}_{10}\text{Ce}_{85}$, for example, was carried out as follows. The complexing agent (4-hydroxy-4-methyl-pentanone, 3.7 ml, 30 mmol) was placed in a 100-ml glass beaker. Then 1 M $\text{Ce}(\text{NO}_3)_3 \cdot 6 \text{H}_2\text{O}$ solution in methanol (8.5 ml, 8.5 mmol), 1 M $\text{Ni}(\text{NO}_3)_2 \cdot 6 \text{H}_2\text{O}$ solution in methanol (1.0 ml, 1 mmol) and 1 M $\text{Al}(\text{NO}_3)_3 \cdot 9 \text{H}_2\text{O}$ solution in methanol (0.5 ml, 0.5 mmol) were added, and the solution was magnetically stirred for 30 min. Propionic acid (15.0 μl , 0.2 mmol) was added dropwise under continuous stirring. The solution was stirred for another 3 h while covered with parafilm, to obtain a homogeneous solution. After the parafilm was removed, the solution was transferred to a wide, shallow beaker and dried for 5 days at 40 °C for gelation. Then it was carefully calcined in an oven at 65 °C for 5 h (at a heating rate of 0.2 °C min^{-1}) and at 250 °C for 5 h (at a heating rate of 0.2 °C min^{-1}). The catalyst powder obtained was ball-milled for 30 min, then recalcined in an oven, heated to 700 °C at a rate of 2 °C min^{-1} , and kept there for 2 h.

For comparison, a 10 mol% Ni containing catalyst supported on commercial $\gamma\text{-Al}_2\text{O}_3$ (Johnson Matthey, $S_{\text{BET}} = 255 \text{ m}^2 \text{ g}^{-1}$), referred to as Ni/ Al_2O_3 , was prepared using by the wet impregnation method as follows. After 1.268 g $\text{Ni}(\text{NO}_3)_2 \cdot 6 \text{H}_2\text{O}$ in 10 ml water was stirred for 30 min in a flask, 2.0 g $\gamma\text{-Al}_2\text{O}_3$ was added into the solution. Then the mixture in the flask was stirred and evaporated at 50 °C in a rotary evaporator system (IKA Labortechnik). After the solvent was removed, the wet powder was dried in an oven at 120 °C for 24 h. The catalyst powder obtained was ball-milled for 30 min, then calcined in an oven, heated to 700 °C at a rate of 2 °C min^{-1} , and kept there for 2 h.

3.4. Conventional testing of catalysts

Conventional catalytic studies were carried out in a gas-phase quartz tubular flow reactor (7 mm i.d., 400 mm long) at atmospheric pressure. The conventional testing equipment is schematically shown in Figure 53.

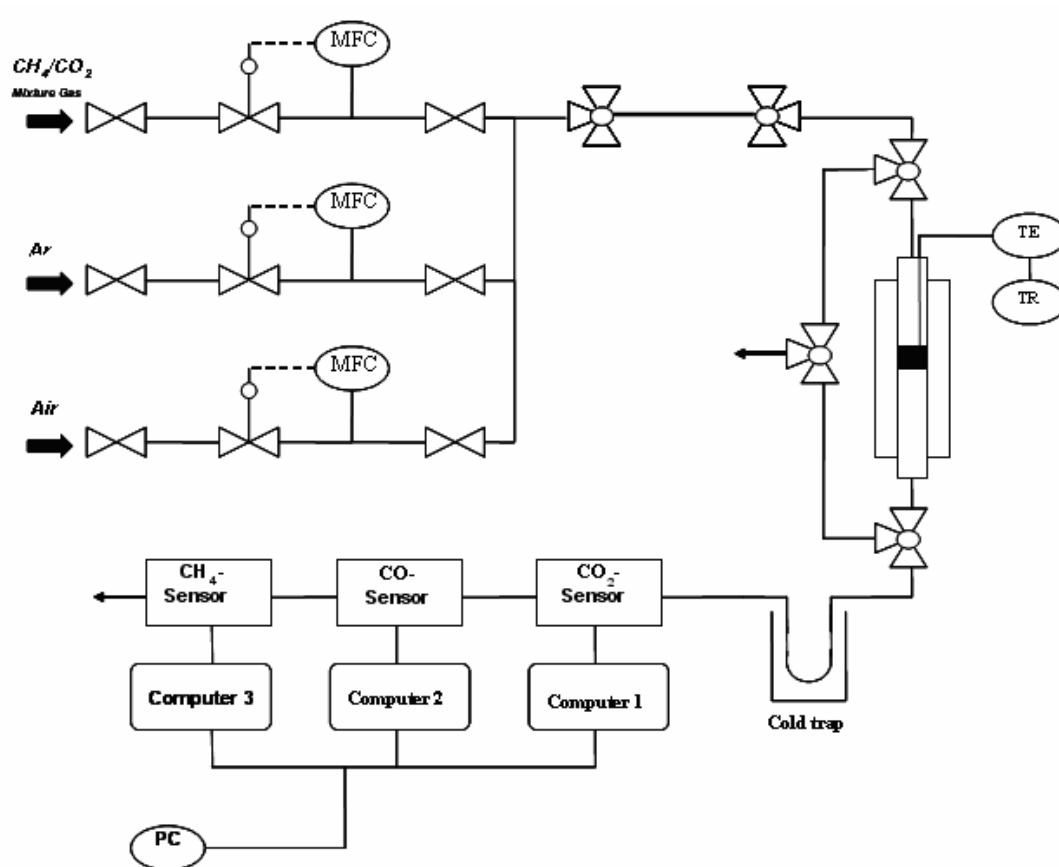


Figure 53. Schematic setup of the conventional testing.

Typically, 100 mg of catalyst sample as fine-powder (25–50 μm) was placed in the center of the reactor and held by quartz wool plugs. The reactor tube was heated inside an electric furnace. A quartz tube-sheathed K-type thermocouple was placed at the top of the catalyst bed to monitor

the reaction temperature. The reactant gas (52.8 vol% CH₄ (quality 3.5) and 47.2 vol% CO₂ (4.8)), diluted with argon (5.0), was used without further purification. The typical in situ reduction step was excluded, because the focus was on autoactivation performance. The following experimental conditions were used for a typical run. The catalyst was oxidized in situ at 600 °C for 2 h in flowing air (50 ml min⁻¹) under similar conditions as for the high-throughput experiment. After purging with Ar (50 ml min⁻¹) for 30 min, the gas flow was switched to an upstream reactant gas mixture (CH₄/CO₂/Ar = 16.9/15.1/68, total flow: 65 ml min⁻¹). A dilute reactant gas mixture was used to avoid hot-spots in the packed catalyst bed and for better temperature control. After switching, the catalyst bed temperature of the active catalyst was decreased for a short time due to a large endothermic heat change. The gas composition of products was analyzed by gas sensors (20 vol% CH₄, 25 vol% CO₂ and 10 vol% CO; GfG-mbH) and a micro-gas chromatograph (model CP 4900; Varian). Each sample was tested for 10 h and analyzed by 60 sequential GC measurement runs. Blank reaction tests without catalyst were carried out to confirm that the reactor and thermocouple itself were not catalytically active. In the conventional experiments, the deactivation rate (h⁻¹) for each catalyst was defined as [(1 - (the activity at last measurement)/(the maximum activity))/(time-on-stream between a maximum and a last point (h))].

For the regeneration studies, the following experimental conditions were typical for a single run. The catalyst was oxidized in situ at 600 °C for 2 h in flowing air (50 ml min⁻¹). After purging with Ar (50 ml min⁻¹) for 30 min, the gas flow was switched to an upstream reactant gas mixture (CH₄/CO₂/Ar = 16.9/15.1/68; total flow, 65 ml min⁻¹). Each sample was tested for 150 min with GC samplings after every 10 min within a measurement run. After the reaction test the catalyst was regenerated in situ at 600 °C for 2 h in a flow of air, Ar or H₂ (50 ml min⁻¹). After purging with Ar (50 ml min⁻¹) for 30 min, the reaction test was conducted again.

3.5. Pulse experiment

The transient pulse experiments were performed in a gas-phase quartz reactor (3 mm i.d., 520 mm length) at atmospheric pressure. Typically, the sample in fine powder form (25 - 50 μm) was placed in the center of the reactor and held by quartz wool plugs. The reactor tube was heated inside an electric furnace. The temperature of the catalyst bed was monitored by a thermocouple attached to the outside. Prior to taking the pulse data, the catalyst was treated in situ at 600 $^{\circ}\text{C}$ for 150 min in flowing Ar (30 ml min^{-1}). During the pulse experiment, gas pulses (CH_4 (quality 3.5), CO_2 (4.8) or H_2 (5.0)) with a volume of 100 μl (ca. 4.07 μmol) were passed at 600 $^{\circ}\text{C}$ over the catalyst sample using Ar (5.0) as carrier gas (30 ml min^{-1}). The time between consecutive pulses was 5 min. After the stabilization for 30 min in flowing Ar (30 ml min^{-1}) at 600 $^{\circ}\text{C}$, the pulses of a different gas were introduced by using a six-port valve (VICI). The operation principle of the six-port valve in two positions is schematically shown in Figure 54. The products were monitored on-line by a quadrupole mass spectrometer (GSD 300 T2, Balzers). Products m/z of 2 (H_2), 15 (CH_4), 17 (H_2O), 28 (CO), 32 (O_2), 40 (Ar), and 44 (CO_2) were monitored. The argon intensity of each pulse was chosen for internal standardization as representative within the chronological progress recording the detection sensitivity over the whole experiment. The normalized areas under a peak were integrated and then converted to molar fraction using a conversion factor that was determined after the experiments. The areas under the peaks were reproducible within about 8 %. The conversion factors were determined in the experimental conditions as close as possible to the product gas compositions in a blank reactor at 600 $^{\circ}\text{C}$. To obtain the conversion factor, blank tests were carried out for a variety of reactant/product gases and their compositions (CH_4 and CO_2 , H_2 and CH_4 , CO_2 and CO , H_2 and CO in 100 μl sample loop and H_2 and CO , H_2 and CH_4 in 200 μl sample loop). In our pulse experiment system, the only oxygen source is the catalyst itself because of the absence of

gaseous oxygen. Among the products (i.e., H_2 , H_2O , CO , and CO_2), the detection time of 5 min was not sufficient for water (due to interaction with the walls of the capillary connecting the reactor with the QMS). Therefore, the amount of water released was determined indirectly by the amount of H_2 consumed for H_2 pulses or the amount of CH_4 consumed for CH_4 pulses. A blank reaction test without catalyst was carried out to confirm that the reactor itself was not catalytically active. Only negligible amount of products was formed and the amount was considered in the conversion factor.

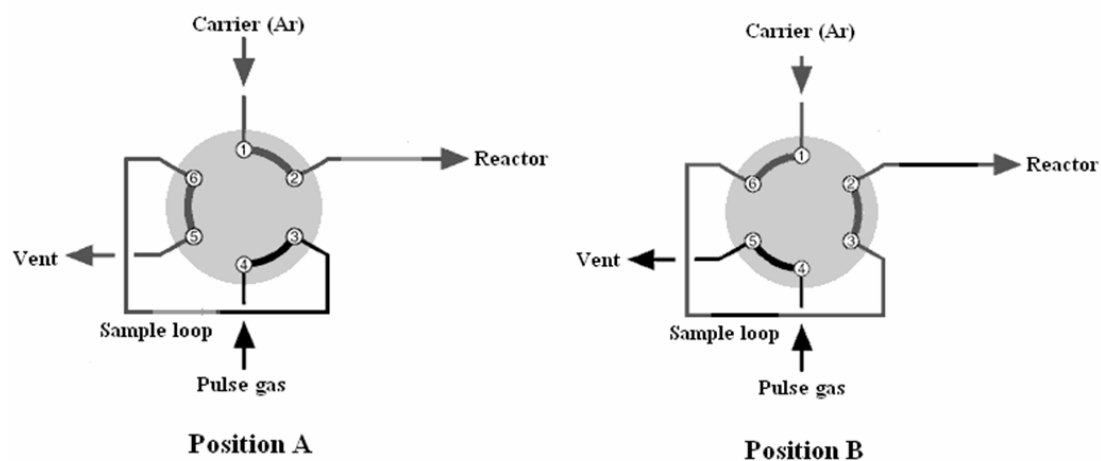


Figure 54. Operation principle of six-port valve in two positions.

3.6. Catalyst characterization

The chemical composition of catalysts was analysed semi-quantitatively by standardless X-ray fluorescence (XRF) spectroscopy (EAGLE II μ -Probe, EDAX) with Rh- K_{α} radiation using the fundamental parameter model. The X-ray beam was focused to a spot size of 300 μm on the surface of samples.

Total BET surface areas were measured by nitrogen adsorption (Sorptomatic 1990, Carlo Erba) at the temperature of liquid nitrogen. The samples were outgassed overnight under vacuum at 200 $^{\circ}\text{C}$ before adsorption.

Temperature-programmed oxidation (TPO) was done by thermogravimetric analysis (TGA) using a Shimadzu TGA-50 thermogravimetric analyser. After 10 h of reaction time, the catalyst sample was cooled to room temperature in a flow of Ar and then transferred to the TGA apparatus. About 50 mg of sample was loaded in a sample pan. The weight change of the catalyst was recorded in a flow of air (15 ml min^{-1}) as temperature increased from room temperature to 900 $^{\circ}\text{C}$ at a rate of 15 $^{\circ}\text{C min}^{-1}$.

Structural characterization of $\text{Ni}_{10}\text{Ce}_{90}$ catalysts was performed by powder X-ray diffraction (XRD) with a Huber G 670 Guinier-camera using Cu $K_{\alpha 1}$ radiation ($\lambda=1.54056 \text{ \AA}$). The powder diffraction patterns of the $\text{Ni}/\text{Al}_2\text{O}_3$ catalysts were recorded by means of a D5000 diffractometer (Bruker-Nonius Corp.) in focussing Bragg-Brentano reflection geometry with a Cu fine focus tube ($U = 40\text{kV}$, $I = 25\text{mA}$) and a Johansson-type quartz monochromator ($\lambda(\text{Cu-}K_{\alpha 1}) = 1.54056 \text{ \AA}$). The diffracted intensity was measured by a linear position sensitive detector PSD with Ar/10% methane filling at 8.5 bar pressure and an aperture of 10 mm to improve spatial resolution. In step scan mode the step width was *ca.* 0.015 $^{\circ}$ in 2θ . Lattice parameter refinement was done by full pattern Rietveld refinement with the program TOPAS [183] using the fundamental parameters approach [184].

X-ray photoelectron spectra (XPS) were recorded by a VG ESCALAB MK II spectrometer using Al K α radiation (1486.6 eV). The reaction or reduction of samples was performed in a gas-phase quartz reactor with an on/off valve on the top and bottom of the reactor. The reactor with the sample under Ar was transferred to a glove box, in which the sample in powder form was mixed with zirconium (about one-third of total weight) to compensate charging of the non-conducting samples during the measurement and was pressed into a pellet. The resulting pellet was placed in a transfer chamber with a stainless steel sample holder under the inert condition to avoid any exposure to the atmosphere before the analysis. The XPS data from the regions related to the C 1s, O 1s, Ce 3d, and Ni 2p core levels were recorded for each sample. The binding energies were adjusted relative to C 1s at 284.5 eV.

4. Summary and Conclusion

High-throughput synthesis and primary screening techniques were utilized in the search for and optimization of new autoactivation catalysts for the CO₂ reforming of methane to syngas and new catalysts for the selective oxidation of propane to acrylic acid. The general strategy for this high-throughput experiment involved both the creation of a library of spatially separated catalysts and evaluation of the materials in the library in terms of initial and long-term performance. Highly tolerant synthesis recipes based on sol–gel procedures have been successfully used, which allow the broad screening and optimization of elemental compositions. A simple open-well high-throughput reactor system connected to a micro-gas chromatograph or a quadrupole mass spectrometer for product analysis was modified for high-temperature screening and then used to test catalytic activities and stabilities.

In the study of the CO₂ reforming of methane, during generations 1 and 2, over 5000 highly diverse mixed oxides were tested for potential catalytic activity. Ni₁₀Ce₉₀O_x demonstrated effective activity and stability among nonprecious metal catalysts without a prereduction step. In a conventional study, two advantages (i.e., rapid start-up operation and high coking resistance) of Ni₁₀Ce₉₀O_x were noted relative to the commercial Ni/Al₂O₃ catalyst, but a slow but continuous catalyst deactivation was also recognized. To reduce deactivation of Ni₁₀Ce₉₀O_x, catalyst libraries with additional dopants were prepared and examined during generations 3 and 4. Among these, (Al, Zr)_yNi₁₀Ce_{90-y}O_x (y = 5, 15) exhibited comparable activity and strongly reduced deactivation compared with Ni₁₀Ce₉₀O_x. In the conventional tests of the best catalysts, the improved performance of the catalysts, especially Al₁₅Ni₁₀Ce₇₅O_x and Zr₁₅Ni₁₀Ce₇₅O_x could be confirmed. From the good reproducibility of the combinatorial results in conventional experiments it has been demonstrated that a simple high-throughput technology can be

successfully applied to search for new catalyst formulations even in high-temperature reactions.

The mechanistic study of the $\text{Ni}_{10}\text{Ce}_{90}\text{O}_x$ for the CO_2 reforming of methane was performed by X-ray diffraction (XRD) and pulse experimentation to elucidate the structural features connected to catalytic activity and stability and from those results a reaction mechanism was proposed. The XRD reflections corresponding to Ni species of the $\text{Ni}_{10}\text{Ce}_{90}\text{O}_x$ catalyst were very weak, together with the line broadening because of its very small particles or the formation of solid solution. The exceptional properties of $\text{Ni}_{10}\text{Ce}_{90}\text{O}_x$ are attributed to an intrinsic result of the acid catalyzed sol-gel preparation, well-known to provide atomically dispersed mixed oxides. From the pulse experiments and regeneration tests of $\text{Ni}_{10}\text{Ce}_{90}\text{O}_x$, it was demonstrated that (i) the interfacial oxygen in the Ni-Ce boundary is an active component for the complete oxidation of methane, (ii) methane is reformed to syngas through the reaction with the oxygen migrated from ceria lattice, and (iii) subsequently, the oxygen vacancies of ceria lattice are supplemented by oxygen arising from the dissociative adsorption of CO_2 . However, the consumed interfacial oxygen in the Ni-Ce boundary cannot be recovered by oxygen from CO_2 dissociation.

The doping effect of Zr on the activity and stability of Ni-Ce mixed oxide was investigated by X-ray diffraction (XRD) and pulse experimentation, and it was found that the oxygen storage/release capacity (OSC) improved by production of $\text{CeO}_2\text{-ZrO}_2$ solid solution allowed $\text{Zr}_{15}\text{Ni}_{10}\text{Ce}_{75}\text{O}_x$ to have higher activity and stability.

In the study of catalysts for the selective oxidation of propane, more than 600 samples composed of ternary and quaternary mixed oxides were synthesized and screened. It was not fulfilled to discover and optimize new materials which show high activity for acrylic acid formation.

Zusammenfassung und Schlussfolgerungen

Hochdurchsatzsynthesen und Screeningmethoden wurden bei der Suche und Optimierung neuer selbstreduzierender CO₂ Reformierungskatalysatoren von Methan zu Synthesegas sowie von neuen Katalysatoren für die selektive Oxidation von Propan zu Acrylsäure verwendet. Die generelle Strategie für die Hochdurchsatzexperimente umfasste die Herstellung von Materialbibliotheken mit räumlich getrennten Katalysatoren und die Untersuchung der katalytischen Eigenschaften dieser Materialien in Hinblick auf Anfangsaktivität sowie Langzeitstabilität. Die Verwendung äußerst toleranter Sol-Gel Synthesevorschriften ermöglichte die Untersuchung und Optimierung innerhalb weiter Zusammensetzungsbereiche. Ein einfaches offenes Hochdurchsatzreaktorsystem, das zur Produktanalyse mit einem Micro-GC bzw. einem Quadropol Massenspektrometer verbunden war, wurde für Hochtemperaturexperimente modifiziert und schließlich zur Untersuchung der katalytischen Aktivitäten und Stabilitäten benutzt.

Im Fall der CO₂ Reformierung von Methan wurden mehr als 5000 hochdiverse binäre Mischoxide auf eine mögliche katalytische Aktivität hin untersucht. Unter den edelmetallfreien Verbindungen zeichnete sich vor allem Ni₁₀Ce₉₀O_x als aktive und langzeitstabile Verbindung aus, die keinen Vorreduzierungsschritt benötigte. Konventionelle Untersuchungen zeigten zwei Vorteile von Ni₁₀Ce₉₀O_x gegenüber einem kommerziell erhältlichen Ni/Al₂O₃ Katalysator auf: Direkter Operationsbetrieb ohne Vorbehandlung und geringe Tendenz zur Kohlenstoffabscheidung. Dennoch wurde eine langsame kontinuierliche Desaktivierung des Katalysators festgestellt. Zur Minimierung dieser Desaktivierung von Ni₁₀Ce₉₀O_x wurden weitere Katalysatorbibliotheken durch Dotieren mit zusätzlichen Elementen präpariert und in den beiden folgenden Generationen untersucht. Dabei zeigten (Al, Zr)_yNi₁₀Ce_{90-y}O_x (y = 5 bzw.

15) vergleichbare Aktivität bei deutlich reduzierter Desaktivierung im Vergleich zum undotierten $\text{Ni}_{10}\text{Ce}_{90}\text{O}_x$. Konventionelle Versuche mit den besten Materialien bestätigten die verbesserte Leistungsfähigkeit dieser Katalysatoren, vor allem von $\text{Al}_{15}\text{Ni}_{10}\text{Ce}_{75}\text{O}_x$ und von $\text{Zr}_{15}\text{Ni}_{10}\text{Ce}_{75}\text{O}_x$. Diese gute Reproduzierbarkeit der kombinatorischen Ergebnisse in konventionellen Studien zeigt, dass eine relativ simple Hochdurchsatztechnologie erfolgreich in der Suche neuer Katalysatoren selbst für Hochtemperaturreaktionen eingesetzt werden kann.

Mechanistische Studien der CO_2 Reformierung über $\text{Ni}_{10}\text{Ce}_{90}\text{O}_x$ wurden mit Hilfe von Röntgenbeugungs- und Puls-Experimenten durchgeführt, um Zusammenhänge zwischen strukturellen Parametern und katalytischer Aktivität und Stabilität aufzuzeigen. Röntgenbeugungsdiagramme zeigten lediglich sehr schwache und breite Beugungssignale von Ni-Spezies in $\text{Ni}_{10}\text{Ce}_{90}\text{O}_x$ auf, was auf sehr kleinen Partikeln bzw. auf der Ausbildung von festen Lösungen beruht. Diese außergewöhnlichen Eigenschaften von $\text{Ni}_{10}\text{Ce}_{90}\text{O}_x$ basieren auf dem sauer katalysierten Sol-Gel-Prozess, der die Präparation von Mischoxiden mit einer homogenen atomaren Verteilung ermöglicht. Die Pulsexperimente und Regenerierungstests mit $\text{Ni}_{10}\text{Ce}_{90}\text{O}_x$ ergaben, dass (1) die an den Ni-Ce Grenzflächen lokalisierten Sauerstoffspezies als aktive Komponente für die Oxidation von Methan, (2) die Umsetzung von Methan zu Synthesegas über Sauerstofftransfer vom Cerdioxidgitter und schließlich (3) die so gebildeten Sauerstofflücken im Cerdioxidgitter durch der dissoziativen Adsorption von CO_2 entsprungenem Sauerstoff wieder aufgefüllt werden. Dennoch kann der verbrauchte grenzflächenlokalisierte Sauerstoff durch die CO_2 Dissoziation nicht wieder hergestellt werden.

Der Effekt der Zr-Dotierung auf die Aktivität und Langzeitstabilität des Ni-Ce-Mischoxids wurde mit Hilfe von Röntgenbeugungs- und Puls-Experimenten untersucht, wobei die Ausbildung einer festen Lösung von CeO_2 und ZrO_2 eine verbesserte Sauerstoff Speicher- und Abgabe-Kapazität bewirkte, die in einer höheren Aktivität und Langzeitstabilität von $\text{Zr}_{15}\text{Ni}_{10}\text{Ce}_{75}\text{O}_x$ resultierte.

Im Fall der selektiven Oxidation von Propan wurden mehr als 600 ternäre und

quaternäre Mischoxide dargestellt und mit Hilfe von Hochdurchsatzmethoden untersucht, wobei jedoch kein neues Material entdeckt und optimiert werden konnte, das hohe Aktivitäten für die Bildung von Acrylsäure aufwies.

5. References

- [1] M. Hammada, D. Badarneh, K. Tahboub, *Energy Convers. Manage.* 40 (1999) 1463.
- [2] J. Huang, R.J. Crookes, *Fuel* 77 (1998) 1793.
- [3] A. Effendi, K. Hellgardt, Z.-G. Zhang, T. Yoshida, *Catal. Commun.* 4 (2003) 203.
- [4] C.N. Hamelinck, A.P.C. Faaij, *J. Power Sources* 111 (2002) 1.
- [5] C. Courson, L. Udron, D. 'Swierczy'nski, C. Petit, A. Kiennemann, *Catal. Today* 76 (2002) 75.
- [6] S. Rapagna, H. Provendier, C. Petit, A. Kiennemann, P.U. Foscolo, *Biomass Bioenergy* 22 (2002) 377.
- [7] J. Staniforth, R.M. Ormerod, *Catal. Lett.* 81 (2002) 19.
- [8] A. Effendi, Z.-G. Zhang, K. Hellgardt, K. Honda, T. Yoshida, *Catal. Today* 77 (2002) 181.
- [9] S. Vasileiadis, Z. Ziaka-Vasileiadou, *Chem. Eng. Sci.* 59 (2004) 4853.
- [10] J.M. Fox III, *Catal. Rev. –Sci. Eng.* 35 (1993) 169.
- [11] A.T. Ashcroft, A.K. Cheetham, M.L.H. Green, P.D.F. Vernon, *Nature* 352 (1991) 225.
- [12] G.F. Froment, *J. Mol. Catal. A* 163 (2000) 147.
- [13] M.A. Pena, J.P. Gomez, J.L.G. Fierro, *Appl. Catal. A* 144 (1996) 7.
- [14] B.-Q. Xu, W.M.H. Sachtler, *J. Catal.* 180 (1998) 198.
- [15] S. Wang, G.Q. Lu, G.J. Millar, *Energy Fuels* 10 (1996) 896.
- [16] S.-H. Lee, W. Cho, W.-S. Ju, B.-H. Cho, Y.-C. Lee, Y.-S. Baek, *Catal. Today* 87 (2003) 133.
- [17] K. Tomishige, S. Kanazawa, K. Suzuki, M. Asadullah, M. Sato, K. Ikushima, K. Kunimori, *Appl. Catal. A* 233 (2002) 35.
- [18] A.L. Larentis, N.S. Resende, V.M.M. Salim, J.C. Pinto, *Appl. Catal. A* 215 (2001) 211.
- [19] J.H. Edwards, A.M. Maitra, *Fuel Process. Technol.* 42 (1995) 269.
- [20] K. Asami, X. Li, K. Fujimoto, Y. Koyama, A. Sakurama, N. Kometani, Y. Yonezawa, *Catal.*

- Today 84 (2003) 27.
- [21] A.M. Gadalla, B. Bower, Chem. Eng. Sci. 43 (1988) 3049.
- [22] J.-H. Kim, D.J. Suh, T.-J. Park, K.-L. Kim, Appl. Catal. A 197 (2000) 191.
- [23] M.C.J. Bradford, M.A. Vannice, Catal. Rev. –Sci. Eng. 41 (1999) 1.
- [24] T. Inui, Appl. Organomet. Chem. 15 (2001) 87.
- [25] M.C.J. Bradford, M.A. Vannice, Appl. Catal. A. 142 (1996) 73.
- [26] A.A. Lemonidou, I.A. Vasalos, Appl. Catal. A 228 (2002) 227.
- [27] M.F. Mark, W.F. Maier, J. Catal. 164 (1996) 122.
- [28] Q.G. Yan, W.Z. Weng, H.L. Wan, H. Toghiani, R.K. Toghiani, C.U. Pittman, Appl. Catal. A 239 (2003) 43.
- [29] Z. Zhang, X.E. Verykios, Appl. Catal. A 138 (1996) 109.
- [30] X.E. Verykios, Int. J. Hydrogen Energy 28 (2003) 1045.
- [31] J.-M. Wei, B.-Q. Xu, J.-L. Li, Z.-X. Cheng, Q.-M. Zhu, Appl. Catal. A 196 (2000) L167.
- [32] Y.H. Hu, E. Ruckenstein, Catal. Lett. 43 (1997) 71.
- [33] S. Wang, G.Q. Lu, Energy Fuels 12 (1998) 248.
- [34] J.B. Wang, S.-Z. Hsiao, T.-J. Huang, Appl. Catal. A 8521 (2003) 1.
- [35] H.-S. Roh, K.-W. Jun, S.-C. Baek, S.-E. Park, Catal. Lett. 81 (2002) 147.
- [36] H.S. Roh, H.S. Potdar, K.W. Jun, J.W. Kim, Y.S. Oh, Appl. Catal. A 276 (2004) 231.
- [37] H.S. Roh, H.S. Potdar, K.W. Jun, Catal. Today 93-95 (2004) 39.
- [38] J.A. Montoya, E. Romero-Pascual, C. Gimon, P.D. Angel, A. Monzónb, Catal. Today 63 (2000) 71.
- [39] H.S. Potdar, H.S. Roh, K.W. Jun, M. Ji, Z.W. Liu, Catal. Lett. 84 (2002) 95.
- [40] T. Hayakawa, S. Suzuki, J. Nakamura, T. Uchijima, S. Hamakawa, K. Suzuki, T. Shishido, K. Takehira, Appl. Catal. A 183 (1999) 273.
- [41] Z. Xu, Y. Li, J. Zhang, L. Chang, R. Zhou, Z. Duan, Appl. Catal. A 210 (2001) 45.

- [42] T. Horiuchi, K. Sakuma, T. Fukui, Y. Kubo, T. Osaki, T. Mori, *Appl. Catal. A* 144 (1996) 111.
- [43] J. Juan-Juan., M.C. Román-Martinez, M.J. Illán-Gómez, *Appl. Catal. A* 264 (2004) 169.
- [44] C.E. Quincoces, S. Dicundo, A.M. Alvarez, M.G. Gonzalez, *Mater. Lett.* 50 (2001) 21.
- [45] T. Osaki, T. Mori, *J. Catal.* 204 (2001) 89.
- [46] J.-S. Choi, K.-I. Moon, Y.G. Kim, J.S. Lee, C.-H. Kim, D.L. Trimm, *Catal. Lett.* 52 (1998) 43.
- [47] S.-H. Seok, S.H. Choi, E.D. Park, S.H. Han, J.S. Lee, *J. Catal.* 209 (2002) 6.
- [48] S.-H. Seok, S.H. Han, J.S. Lee, *Appl. Catal. A* 215 (2001) 31.
- [49] C.E. Quincoces, S.P. de Vargas, P. Grange, M.G. Gonzalez, *Mater. Lett.* 56 (2002) 698.
- [50] B.S. Liu, C.T. Au, *Appl. Catal. A* 244 (2003) 181.
- [51] Z. Xu, Y. Li, J. Zhang, L. Chang, R. Zhou, Z. Duan, *Appl. Catal. A* 213 (2001) 65.
- [52] S. Wang, G.Q. Lu, *Appl. Catal. B* 19 (1998) 267.
- [53] Z. Hou, O. Yokota, T. Tanaka, T. Yashima, *Appl. Surf. Sci.* 223 (2004) 58.
- [54] A. Valentini, N.L.V. Carreño, L.F.D. Probst, P.N. Lisboa-Filho, W.H. Schreiner, E.R. Leite, E. Longo, *Appl. Catal. A* 255 (2003) 211.
- [55] M.G. Gonzalez, N.N. Nichio, B. Moraweck, G. Martin, *Mater. Lett.* 45 (2000) 15.
- [56] K. Tomishige, Y. Chen, K. Fujimoto, *J. Catal.* 181 (1999) 91.
- [57] Y.-G. Chen, K. Tomishige, K. Yokoyama, K. Fujimoto, *J. Catal.* 184 (1999) 479.
- [58] Y. Liu, T. Cheng, D. Li, P. Jiang, J. Wang, W. Li, Y. Bi, K. Zhen, *Catal. Lett.* 85 (2003) 101.
- [59] B.S. Liu, C.T. Au, *Catal. Lett.* 85 (2003) 165.
- [60] S. Tomiyama, R. Takahashi, S. Sato, T. Sodesawa, S. Yoshida, *Appl. Catal. A* 241 (2003) 349.
- [61] S. Tang, L. Ji, J. Lin, H.C. Zeng, K.L. Tan, K. Li, *J. Catal.* 194 (2000) 424.
- [62] T. Osaki, T. Horiuchi, T. Sugiyama, K. Suzuki, T. Mori, *Catal. Lett.* 52 (1998) 171.

- [63] D.J. Suh, T.-J. Park, J.-H. Kim, K.-L. Kim, *J. Non-Cryst. Solids* 225 (1998) 168.
- [64] H. Li, J. Wang, *Che. Eng. Sci.* 59 (2004) 4861.
- [65] L. Ji, S. Tang, H.C. Zeng, J. Lin, K.L. Tan, *Appl. Catal. A* 207 (2001) 247.
- [66] S. Tomiyama, R. Takahashi, S. Sato, T. Sodesawa, S. Yoshida, *Appl. Catal. A* 241 (2003) 349.
- [67] U. Olsbye, O. Moen, A. Slagtern, I.M. Dahl, *Appl. Catal. A* 228 (2002) 289.
- [68] T. Wurzel, S. Malcus, L. Mleczko, *Che. Eng. Sci.* 55 (2000) 3955.
- [69] Y. Matsuo, Y. Yoshinaga, Y. Sekine, K. Tomishige, K. Fujimoto, *Catal. Today* 63 (2000) 439.
- [70] J.R. Rostrup-Nielsen, *J. Catal.* 85 (1984) 31.
- [71] www.fuelcells.unicore.com/de/downloads/fcprotonics032004.pdf
- [72] J.A.C. Dias, J.M. Assaf, *J. Power Sources* 139 (2005) 176.
- [73] P.H. Matter, D.J. Braden, U.S. Ozkan, *J. Catal.* 223 (2004) 340.
- [74] M.F. Mark, W.F. Maier, *Angew. Chem. Int. Ed.* 33 (1994) 1657.
- [75] A. Erdohelyi, J. Cserenyi, F. Solymosi, *J. Catal.* 141 (1993) 287.
- [76] M.C.J. Bradford, M.A. Vannice, *Appl. Catal. A* 142 (1996) 97.
- [77] M.C.J. Bradford, M.A. Vannice, *J. Catal.* 173 (1998) 157.
- [78] K. Nagaoka, K. Seshan, K. Aika and J. A. Lercher, *J. Catal.* 197 (2001) 34.
- [79] E. Ruckenstein, Y.H. Hu, *J. Catal.* 162 (1996) 230.
- [80] A. Slagtern, Y. Schuurman, C. Leclercq, X. Verykios, C. Mirodatos, *J. Catal.* 172 (1997) 118.
- [81] J.H. Bitter, K. Seshan, J.A. Lercher, *J. Catal.* 171 (1997) 279.
- [82] J.H. Bitter, K. Seshan, J.A. Lercher, *J. Catal.* 176 (1998) 93.
- [83] M. Ebelmen, *Ann. Chimie Phys.* 16 (1846) 129.
- [84] L.L. Hench, J.L. West, *Chem. Rev.* 90 (1990) 33.

- [85] G. Frenzer, W.F. Maier, *Annu. Rev. Mater. Res.*, accepted.
- [86] J.-F. Lambert, M. Che, *J. Mol. Catal. A* 162 (2000) 5.
- [87] R.D. Gonzalez, T. Lopez, R. Gomez, *Catal. Today* 35 (1997) 293.
- [88] K. Haas-Santo, M. Fichtner, K. Schuber, *Appl. Catal. A* 220 (2001) 79.
- [89] J. Klein, W.F. Maier, *Chem. Mater.* 11 (1999) 2584.
- [90] J. Klein, C. Lettmann, W.F. Maier, *J. Non-Cryst. Solids* 282 (2001) 203.
- [91] C.J. Brinker, *Non-Cryst. Solids* 100 (1988) 31.
- [92] C.J. Brinker and G.W. Scherer, *Sol-Gel Science: The Physics and Chemistry of Sol-Gel Processing*, Academic Press, New York, (1990).
- [93] W.F. Maier, lecture note (TC5 Kombinatorische Chemie), Universität des Saarlandes.
- [94] S. Senkan, *Angew. Chem. Int. Ed.* 40 (2001) 312.
- [95] J.J. Hanak, *J. Mater. Sci.* 5 (1970) 964.
- [96] X.-D. Xiang, X. Sun, G. Briceno, Y. Lou, K.-A. Wang, H. Chang, W.G. Wallace-Freedman, S.-W. Chen, P.G. Schultz, *Science* 268 (1995) 1738 .
- [97] F.C. Moates, M. Somani, J. Annamalai, J.T. Richardson, D. Luss, R.C. Wilson, *Ind. Eng. Chem. Res.* 35 (1996) 4801.
- [98] R.J. Hendershot, C.M. Snively, J. Lauterbach, *Chem. Eur. J.* 11 (2005) 806.
- [99] S.I. Woo, K.W. Kim, H.Y. Cho, K.S. Oh, M.K. Jeon, N.H. Tarte, T.S. Kim, A. Mahmood, *QSAR Comb. Sci.* 24 (2005) 138.
- [100] F. Schüth, O. Busch, C. Ho.mann, T. Johann, C. Kiener, D. Demuth, J. Klein, S. Schunk, W. Strehlau, T. Zech, *Top. Catal.* 21 (2002) 55.
- [101] E. Danielson, J. H. Golden, E. W. McFarland, C. M. Reaves, W. H. Weinberg, X. D. Wu, *Nature* 389 (1997) 944.
- [102] P. Cong, R. D. Doolen, Q.Fan, D. M. Giaquinta, S. Guan, E. W. McFarland, D. M. Poojary, K. Self, H. W. Turner, W. H. Weinberg, *Angew. Chem. Int. Ed.* 38 (1999) 484.

- [103] P. Cong, A. Dehestani, R. Doolen, D.M. Giaquinta, S. Guan, V. Markov, D. Poojary, K. Self, H. Turner, W.H. Weinberg, *Proc. Natl. Acad. Sci.* 96 (1999) 11077.
- [104] T. Miyao, I. Shishikura, M. Matsuoka, M. Nagai, *Chem. Lett.* 121 (1996) 561.
- [105] M.B. Kizling, S.G. Jaras, *Appl. Catal. A* 147 (1996) 1.
- [106] G.P. Vossokov, P.S. Pirgov, *Appl. Catal. A* 168 (1998) 229.
- [107] Y.J. Kim, Y. Gao, S.A. Chambers, *Surf. Sci.* 371 (1997) 358.
- [108] A.A. Gorbunov, W. Pompe, A. Sewing, S.V. Gapanov, A.D. Akhsakhalyan, I.G. Zabrodin, I.A. Kaskov, E.B. Klyenkov, A.P. Mozorov, N.N. Salashchenko, R. Dietsch, H. Mai, S. Vollmar, *Appl. Surf. Sci.* 96 (1996) 649.
- [109] R. E. Russo, X. L. Mao, D. L. Perry, *ChemTech* 12 (1994) 14.
- [110] E. Reddington, A. Sapienza, B. Guraou, R. Viswanathan, S. Sarangapani, E. S. Smotkin, T. E. Mallouk, *Science* 280 (1998) 1735.
- [111] W.F. Maier, J. Martens, S. Klein, J. Heilmans, R. Parton, K. Vercruyssen, P. Jacobs, *Angew. Chem. Int. Ed.* 35 (1996) 180.
- [112] S. Bergh, S. Guan, A. Hagemeyer, C. Lugmair, H. Turner, A.F. Volpe, W.H. Weinberg, G. Mott, *Appl. Catal. A* 254 (2003) 67.
- [113] A.C. Cooper, L.H. McAlexander, D.-H. Lee, M.T. Torres, R.H. Crabtree, *J. Am. Chem. Soc.* 120 (1998) 9971.
- [114] H. Su, E. S. Yeung, *J. Am. Chem. Soc.* 122 (2000) 7422.
- [115] S. Senkan, *Nature* 394 (1998) 350.
- [116] A. Holzwarth, H.-W. Schmidt, W.F. Maier, *Angew. Chem. Int. Ed.* 37 (1998) 2644.
- [117] W. J. Haap, T. B. Walk, G. Jung, *Angew. Chem. Int. Ed.* 37 (1998) 3311.
- [118] C. M. Snively, G. Oskarsdottir, J. Lauterbach, *J. Comb. Chem.* 2 (2000) 243.
- [119] S. Senkan, K. Krantz, S. Ozturk, V. Zengin, I. Onal, *Angew. Chem. Int. Ed.* 38 (1999) 2794.

- [120] M. Orschel, J. Klein, H.-W. Schmidt, W.F. Maier, *Angew. Chem. Int. Ed.* 38 (1999) 2791.
- [121] P. Claus, D. Hönicke, T. Zech, *Catal. Today* 76 (2001) 319.
- [122] P. Claus, M. Lucas, *Appl. Catal. A* 254 (2003) 35.
- [123] U. Rodemerck, P. Ignaszewski, M. Lucas, P. Claus, *Chem. Ing. Tech.* 71 (1999) 873.
- [124] C. Mirodatos, Y. Schuurman, C. Hayaud, A. Holzwarth, D. Farusseng, T. Richter, EP 1293772 A2 (2003).
- [125] S. Guan, L. Van Erden, R.C. Haushalter, X.P. Zhou, X.J. Wang, R. Srinivasan, US 6149882 (2000).
- [126] C. Hoffmann, A. Wolf, F. Schüth, *Angew. Chem. Int. Ed.* 38 (1999) 2800.
- [127] C. Hoffmann, H.-W. Schmidt, F. Schüth, *J. Catal.* 198 (2001) 348.
- [128] S. Thomson, C. Hoffmann, S. Ruthe, H.-W. Schmidt, F. Schüth, *Appl. Catal. A* 220 (2001) 253.
- [129] C. Kiener, M. Kurtz, H. Wilmer, C. Hoffmann, H.W. Schmidt, J.D. Grunwaldt, M. Muhler, F. Schuth, *J. Catal.* 216 (2003) 110.
- [130] W. Huybrechts, J. Mijoin, P.A. Jacobs, J.A. Martens, *Appl. Catal. A* 243 (2003) 1.
- [131] R.J. Hendershot, S.S. Lasko, M.-F. Fellmann, G. Oskarsdottir, W.N. Delgass, C.M. Snively, J. Lauterbach, *Appl. Catal. A* 254 (2003) 107.
- [132] K.S. Oh, Y.K. Park, S.I. Woo, *Rev. Sci. Instrum.* 76 (2005) 062219.
- [133] R.S. Bohacek, C. McMartin, G. Colin, C. Wayne, *Med. Res. Rev.* 16 (1996) 3.
- [134] W.F. Maier, *Angew. Chem. Int. Ed.* 38 (1999) 1216.
- [135] J. Scheidtmann, P.-A.W. Weiss, W.F. Maier, *Appl. Catal. A* 222 (2001) 79.
- [136] C. Klanner, D. Farrusseng, L. Baumes, M. Lengliz, C. Mirodatos, F. Schüth, *Angew. Chem* 116 (2004) 5461.
- [137] D. Wolf, O.V. Buyevskaya, M. Baerns, *Appl. Catal. A* 200 (2000) 63.
- [138] U. Rodemerck, D. Wolf, O.V. Buyevskaya, P. Claus, S.M. Senkan, M. Baerns, *Chem. Eng.*

- J. 82 (2002) 3.
- [139] J.M. Serra, A. Chica, A. Corma, *Appl. Catal. A* 239 (2003) 35.
- [140] Y. Yamada, A. Ueda, I. Nakagawa, T. Kobayashi, *Res. Chem. Intermed.* 28 (2002) 397.
- [141] D. Farrusseng, C. Klanner, L. Baumes, M. Lengliz, C. Mirodatos, F. Schüth, *QSAR & Comb Sci* 24 (2005) 78.
- [142] R.K. Grasselli, *Top. Catal.* 21 (2002) 79.
- [143] K. Weissermel, H.-J. Arpe, *Industrial Organic Chemistry*, Wiley-VCH, Weinheim (2003).
- [144] M. Ai, *J. Catal.* 101 (1986) 389.
- [145] B. Kerler, A. Martin, M.M. Paul, M. Baerns, *Catal. Lett.* 78 (2002) 259.
- [146] N. Mizuno, M. Tateishi, M. Iwamoto, *Appl. Catal. A* 128 (1995) 165.
- [147] W. Ueda, Y. Suzuki, *Chem. Lett.* 7 (1995) 541.
- [148] A.C. Kaddouri, C. Mazzochia, E.G. Derouane, *J. Catal.* 211 (2002) 226.
- [149] T. Ushikubo, H. Nakamura, Y. Koyasu, S. Wajiki, EP 0,962,253,A2 (1999)
- [150] M. Baca, A. Pigamo, J.L. Dubios, J.M.M. Millet, *Top.Catal.* 23 (1999) 39.
- [151] Mitsubishi Chemicals, *Jpn. Patent* 10-36311 (1998).
- [152] B. Stein, C. Weimer, J. Gaube, *Stud. Surf. Sci. Catal.* 110 (1997) 357.
- [153] J.W. Saalfrank, W.F. Maier, *Angew. Chem. Int. Ed.* 43 (2004) 2028.
- [154] T. Wolter, W.F. Maier, in: R.A. Potyrailo, A. Karim, Q. Wang, T. Chikyow (Eds.), *MRS-Symposium Proceedings*, Vol. 804, 2004, p. 283.
- [155] P.-A.W. Weiss, J.W. Saalfrank, J. Scheidtmann, H.-W. Schmidt, W.F. Maier, in: R.A. Potyrailo, E.J. Amis (Eds.), *High Throughput Analysis: A Tool for Combinatorial Materials Science*, Kluwer Academic/Plenum Publishers, New York, 2003, p. 125.
- [156] J. Scheidtmann, J.W. Saalfrank, W.F. Maier, *Stud. Surf. Sci. Catal.* 145 (2003) 13.
- [157] J. Urschey, P.-A.W. Weiss, J. Scheidtmann, R. Richter, W.F. Maier, *Solid State Sci.* 5 (2003) 909.

- [158] J. Scheidtmann, PhD thesis, Universität des Saarlandes, 2003.
- [159] K. Tomishige, S. Kanazawa, M. Sato, K. Ikushima, K. Kunimori, *Catal. Lett.* 84 (2002) 69.
- [160] Z.X. Cheng, X.G. Zhao, J.L. Li, Q.M. Zhu, *Appl. Catal. A* 205 (2001) 31.
- [161] E. Rocchini, A. Trovarelli, J. Llorca, G.W. Graham, W.H. Weber, M. Maciejewski, A. Baiker, *J. Catal.* 194 (2000) 461.
- [162] S. Klein, S. Thorimbert, W.F. Maier, *J. Catal.* 163 (1996) 476.
- [163] M. Stöckmann, F. Konietzki, J.U. Notheis, J. Voss, W. Keune, W.F. Maier, *Appl. Catal. A* 208 (2001) 343.
- [164] G. Wrobel, M.P. Sohier, A. D'Huysser, J.P. Bonnelle, *Appl. Catal. A* 101 (1993) 73.
- [165] N. Yisup, Y. Cao, W.-L. Feng, W.-L. Dai, K.-N. Fan, *Catal. Lett.* 99 (2005) 207.
- [166] S.M. Stagg, F.B. Noronha, G. Fendley, D.E. Resasco, *J. Catal.* 194 (2000) 240.
- [167] J.H. Bitter, K. Seshan, J.A. Lercher, *J. Catal.* 176 (1998) 93.
- [168] S. Sharma, S. Hilaire, J.M. Vohs, R.J. Gorte, H.-W. Jen, *J. Catal.* 190 (2000) 199.
- [169] K. Otsuka, Y. Wang, E. Sunada, I. Yamanaka, *J. Catal.* 175 (1998) 152.
- [170] J.A. Rodriguez, J.C. Hanson, A. Frenkel, J.-Y. Kim, M. Perez, *J. Am. Chem. Soc.* 124 (2002) 346.
- [171] J.Z. Shyu, K. Otto, W.L.H. Watkins, G.W. Graham, R.K. Belitz, H.S. Gandhi, *J. Catal.* 114 (1988) 23.
- [172] M.S. Brogan, T.J. Dines, J.A. Cairns, *J. Chem. Soc., Faraday Trans.* 90 (1994) 1461.
- [173] S. Sieg, B. Stutz, T. Schmidt, F. Hamprecht, W.F. Maier, *J. Mol. Model.* (2006).
- [174] J.-H. Lee, E.-G. Lee, O.-S. Joo, K.-D. Jung, *Appl. Catal. A* 269 (2004) 1.
- [175] P. Fornasiero, J. Kašpar, V. Sergo, M. Graziani, *J. Catal.* 182 (1999) 56.
- [176] P. Fornasiero, R. Monte, G. Rao, J. Kašpar, S. Meriani, A. Trovarelli, M. Graziani, *J. Catal.* 151 (1995) 168.

- [177] T. Suzuki, A. Morikawa, A. Suda, H. Sobukawa, M. Sugiura, T. Kanazawa, J. Suzuki, T. Takada, R&D Review of Toyota CRDL Vol. 37 No.4.
- [178] F.B. Noronha, E.C. Fendley, R.R. Soares, W.E. Alvarez, D.E. Resasco, *Chem. Eng. J.* 82 (2001) 21.
- [179] J.S. Paul, P.A. Jacobs, P.-A.W. Weiss, W.F. Maier, *Appl. Catal. A* 265 (2004) 185.
- [180] M. Krämer, T. Schmidt, K. Stöwe, W.F. Maier, *Appl. Catal. A* 302 (2006) 257.
- [181] TOPAS, Version 2.1, Bruker AXS, Karlsruhe.
- [182] <http://www.imm-mainz.de/upload/dateien/IMM%20catalogue%20III2004.pdf>
- [183] R.W. Cheary, A.A. Coelho, *J. Appl. Cryst.* 25 (1992) 109.
- [184] P.-A.W. Weiss, C. Thome, W.F. Maier, *J. Comb. Chem.* 6 (2004) 520.
- [185] J.M. Rynkowski, T. Paryjczak, M. Lenik, M. Farbotko, J. Goralski, *J. Chem. Soc. Faraday Trans.* 91(1995) 3481.
- [186] J.W. Allen, *J. Mag. & Magn. Mater.* 47-48 (1985) 168.
- [187] K. Gschneider, L. Eyring, S. Hüfner, *Handbook on the Physics and Chemistry of Rare Earths*, North-Holland, Amsterdam, (1987) Vol. 10.
- [188] D.H. Kim, S.I. Woo, *Catal. Lett.* 98 (2004) 23.
- [189] A. Trovarelli, *Catal. Rev. –Sci. Eng.* 38 (1996) 439.
- [190] Q. Fu, H. Saltsburg, M. Flytzani-Stephanopoulos, *Science* 301 (2003) 935.